Experimental solid state quantum simulation using 1D superlattice structures

by

Megan Briggeman

B.A., Kenyon College, 2010

Submitted to the Graduate Faculty of

the Dietrich School of Arts and Sciences in partial fulfillment

of the requirements for the degree of

Doctor of Philosophy

University of Pittsburgh

2020

UNIVERSITY OF PITTSBURGH

DIETRICH SCHOOL OF ARTS AND SCIENCES

This dissertation was presented

by

Megan Briggeman

It was defended on

December 13, 2019

and approved by

Jeremy Levy, Distinguished Professor, Physics and Astronomy, Arts and Sciences

Michael Hatridge, Assistant Professor, Physics and Astronomy, Arts and Sciences

Arthur Kosowsky, Professor, Physics and Astronomy, Arts and Sciences

Roger Mong, Assistant Professor, Physics and Astronomy, Arts and Sciences

David Waldeck, Professor, Chemistry, Arts and Sciences

Dissertation Director: Jeremy Levy, Distinguished Professor, Physics and Astronomy, Arts

and Sciences

Experimental solid state quantum simulation using 1D superlattice structures

Megan Briggeman, PhD

University of Pittsburgh, 2020

In this thesis we describe experiments which explore 1D transport at the $LaAlO_3/SrTiO_3$ interface. Complex oxide systems, specifically those based on $SrTiO_3$, possess a wide range of magnetic and electronic properties, including superconductivity, magnetism, ferroelectricity, and ferroelasticity. Electron waveguide devices created at the $LaAlO_3/SrTiO_3$ interface exhibit quantized ballistic transport of electrons, electron pairs, and Pascal liquid phases-bound states of more than two electrons. Different types of periodic modulation are applied to the electron waveguides to create one-dimensional superlattices. By creating superlattice devices we are able to engineer new properties and enhance electron-electron interactions at the $LaAlO_3/SrTiO_3$ interface. These devices represent a first step towards developing a solid-state quantum simulation platform and will be used as building blocks for creating more complex quantum systems.

Keywords: Complex-oxides, 1D transport, strongly correlated physics.

Table of contents

List of tables

List of figures

xi

Preface

The work presented here is the culmination of many years of graduate work and wouldn't have been possible without the support of my friends, family, and the many people who have helped me during my time at Pitt.

I would like to thank my friends and family for their love and encouragement throughout this process. My advisor Jeremy Levy and all of my LevyLab colleagues have been a constant source of help and support during my graduate career. Thanks to our collaborators in the group of Chang-Beom Eom at the University of Wisconsin-Madison for growing all of the samples used in the research presented here. Many thanks also to my committee members for their advice and feedback.

1.0 Introduction

Quantum theory provides a unified framework for understanding the fundamental properties of matter. However, there are many quantum systems whose behavior is not well understood because the relevant equations are too hard to solve using known approaches. For example, high-temperature superconductivity, in copper-oxides or other materials, was neither predicted nor is it currently understood in the same way that, for example, the band structure of silicon is known. One avenue for exploring these systems of interest is quantum simulation. The idea was first proposed by Feynman in 1982 [1], and involves the use of a configurable quantum system in which the Hamiltonian can be mapped onto a system of interest. The simulator can be used to compute the properties of interest, in order to gain insight into the quantum nature of matter. It has been shown that Feynman's original idea, "that quantum computers can be programmed to simulate any local quantum system", is correct [2], and that such a quantum simulator could be used to gain insight, for example, into the problem of high-temperature superconductivity [3].

The motivation for the work described here is to develop the tools necessary to build a solid-state quantum simulation platform. Complex oxide materials give access to important phases of matter, such as superconductivity, where the model Hamiltonians (e.g., 2D Hubbard model) are challenging to understand theoretically, while their nanoscale reconfigurability makes it possible to engineer new forms of quantum matter with extreme nanoscale precision [4, 5].

1.1 QUANTUM COMPUTATION AND QUANTUM INFORMATION

The ability to understand and harness complex quantum systems is at the forefront of much of today's research. The majority of these quantum systems cannot be simulated using classical computational techniques. Simulating the full time-evolution of an arbitrary quantum system with a classical computer is intractable, requiring resources that scale exponen-

tially with the size of the system [1]. For example, using classical bits to describe the state of N spin-$\frac{1}{2}$ particles requires 2^N bits. Recording the state of a system of $N = 50$ particles would require $2^{50} \sim 1 \times 10^{15}$ bits, and doing calculations of this size with classical computers becomes nearly impossible.

These problems (and many more) could, however, be efficiently solved using a quantum computer. Analogous to the classical 'bit', quantum computation is built on the concept of a 'qubit' or a quantum bit. The power of the qubit comes from its quantum nature and its ability to be in a superposition of states. Analogous to the bit, the qubit can be in the state $|0\rangle$ or $|1\rangle$, but it can also be in a linear combination of these two states,

$$|\psi\rangle = \alpha|0\rangle + \beta|1\rangle, \tag{1.1}$$

where α and β are complex numbers. These numbers, or amplitudes, represent the probability of measuring the state $|\psi\rangle$ and finding it in either the state $|0\rangle$ or $|1\rangle$. A measurement of $|\psi\rangle$ will yield the state $|0\rangle$ with a probability of $|\alpha|^2$ and $|1\rangle$ with a probability of $|\beta|^2$. A more complete discussion of this topic can be found in Ref [6].

The full set of problems that could benefit from a universal quantum computer is not known, but there are many possible applications [7]. Being able to efficiently simulate nature would provide insight into a variety of fields involving strongly correlated systems [8] including: condensed-matter physics, quantum chemistry, high-energy physics, atomic physics, and cosmology. Quantum computation also has implications for cryptography (with the ability to efficiently factor large numbers) [9], quantum sensing [10], communication, and many other applications [11]. There are many physical implementations of a qubit and a quantum computer. It is not yet clear what form the first universal quantum computer will take, and building them is the focus of intense research. The full implementation of a gate-based universal quantum computer with fault tolerant logical qubits is still many years in the future [11].

An alternative to a universal quantum computer may be the more specialized approach of quantum simulation. While not as versatile as a universal quantum computer, quantum simulations may be a mid-range goal that can give insight into some specific (but still very

interesting) problems [12, 13]. In the the same way that analog classical computers preceded digital classical computers.

1.1.1 Quantum simulation

Quantum simulation requires a quantum system that can be precisely controlled and whose Hamiltonian can be mapped onto the system of interest. These systems can be studied experimentally to gain insight into the quantum nature of matter. A schematic of this process is shown in Fig. 1.

There are a variety of systems that have been developed for quantum simulation including; ultracold atomic lattices [14, 15, 16], ion trap arrays [17, 18, 19] (which can simulate spin systems readily), superconducting Josephson junction arrays [20, 21, 22], photonic systems [23, 24, 25], and various solid-state approaches[26, 27, 28, 29]. Platforms capable of quantum simulation of Fermi-Hubbard models would be of enormous value in condensed matter physics and beyond.

Quantum simulators have reached the point where they are able to study the dynamics of quantum systems that are beyond the reach of classical computation. Several groups have simulated an Ising-type model of ~ 50 spins using ultracold atoms [30] and trapped ions [31], a problem that cannot currently be solved using classical computational methods.

1.1.1.1 Quantum simulation platforms Perhaps the most extensively studied platform currently being used for quantum simulation are ultra cold atoms. A large number of atoms can be trapped and controlled using standing waves of light and magnetic fields [15]. These systems are well-described by the Hubbard model and have been used to simulate a wide range of many-body Hamiltonians, including the Fermi-Hubbard model [32]. More details can be found in Ref. [15], which details the "Cold atom Hubbard toolbox". While the atoms trapped in ultracold atoms are at nominally very low temperatures (nanokelvins), cooling to low effective temperatures where correlated ground states occur is still a challenge in these systems.

Solid-state platforms for quantum simulation have the advantage that they can naturally

3
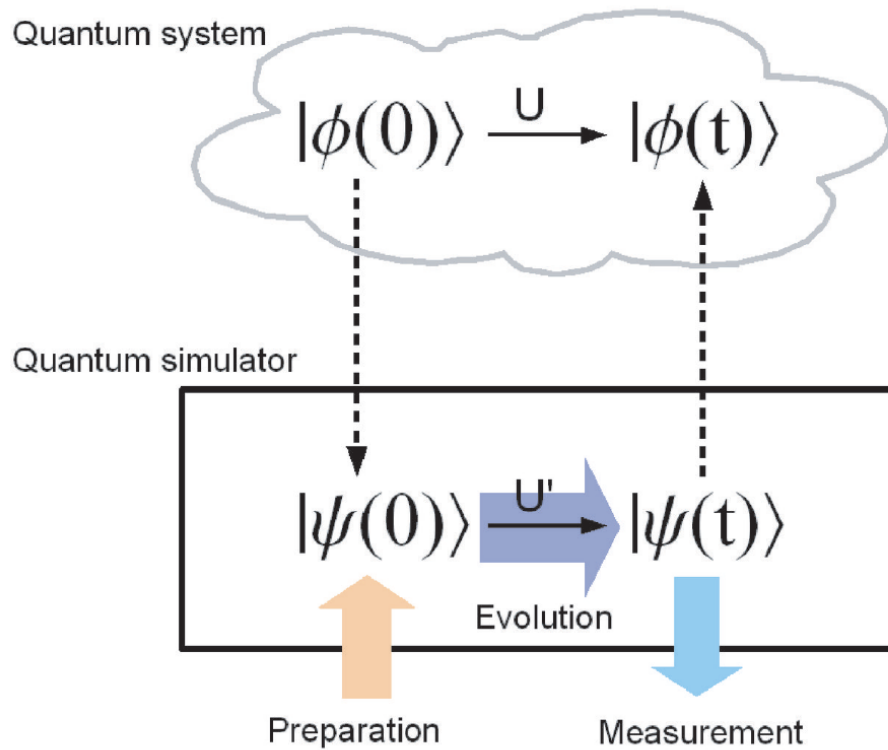
Figure 1: Schematic of a quantum simulator simulating a quantum system of interest. There is a mapping between the states of the simulator, which can be precisely controlled and measured, and the quantum system. Reproduced from Ref [13].

4

support the quantum phases of interest, such as superconductivity. These platform have a range of sizes and interactions and are in some cases real electronic devices that can be readily integrated with other systems. The disadvantage is that the precise Hamiltonian of these systems is often not well understood.

1.2   COMPLEX OXIDE HETEROSTRUCTURES

Complex oxide systems, specifically those based on $SrTiO_3$, possess a wide range of magnetic and electronic properties including: superconductivity, magnetism, ferroelectricity, and ferroelasticity [33]. Complex oxide materials offer new opportunities to create a platform for quantum simulation in a solid-state environment. Their complexity gives access to important quantum phases of matter, such as superconductivity, where the model Hamiltonians (e.g., 2D Hubbard model) are challenging to understand theoretically.

1.2.1   The $LaAlO_3$/$SrTiO_3$ heterointerface

The work described here is based on the properties of the complex oxide heterostructure $LaAlO_3$/$SrTiO_3$ [34] (Fig. 3). We will briefly describe some of the relevant properties here and more details can be found in Ref. [33].

$LaAlO_3$/$SrTiO_3$ is composed of two wide-bandgap insulating oxide materials; $LaAlO_3$, $E_g \sim$ 5.6 eV and $SrTiO_3$, $E_g \sim 3.2$ eV. The two materials have a small lattice mismatch with a lattice spacing of 3.789 Å and 3.905 Å, respectively. When a thin layer (> 4 unit cells (u.c.)) of (001)-oriented $LaAlO_3$ is grown on a TiO_2-terminated [35] $SrTiO_3$ substrate the interface becomes conductive with a carrier mobility exceeding $10,000$ cm^2 V^{-1} s^{-1} [34]. The interface of $LaAlO_3$ grown on an SrO-terminated $SrTiO_3$ substrate is expected to be a p-type interface but is found to be insulating. The two dimensional electron system (2DES) at the TiO_2 terminated $LaAlO_3$/$SrTiO_3$ interface is very strongly confined, extending only ~ 10 nm into the $SrTiO_3$ substrate at both room temperature [36] and cryogenic temperatures $T = 8$ K [37].

The origin of the emergent conductivity at the $LaAlO_3$/$SrTiO_3$ interface, and its depen-

5
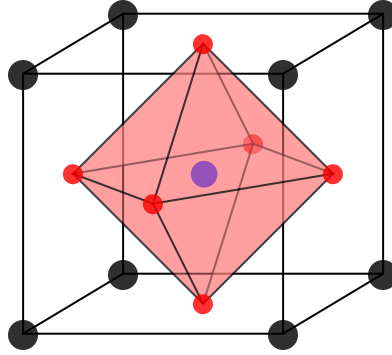
Figure 2: Perovskite crystal structure of many of the complex oxide materials, including $LaAlO_3$ and $SrTiO_3$. Black and blue atoms are the cations, and the red atoms are the anions (usually oxygen).

dence on a critical thickness of the $LaAlO_3$ layer, is still not fully understood. Possible explanations are: a polar catastrophe effect [38], Oxygen vacancies [39, 40, 41], atomic interdiffusion [42], structural deformation [43], and some possible combination of these or other effects [44].

The most widely cited explanation for the origin of the conductivity at the interface and the need for critical thickness of the $LaAlO_3$ layer, is the polar catastrophe [38]. This is due to the polarity of the different layers of $LaAlO_3/SrTiO_3$. Both $LaAlO_3$ and $SrTiO_3$ have a perovskite crystal structure (Fig. 2). The $LaAlO_3$ is made up of alternating layers of LaO and AlO_2, and the $SrTiO_3$ is made up of alternating layers of SrO and TiO_2. Both of the layers in $SrTiO_3$ are charge neutral. But the layers of $LaAlO_3$ have alternating charges of +1 (LaO) and -1 (AlO_2), as shown in Fig. 4. For a TiO_2-terminated $SrTiO_3$ substrate the alternating charges of $LaAlO_3$ lead to an electric field, and a diverging potential with increasing $LaAlO_3$ thickness. In order to prevent this diverging potential, the "polar catastrophe", the system undergoes an electronic reconstruction, transferring 1/2 an electron per 2D unit cell from the surface to the interface (Fig. 4). This causes the electric field to oscillate around zero and the potential to no longer diverge. Similarly, if the $SrTiO_3$ is terminated with an SrO layer the polar layers of $LaAlO_3$ cause a negatively diverging potential which can be avoided by removing 1/2 an electron from the last SrO layer. The polar catastrophe theory can also explain the existence of the critical thick-
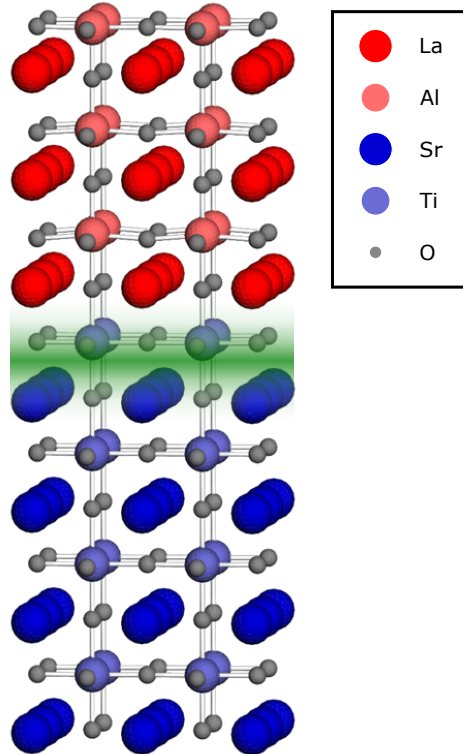
Figure 3: LaAlO$_3$/SrTiO$_3$ structure. SrTiO$_3$ substrate with a few unit cells of LaAlO$_3$ grown on top. Both materials have perovskite crystal structure. Under the right conditions the interface can host a high mobility 2D electron liquid (highlighted in green).

ness dependence of the conductivity. When the LaAlO$_3$ layer reaches the critical thickness (4 u.c.) there is a crossover of the LaAlO$_3$ valence band maximum and SrTiO$_3$ conduction band minimum [45, 46].

The polar catastrophe is however not the whole story. The polar catastrophe model predicts that the interface would have an electron density of $n = 3 \times 10^{14}$ cm^{-2}, but the interface is found to have carrier concentrations an order of magnitude smaller [47, 48]. There are also other types of interfaces such as (110)-oriented [49] and amorphous [50] LaAlO$_3$ that can produce conductive interfaces but do not have layers with alternating charge.

Another possible explanation for the conductivity of the LaAlO$_3$/SrTiO$_3$ interface is the presence of oxygen vacancies. Each oxygen vacancy would provide a charge of $2e$. The number of oxygen vacancies in LaAlO$_3$/SrTiO$_3$ can be controlled with the oxygen partial pressure and temperature during growth. Calculations suggest that the most likely source of conductivity is oxygen vacancies in the LaAlO$_3$ surface layers which leads to in-gap states in the LaAlO$_3$ that can transfer charge to the SrTiO$_3$ conduction band [39, 40, 41]. This theory can also explain the critical thickness due to the fact that the formation of oxygen vacancies at the surface becomes more favorable with increasing LaAlO$_3$ thickness. The source of the emergent conductivity at the interface is the subject of ongoing study.

Conduction at the LaAlO$_3$/SrTiO$_3$ interface occurs in the Ti t_{2g} orbitals. Confinement from the interface splits the d_{xy} band from the d_{xz}/d_{yz} bands, making the d_{xy} band the lowest conducting band [51]. The band structure of LaAlO$_3$/SrTiO$_3$ has been measured using angle-resolved photoemission spectroscopy (ARPES) [52, 53].

1.2.1.1 Electronically tunable interface The metal-insulator transition at the LaAlO$_3$/SrTiO$_3$ interface can be tuned both by controlling the thickness of the LaAlO$_3$ layer (Fig. 5A) and electronically (Fig. 5B) [54]. With three unit cells or less of LaAlO$_3$ the interface in insulating. At four unit cells, and above, the interface becomes conducting with a typical electron density of 10^{13} per cm^2.

When the LaAlO$_3$/SrTiO$_3$ is right below the critical thickness (3 u.c.), so that the interface is naturally insulating, application of a positive gate voltage to the back of the SrTiO$_3$ substrate can drive the interface into a conducting state. This conducting state persists even when the
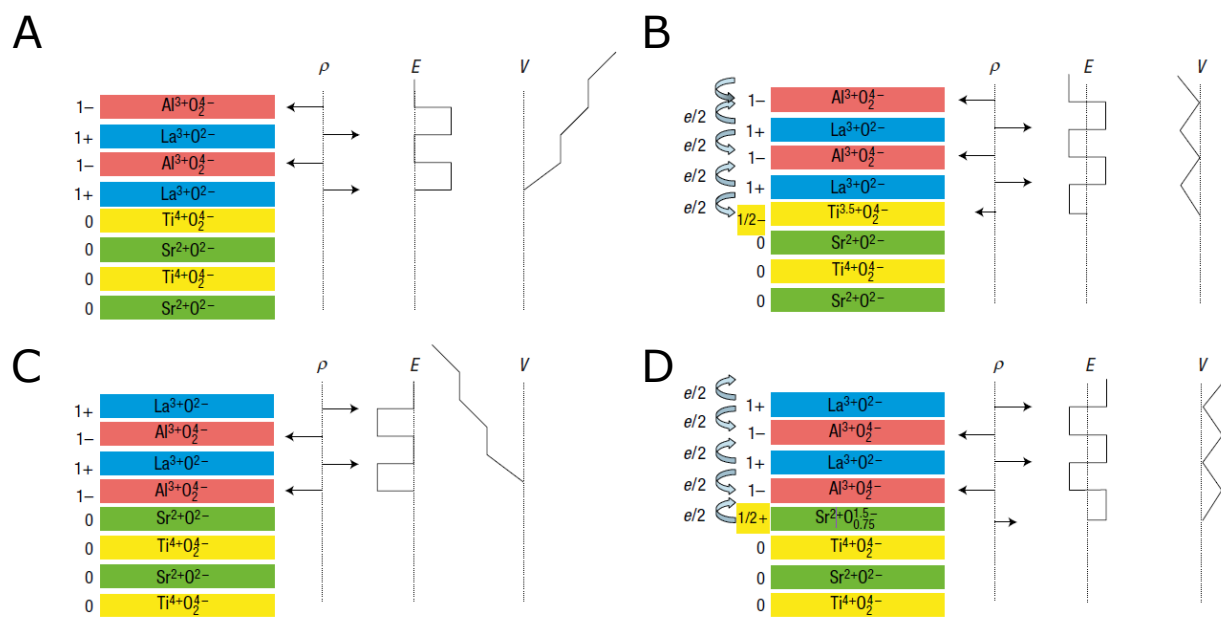
Figure 4: Illustration of the polar catastrophe which is one possible mechanism for the interface conductivity of LaAlO$_3$/SrTiO$_3$. The layers that make up SrTiO$_3$ are charge neutral, but the layers of LaAlO$_3$ have alternating charge which leads to a diverging potential. To prevent this the system may undergo an electronic reconstructing and transfer charge to the interface. **(A)** and **(B)** depict TiO$_2$ terminated LaAlO$_3$/SrTiO$_3$ and **(C)** and **(D)** depict SrO terminated LaAlO$_3$/SrTiO$_3$. (A and (C) show the diverging potential due to the alternating polarization in the LaAlO$_3$ layers. (B) and (D) show how this polar catastrophe is avoided by the charge transfer to the interface. Adapted from Ref. [38].
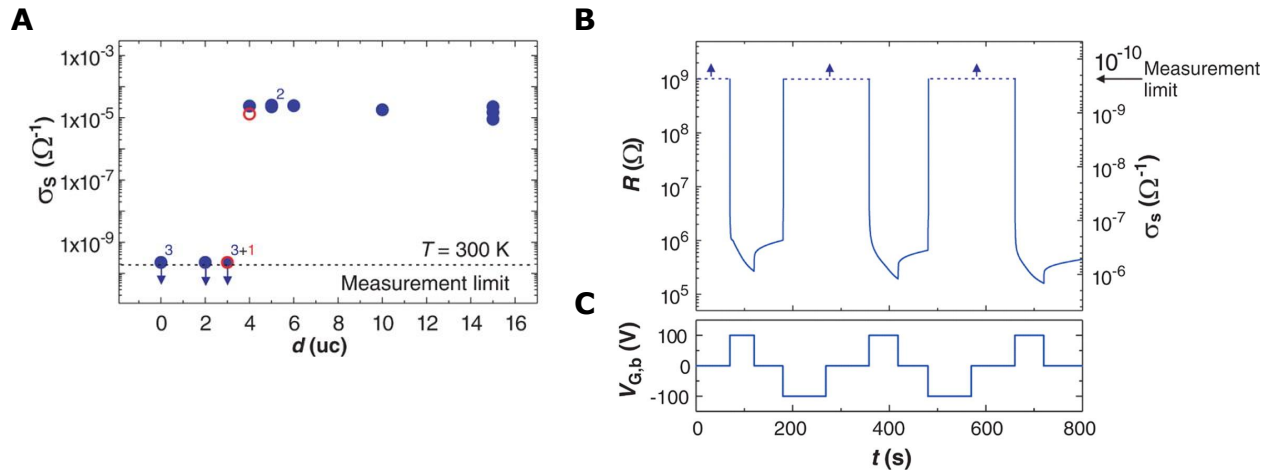
Figure 5: **(A)** Sheet conductance as a function of the number of LaAlO$_3$ unit cells showing that there is a critical thickness of 4 u.c. at which the interface will transition from insulating to metallic. **(B)** Gate tunable metal to insulator transition at the critical thickness. Sheet resistance as function of time changes with an applied gate voltage **(C)**. Positive voltages drive the interface to a conducting state and negative voltages restore the insulating state. States persist even when the voltages are returned to zero. Adapted from Ref. [54].

positive voltage is removed. A negative voltage restores the interface to the insulating state.

Applying a voltage to the bottom of the $SrTiO_3$ substrate globally controls the conductivity of the interface. The conductivity can also be controlled on a much smaller scale by applying a voltage to the surface with a conductive atomic force microscope tip [4, 5]. This technique will be discussed in more detail in Chapter 2.

1.2.1.2 Emergent properties at the $LaAlO_3$/$SrTiO_3$ interface   The $LaAlO_3$/$SrTiO_3$ interface also exhibits many other interesting properties. The interface becomes superconducting at $T \sim 200$ mK [55]. Tunable spin orbit coupling [47, 48], and magnetism [56, 57] have also been observed.

The superconductivity at the $LaAlO_3$/$SrTiO_3$ interface is inherited from the $SrTiO_3$ substrate. Superconductivity in $SrTiO_3$ was first observed in 1964 [58] in oxygen-reduced $SrTiO_3$ with a $T_c = 250$ mK. $SrTiO_3$ is a superconducting semiconductor with a carrier concentration of only 10^{15} cm^{-3} [59]. It also exhibits a dome shape characteristic of high T_c superconductors where the critical temperature depends on the carrier concentration [60]. The nature of the superconductivity and the pairing mechanism in $SrTiO_3$ are open questions.

Transport and other properties at the $LaAlO_3$/$SrTiO_3$ interface are found to be highly inhomogeneous. Low temperature scanning probe measurements have revealed that ferroelastic domains greatly affect the transport at the interface [61, 62]. Ferroelastic domains can form at low temperatures along the crystallographic axes of the material. These domains form due to the cubic-to-tetragonal antiferrodistortive transition that occurs in $SrTiO_3$ at $T = 100-110$ K [63]. The nanometer scale domain walls that form between the ferroelastic domains are highly conductive [61]. It has been found that superconductivity exists only at the boundaries of conductive regions at the interface, which correspond to ferroelastic domain boundaries [64].

1.2.2 Nanostructures at the $LaAlO_3$/$SrTiO_3$ interface

There are several methods for creating mesoscopic devices at the $LaAlO_3$/$SrTiO_3$ interface. It is possible to take advantage of the critical thickness dependence of the metal-insulator transition of the interface to pattern devices at the interface. E-beam lithography can be used

to create conducting channels with widths of several hundred nanometers [65, 66]. Features as small as 50 nm can be created using low energy beam ion radiation [67]. Field effect gating using split gates can be used to define a constriction at the interface [68, 69]; these will be discussed in more detail later in this chapter. One-dimensional structures can also be created using conductive atomic force microscope lithography (c-AFM) or surface charge writing [4, 5, 70, 71] which will be discussed in detail in Chapter 2.

1.3   1D TRANSPORT

One-dimensional quantum transport is fascinating in its own right, but it can also be regarded as a building-block for a variety of quantum devices. Arrays of quantum wires can be used to construct topological states of matter, including fractional quantum hall states [72, 73]. Many of the experiments described in this thesis will involve transport through 1D or quasi 1D systems.

1.3.1   Ballistic transport and quantized conductance

Transport is considered to be ballistic when the elastic mean free path is much larger than the length and width of the device. This occurs in systems with increased confinement in the direction transverse to the transport which results in an increase in the spacing between the subbands. A schematic of a 1D channel is shown in Fig. 6A. The 1D channel is connected to reservoirs with chemical potentials μ_L and μ_R. Transverse modes travel in the x direction along the channel. The parabolic energy dispersion is given by,

$$E_n(k_x) = E_n + \frac{\hbar^2 k_x^2}{2m^*},$$

(1.2)

where E_n are energies due to the transverse modes in the channel. The energy dispersion is plotted in Fig. 6B. Positive k_x values represent states travelling from left to right and negative k_x values represent states travelling from right to left.
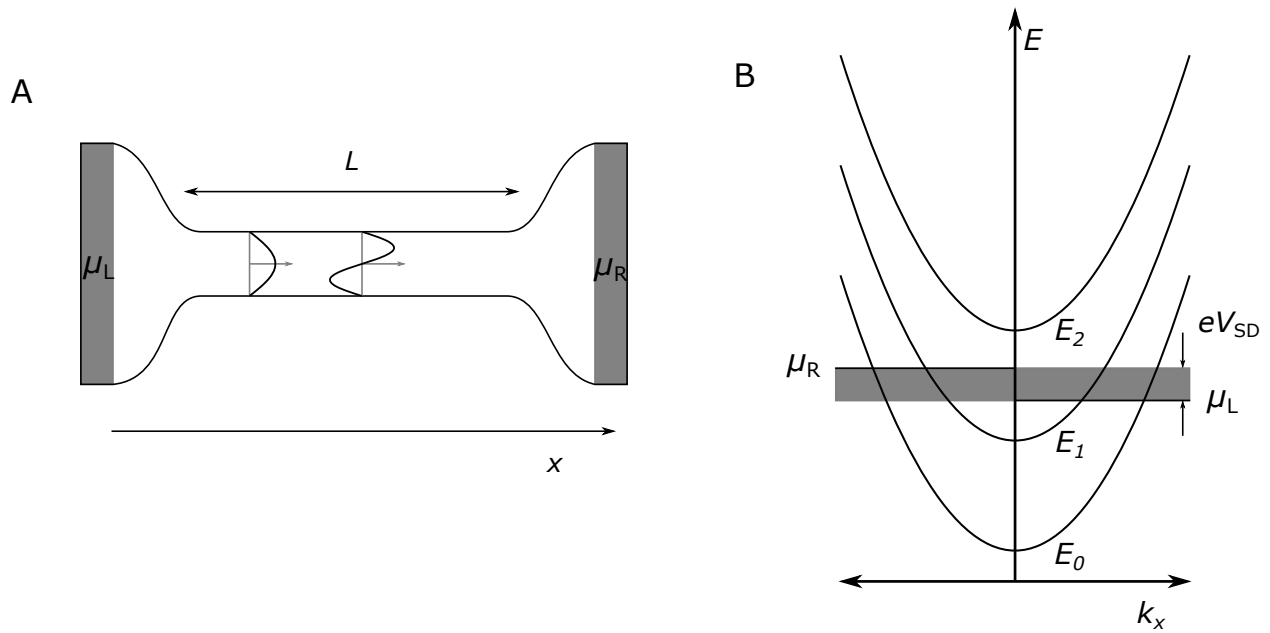
Figure 6: **(A)** Schematic of 1D channel connected to reservoirs at chemical potentials μ_L and μ_R. Transverse modes are depicted in the channel and propagate in the x direction. **(B)** 1D channel dispersion relation. The parabolic dispersion relation is given in Eq. 1.2. Positive k_x values denote states travelling from left to right, and negative k_x states propagate from right to left. The voltage applied between the reservoirs gives the bias window and is denoted by the grey shaded bar. Adapted from Ref. [74].

13

To determine the contribution to the current through the channel from each individual subband we can write

$$I = \frac{-e}{L} \int_{\mu_{\text{R}}}^{\mu_{\text{L}}} DOS(E) v \cdot dE, \tag{1.3}$$

where $v = \frac{1}{\hbar} \frac{\partial E}{\partial k}$ is the group velocity and the density of states is: $DOS(E) = \frac{L}{2\pi} \frac{\partial k}{\partial E}$. This gives,

$$I = \frac{-e}{L} \int_{\mu_{\text{R}}}^{\mu_{\text{L}}} \frac{\hbar L}{2\pi} \cdot dE = \frac{e}{h}(\mu_{\text{R}} - \mu_{\text{L}}), \tag{1.4}$$

the difference in chemical potential is: $\mu_{\text{R}} - \mu_{\text{L}} = e V_{\text{SD}}$, which gives the conductance from each individual subband as:

$$G_0 = \frac{e^2}{h}. \tag{1.5}$$

For a more complete derivation of the conductance quanta see Ref. [74].

Transport through a coherent quantum conductor can be described by Landauer's formula, $G = (e^2/h) \sum_i T_i(\mu)$, where each energy subband available at chemical potential μ contributes one quantum of conductance e^2/h with transmission probability $T_i(\mu)$. The transmission probability is given by $T_i(\mu) = \bar{T} F_{\text{T}}(\mu - E_i)$ where $\bar{T}$ encompasses any tunneling resonances, cavity interference effects, or backscattering processes, $F_{\text{T}}(E)$ is a thermal broadening from the Fermi distribution function of the leads at a finite temperature, and E_i represents the energy minimum of the ith electron subband [75]. For simplicity, we assume that $\bar{T}$ is independent of energy. Within this framework, the conductance increases in steps of e^2/h every time the chemical potential crosses a subband energy minimum. Transport through the channel is ballistic and dissipationless, however, the measured resistance is given by $R = h/(Ne^2)$, where N is the number of occupied subbands. The apparent contradiction between dissipationless transport within the waveguide and finite resistance was understood by Landauer and put on rigorous footing by Maslov and Stone, who developed a Luttinger liquid model of energy dissipation within the leads [76]. However, in experiments, even the cleanest nonchiral systems do not have infinite scattering lengths, each subband can backscatter electrons, leading to a suppression which can be modeled as $\bar{T} = \exp(-L/L_i)$ [77], where L is the channel length and L_i is the mode-dependent scattering length. When $L_i \sim L$, the system is in the

ballistic or quasi-ballistic regime, and when $L_i >> L$, the system enters a quantized ballistic regime.

1.3.1.1 Quantum point contacts

Conductance quantization was first observed in quantum point contacts (QPC) created in GaAs/AlGaAs heterostructures [78, 79]. The point contacts are defined using metallic split gates that deplete the two dimensional electron gas (2DEG) when a negative voltage is applied. A schematic of the QPC device is shown in the inset in Fig. 7. As the voltage applied to the gates is made more negative the width of the point contact decreases. The conductance steps can be explained by assuming quantized transverse momentum in the point contact. As the channel width increases more transverse channels become available and the total conductance is given by Landauer's formula. When each new channel becomes available the conductance increases by $2e^2/h$ as can be seen in Fig. 7. The factor of two comes from the spin degeneracy of the system in zero magnetic field.

Quantized conductance has been observed in several complex oxide systems. Quantum point contacts have been created created in MnZnO/ZnO heterostructures [80]. Using a split-gate geometry a 1D quantum wire device was created at the interface which exhibited quantized conductance steps in units of $2e^2/h$ at zero magnetic field. An interesting feature seen in the transport of these devices was the presence of the "0.7 anomaly", an indication of strong electron-electron interactions in the system.

Superconducting quantum point contacts have been created at the 12 u.c. $LaAlO_3/SrTiO_3$ interface using a similar split gate geometry [68]. Well-quantized conductance steps were observed in a constriction at the $LaAlO_3/SrTiO_3$ interface, which could provide a platform for studying topological superconductivity in oxide 2DEGs [69]. Quantized conductance has been observed at the $SrTiO_3$ surface using a gate-tunable superconducting weak link [81].

Quantized conductance has also been observed in several 1D nanowire devices at the $LaAlO_3/SrTiO_3$ interface, including in edge defined $LaAlO_3/SrTiO_3$ nanowires created by alternating regions of 1 and 3 u.c. $LaAlO_3$ [82], and 1D electron waveguides created using conductive atomic force microscope lithography [83] which will be discussed in more detail in Chapter 3.
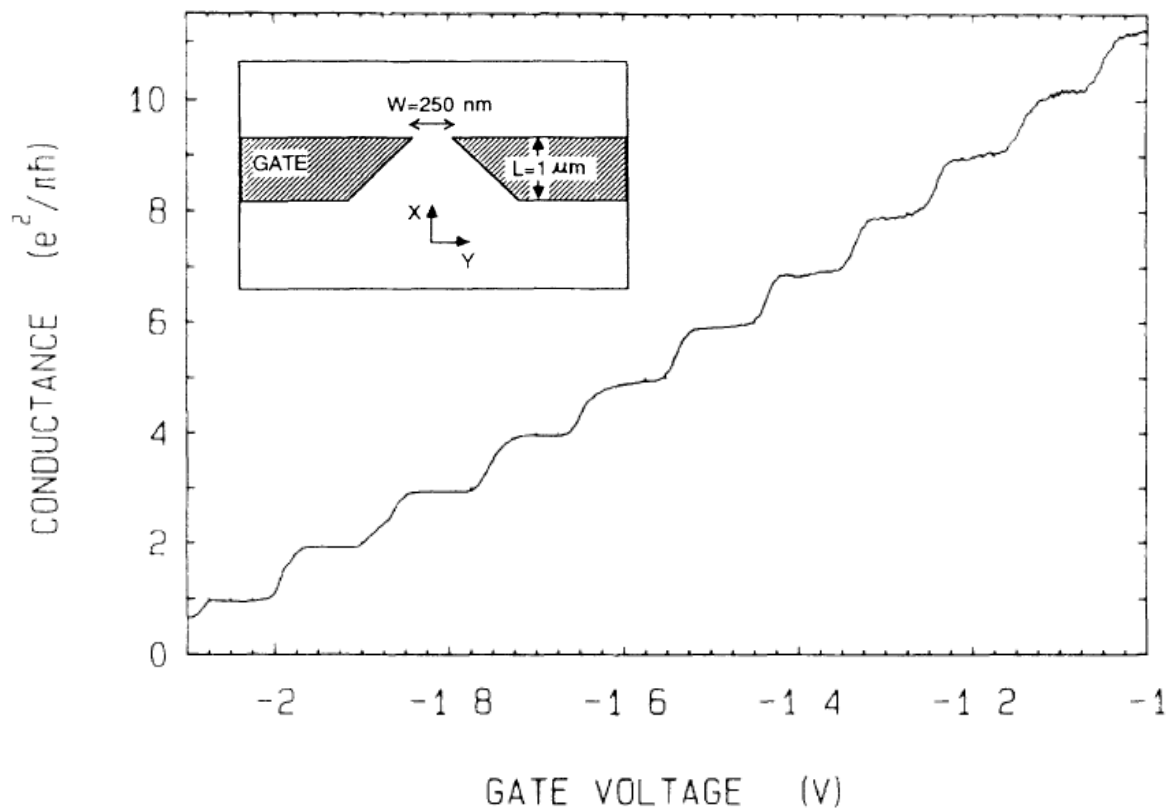
Figure 7: Conductance measured through a quantum point contact device in a GaAs/AlGaAs heterostructure at zero magnetic field. Conductance increases in steps of $2e^2/h$ when the voltage applied to the gates is reduced, increasing the width of the point contact. Inset shows a schematic of the device. $T = 0.6$ K. Adapted from Ref. [78].

1.4 CONTENT SUMMARY

In this thesis we describe experiments which explore 1D transport at the LaAlO$_3$/SrTiO$_3$ interface with the goal of developing a solid state quantum simulation platform. In Chapter 2 we will first discuss the experimental methods used. In Chapter 3 we will discuss a series of experiments to create and explore electron waveguides at the LaAlO$_3$/SrTiO$_3$ interface. Chapter 4 will discuss new Pascal phases with bound states of $n > 2$ electrons observed in the waveguide devices. And finally, in Chapters 5, 6, and 7, experiments are presented where 1D superlattice devices were created by adding periodic perturbation to electron waveguide devices. These devices exhibit dispersive features not present in control waveguides and are a first step towards developing a solid state quantum simulation platform.

2.0   Experimental methods

2.1   INTRODUCTION

This chapter will describe the experimental methods involved with creating the samples and devices used in the experiments discussed below. It will describe the fabrication and processing of the $LaAlO_3/SrTiO_3$ samples as well as the conductive atomic force microscope lithography used to create the devices at the $LaAlO_3/SrTiO_3$ interface. It will also briefly describe some of the methods used for characterizing and measuring these devices.

2.2   LaAlO$_3$/SrTiO$_3$

The devices used in the experiments described here are based on the complex oxide heterostructure $LaAlO_3/SrTiO_3$ which is discussed in Chapter 1. Below we will discuss more details about the sample and device fabrication specific to these experiments.

2.2.1   Sample growth

The $LaAlO_3/SrTiO_3$ samples used in the experiments described here were grown, by the Chang-Beom Eom group at the University of Wisconsin-Madison, using pulsed laser deposition (PLD) [84]. Pulsed laser deposition involves focusing a high intensity laser pulse on a target (single-crystal $LaAlO_3$) in a vacuum chamber. The target is vaporized by the laser pulse and forms a plume that settles onto the substrate (single-crystal $SrTiO_3$). The $SrTiO_3$ substrate is prepared by etching so that the surface is TiO_2-terminated with atomically flat terraces [35]. Samples are grown at $T = 550\,°C$ and oxygen pressure $P_{O_2} = 10^{-3}$ mbar. The thickness of the $LaAlO_3$ film is monitored during growth using high pressure reflection high-energy electron diffraction (RHEED) [85], the intensity of the RHEED signal oscillates as each unit cell is grown on the substrate. The samples used here are grown with 3.4 unit cells (u.c.), about 1.2 nm, of

LaAlO$_3$ on a TiO$_2$ terminated SrTiO$_3$ substrate. This thickness is right below the critical thickness (4 u.c.) at which the interface will transition from an insulating state to a conducting state. 3.4 u.c., the thickness that was empirically found to produce the best results, indicates that some parts of the LaAlO$_3$ are 4 u.c. thick and some are 3 u.c. thick. Atomic force microscope (AFM) images of the LaAlO$_3$ surface after growth show atomically flat terraces (Fig. 8).

2.2.2 Sample processing

In order to measure the conductivity of the LaAlO$_3$/SrTiO$_3$ interface the samples are patterned with a "canvas" that is a 30 μm by 30 μm area surrounded by electrodes that make electrical contact to the interface [86]. Standard photolithography techniques are used to create this canvas; the steps are illustrated in Fig. 9. First photoresist is spun onto the surface and exposed using a mask. The photoresist is developed and the sample ion milled to etch down to the interface. Next Ti /Au electrodes are deposited and liftoff of the photoresist leaves electrodes in contact with the LaAlO$_3$/SrTiO$_3$ interface. Gold is then deposited on the surface of the LaAlO$_3$ to trace the interface electrodes back to larger bonding pads which can be wire bonded to a chip carrier holding the sample (Fig. 10).

2.3 CONDUCTIVE ATOMIC FORCE MICROSCOPE LITHOGRAPHY

For all of the experiments described here we use a conductive atomic force microscopy (c-AFM) lithography technique to create conducting channels at the LaAlO$_3$/SrTiO$_3$ interface [4, 5]. A positively-biased atomic force microscope tip in contact with the LaAlO$_3$ surface locally switches the interface to a conducting state ("writes"), while a negative voltage restores the insulating state ("erases"). This writing (erasing) mechanism is attributed to the local protonation (deprotonation) of the LaAlO$_3$ surface [87, 88]. The protons create an attractive confining potential which defines a nanowire at the interface and can create structures with widths as small as 2 nm [4]. A schematic of the c-AFM writing/erasing process is shown in Fig.
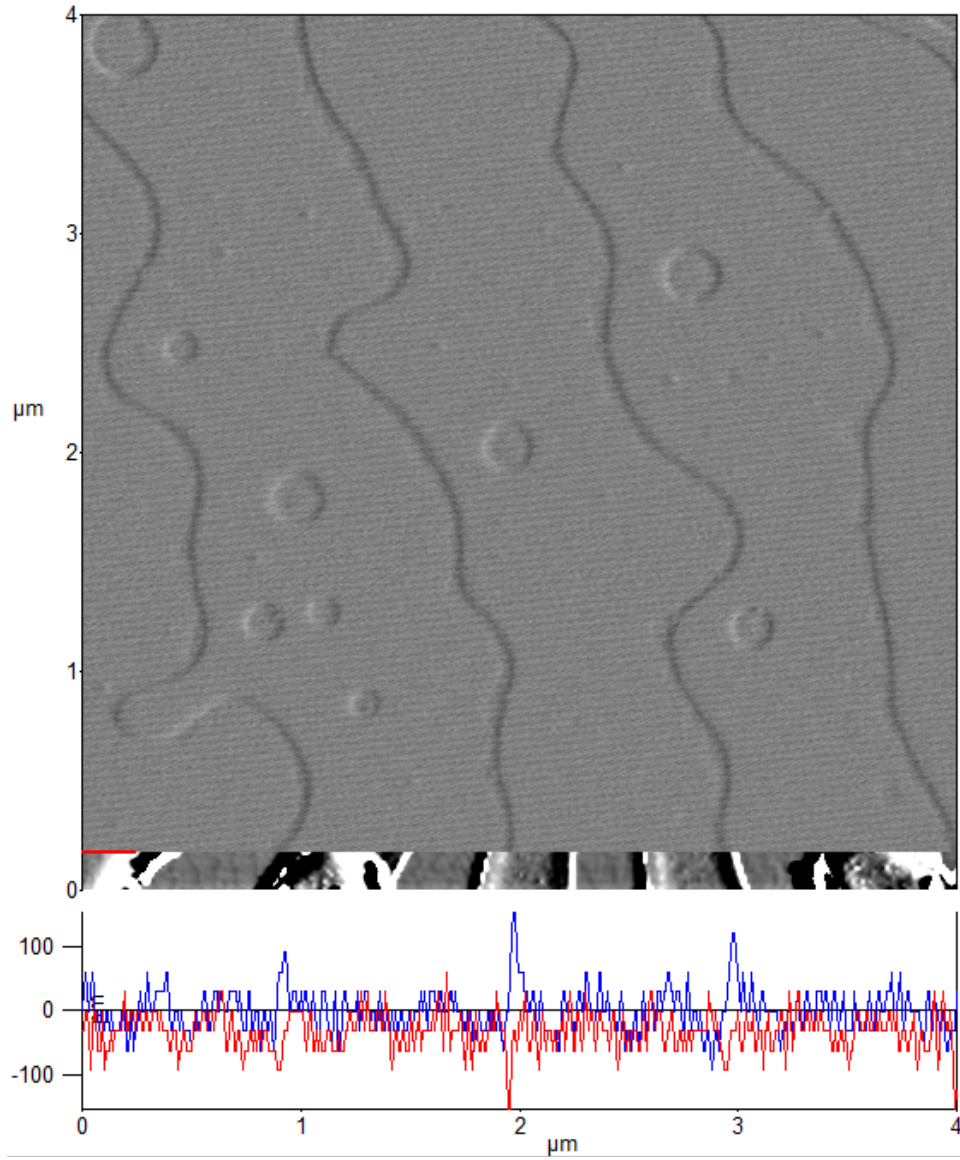
Figure 8: Atomic force microscope image of LaAlO$_3$ surface showing the atomically flat steps and terraces.
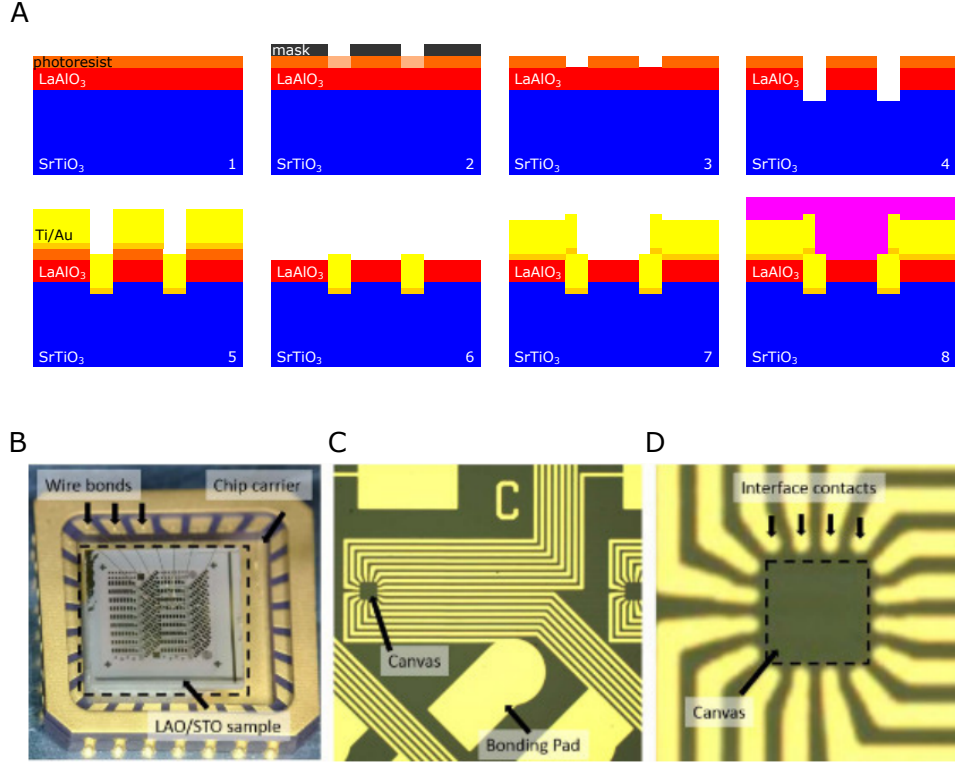
Figure 9: Schematic of the sample processing procedure. **(A)** shows the photolithography steps. Step 1 deposit photoresist, Step 2 apply mask and expose photoresist, Step 3 develop photoresist, Step 4 ion mill the sample, Step 5 deposit Ti/Au, Step 6 liftoff of photoresist, Step 7 pattern surface with Ti/Au, Step 8 oxygen plasma clean surface. **(B)** Processed $LaAlO_3$/$SrTiO_3$ sample mounted on a chip carrier, bonding pads leading to a canvas with interface contacts are wire bonded to the chip carrier. **(C)** $LaAlO_3$/$SrTiO_3$ surface showing gold traces from bonding pads to the interface electrodes of a canvas. **(D)** Canvas surrounded by 16 interface electrodes. Adapted from Ref. [86].
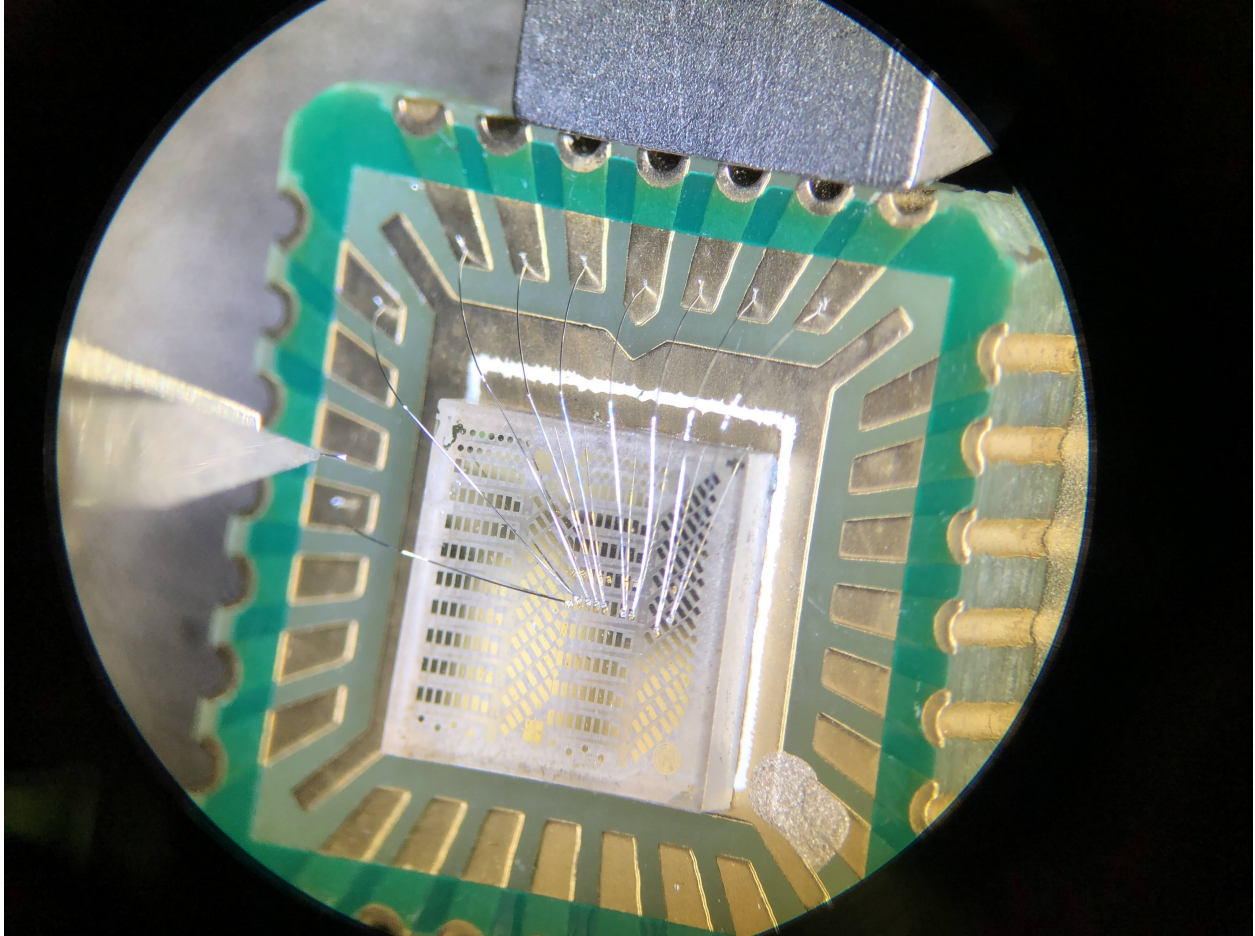
Figure 10: Image of an LaAlO$_3$/SrTiO$_3$ sample mounted on a chip carrier. Bonding pads which were patterned onto the LaAlO$_3$/SrTiO$_3$ sample are connected to the chip carrier with wire-bonds.

11. This technique is analogous to "modulation doping" used in semiconductor heterostructures: here the protons are physically separated from the conducting interface by the highly insulating $LaAlO_3$ layer which has a thickness of only 1.2 nm. The separation minimizes scattering from impurities, but the relative proximity allows for truly nanoscale control over the interface.

2.3.1 Protonation/water cycle mechanism

The "water cycle" is thought to be the mechanism behind the c-AFM lithography process [87]. Water from the air naturally adsorbs to the $LaAlO_3$ surface and subsequently dissociates into H^+ and OH^- ions. The positively-biased AFM tip will remove the negatively charged OH^- ions. This leaves only H^+ ions in the path of the AFM tip, which will attract electrons to the interface beneath the protonated surface and driving the interface from an insulating to a conducting state. The success of the writing process depends on control of the relative humidity of the AFM environment, typically a relative humidity of 30-40% is sufficient. After the c-AFM lithography is completed, the conductance of the devices naturally begins to decay if left in an ambient environment due to the continued adsorption of water onto the $LaAlO_3$ surface. Higher relative humidity levels tend to increase the rate of decay of the devices. The c-AFM lithography writing process is unsuccessful if performed in vacuum, dry air, nitrogen, or helium environments. Placing the sample in a dry environment or under vacuum after writing can significantly increase the lifetime of the device.

2.3.2 c-AFM details

An Asylum MFP-3D AFM was used for most of the c-AFM writing detailed here. The AFM tips used in a majority of the experiments are conductive doped silicon tips with a tip radius of curvature of 8 nm, and a force constant of 3 N/m (Aspire CFMR). Deflection setpoint of the AFM for writing in the MFP3D is about 0.1 V, corresponding to a force of $\sim$ 80 nN. There is a 1 GΩ resistor in series with the voltage being applied to the tip to limit the current applied to the sample. Too large of a current will cause the metal interface electrodes to melt or deform and potentially contaminate the $LaAlO_3$ surface.
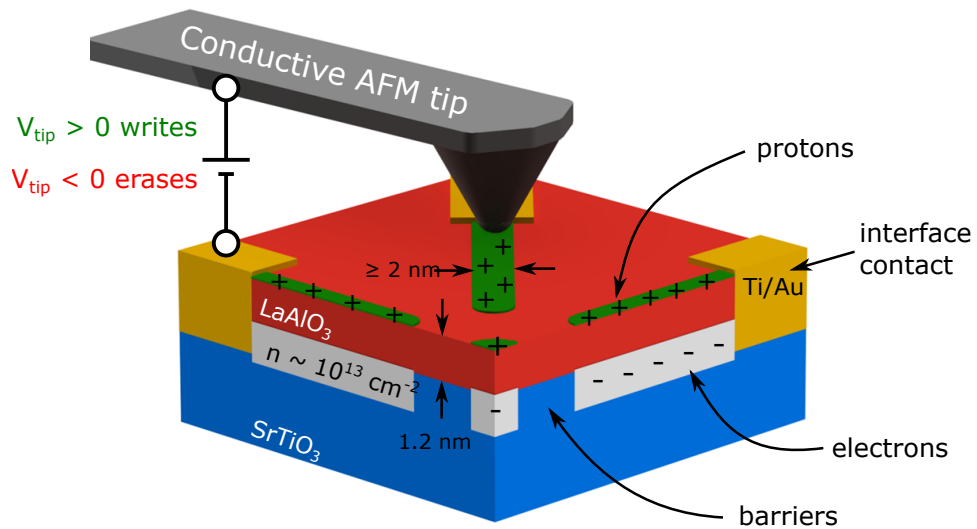
Figure 11: Schematic illustrating the c-AFM lithography technique [4, 5]. A positively-biased conductive AFM probe in contact with the LaAlO$_3$/SrTiO$_3$ surface will deposit a path of protons locally controlling the conductivity of the interface and switching it from an insulating to a conducting state. A negatively-biased tip will erase the conducting path removing the protons. This can be done selectively to create tunnel barriers in nanowires. The width of the nanowires varies depending on the writing parameters but can be as small as 2 nm.
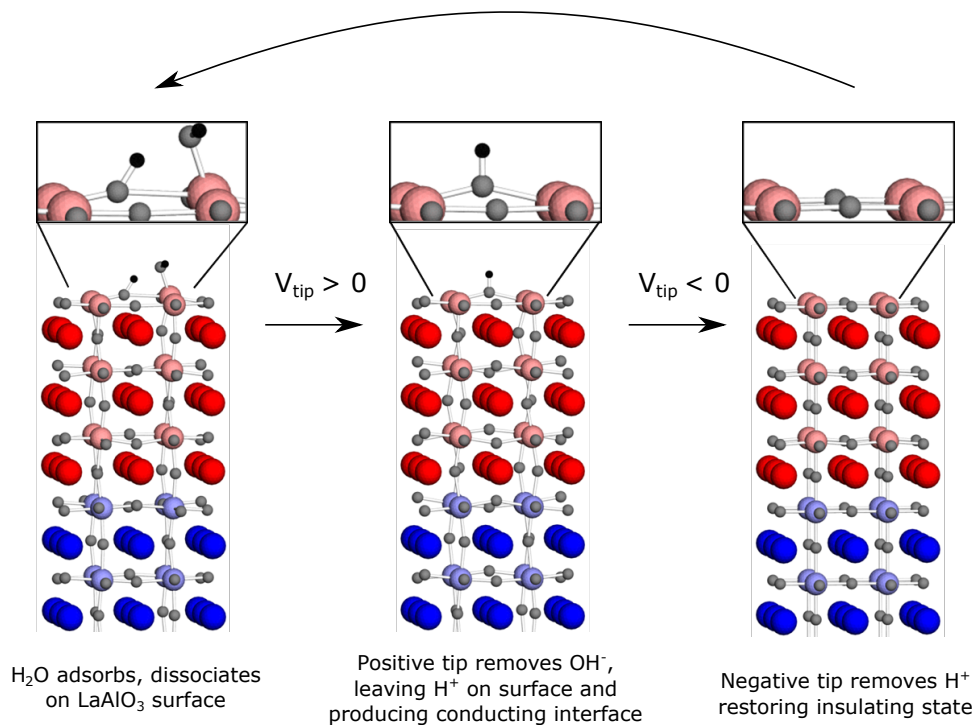
Figure 12: The water cycle mechanism is thought to be the method behind the c-AFM lithography writing process [87]. Here water from the air is adsorbed onto the $LaAlO_3$ surface and dissociates into OH^- and H^+ ions. The application of an AFM tip with a positive bias $V_{tip} > 0$ V will remove the negatively charged OH^-, leaving the H^+ on the surface and driving the interface from an insulating to a conducting state. An AFM tip with a negative bias $V_{tip} < 0$ V will remove the positively charged H^+ and restore the interface to an insulating state.

2.3.2.1 Erasing and cleaning the surface   We have found that a crucial step in the writing process is carefully erasing the area where the device will be written with the c-AFM tip. Successful erasing relies on (1) having a well-defined electrical potential between the tip and the interface and (2) having a spacing between passes of the tip smaller than the tip radius. It is important to attempt to maintain an electrical connection between the tip and the interface electrode because what matters is the relative electric potential between them. If the interface is not connected to a defined electrical potential it will float up to the value of the tip voltage, resulting in no (de)protonation of the surface. This requirement can be achieved by either (1) writing a conducting area that is connected to the interface electrodes before erasing, or (2) by using previously written structures to maintain an electrical connection between the area being erased and the interface electrodes, which are grounded during the erasing process.

For example, following method (2) for erasing (suitable if there is any existing conducting regions), first $V_{\text{tip}} \sim -15$ V is applied to the AFM tip. The deflection set point for erasing can be slightly larger than the setpoint for writing, applying slightly more force to the sample, 0.2 V. In the region surrounding the most crucial part of the device, the c-AFM tip is raster-scanned in a rectangular area with a line spacing of 2.5 nm in both the horizontal and vertical directions with a tip speed of $5-10$ µm/s. Next, a larger area is scanned with a line spacing of ~ 10 nm and similar tip speeds. Finally, an area extending to the interface electrodes is scanned with a larger spacing of around $25-50$ nm. Note that during this procedure electrical contact is always maintained with the interface electrodes by the previously written device.

After erasing the conductance between all of the interface electrodes should be zero. Once the erasing procedure is complete the AFM tip is typically replaced with a new tip to ensure that the tip is as small and uniform as possible. Some of the $\text{LaAlO}_3/\text{SrTiO}_3$ samples are light sensitive. After the sample has been erased it is only exposed to red light in order to prevent conductance in unwanted areas. Sometimes it is necessary to erase in other areas, between interface electrodes to eliminate any unwanted conductance. A negative voltage can also be applied to the bottom for the sample in order to eliminate unwanted conductance.

2.3.2.2 Device writing   The design for a device is created using a vector graphics software, typically Inkscape. The device design is loaded into a LabVIEW program developed in the

LevyLab that communicates with the AFM controller and controls the parameters for moving the tip according to the desired pattern and applying tip voltages.

A typical canvas and device are shown in Fig. 13. A device consist of several components: virtual electrodes, voltage and current leads, a main channel, and a side gate. Virtual electrodes are funnel-shaped conducting regions written at the interface electrodes to improve the connection of the device to the interface electrodes. These are typically written with a voltage $V_{tip} \sim 15 - 20$ V at a tip speed of 2 μm/s. These structures are essential for ensuring that good contact is made between the device and the interface electrodes. Voltage and current leads for the device are typically written with $V_{tip} \sim 10 - 15$ V at a tip speed of 400 nm/s. The writing parameters for the main channel of the device vary depending on the type of device being written. Most of the devices discussed here are written using $V_{tip} \sim 10$ V at speeds of $5-10$ nm/s. Highly transparent tunnel barriers for electron waveguide devices (Chapter 3) can be created in the main channel by retracing the same path and applying negative voltage pulses to the tip, $V_{tip} \sim -10$ V, at a speed of 5 - 10 nm/s. A local side gate can also be created using c-AFM lithography. It is typically written using similar parameters to the voltage and current leads. Cutting around the side gate using a negative tip voltage helps to reduce leakage between the gate and the device at low temperatures. The side gate is usually written in a rounded or loop shape, this may also help eliminate leakage between the side gate and the device by eliminating strong electric field lines due to sharp structures.

Writing 1D superlattice devices involves changing the pattern used to write electron waveguide device and also the voltage applied to the tip. For a vertical superlattice device (Chapter 5) a function generator is used to create a sine wave pattern for the tip voltage. When monitoring the resistance while writing, which will be discussed in more detail in the next section, it is possible to observe the change in resistance due to the applied sinusoidal tip voltage (Fig. 18B). Vertical superlattices writing is similar to electron waveguide devices. The path is first written with a constant voltage $V_{tip} \sim 10$ V and then traced a second time while applying the sinusoidal tip voltage, amplitudes of the sinewave voltage are generally less than the original tip voltage, typically ±5 V, and written with a tip speed of $5-10$ nm.

When writing a lateral superlattice device (Chapter 6) the vector graphics pattern for the device is changed so that the tip will trace a sine wave pattern on the $LaAlO_3$ surface and a
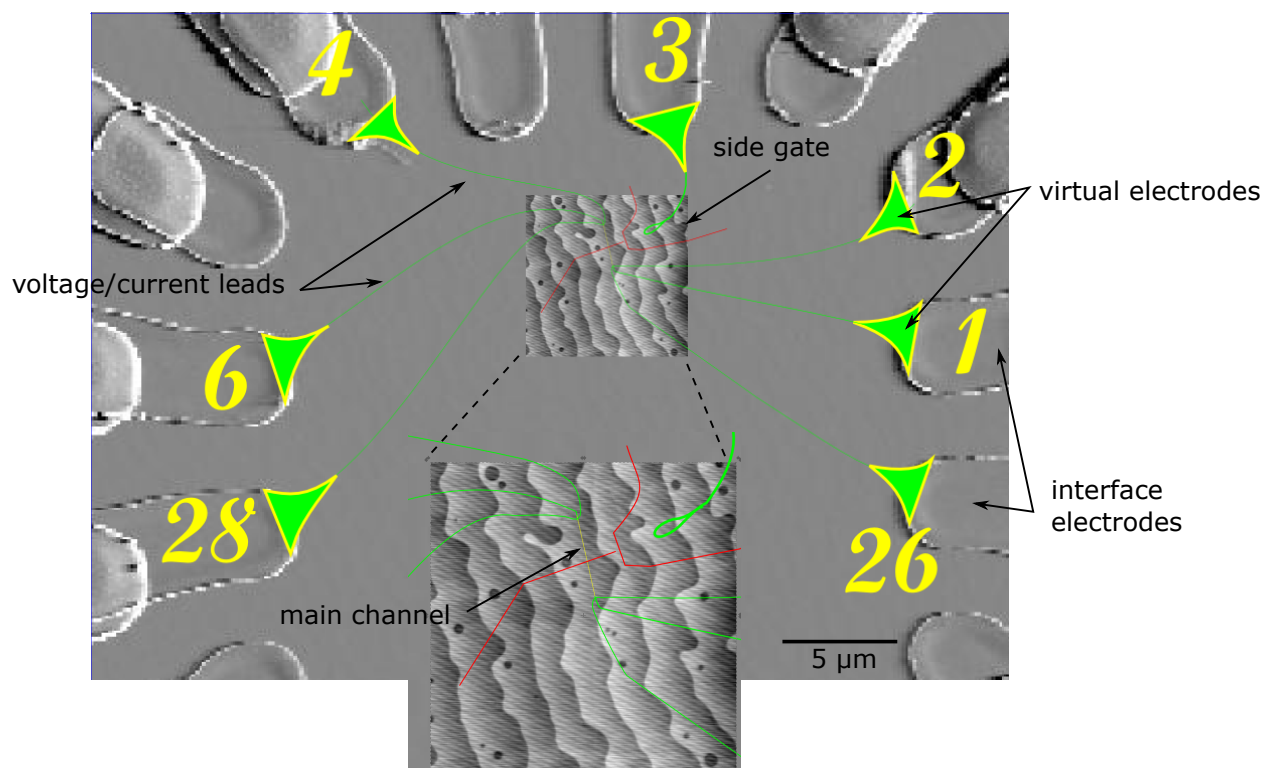
Figure 13: AFM image of a typical canvas and the Inkscape pattern used for c-AFM lithography. The pattern in green defines where the AFM tip moves to create the desired device. Funnel shaped virtual electrodes are created on the interface electrodes to ensure good electrical contact. The red lines are areas that were erased in order to help prevent leakage between the side gate and the device, and between the voltage leads before the main channel was written.
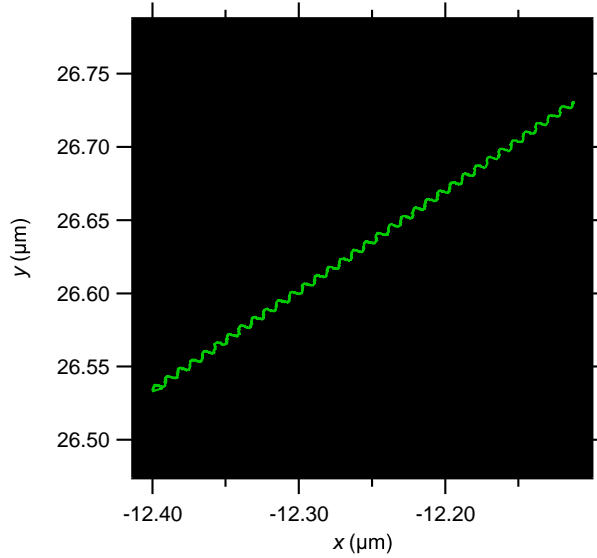
Figure 14: Measured AFM tip path during lateral 1D superlattice writing. A constant voltage is applied to the tip and the tip is moved in a sinusoidal path on the LaAlO$_3$ surface.

constant tip voltage is applied. The tip position is monitored during c-AFM writing (Fig. 14). Tip speeds of 5-10 nm are generally used. Writing chiral 1D superlattices (Chapter 7) combines these two techniques in quadrature. The measured tip position and voltage while writing a chiral 1D superlattice device is shown in Fig. 15. The tip voltage represented by the color of the curve varies sinusoidally 90° out of phase with the lateral tip motion. Chiral superlattices were written using two methods: with only one pass of the tip applying the sinusoidal voltage, or with a two pass method similar to the electron waveguide devices.

2.3.2.3 Monitoring device writing   The 2-terminal and 4-terminal conductance of the device is monitored during the writing process. Electrical contact is made to the sample by wire-bonding the interface electrodes to a chip carrier (Fig. 9B and Fig. 16) which is mounted in the AFM chamber.

While writing a device all of the interface electrodes are either grounded or being used to measure or source the current through the device, ensuring that the difference between the tip voltage and the interface is well defined and that the electrodes are not able to float up to

29
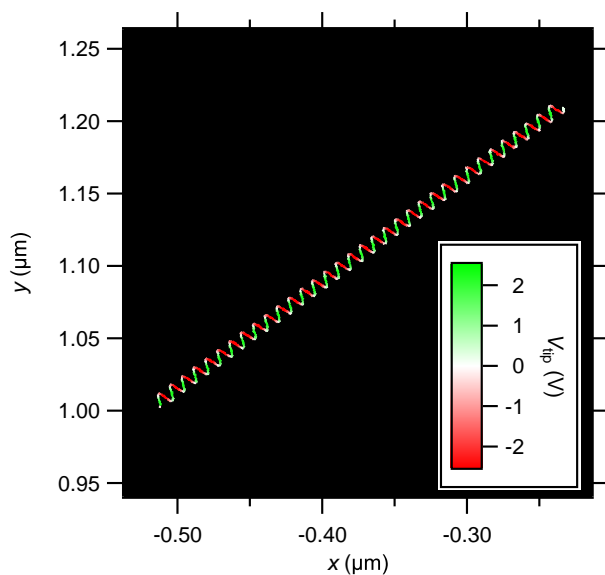
Figure 15: Measured AFM tip path and voltage during chiral 1D superlattice writing. The tip voltage is varied sinusoidally in quadrature (90° out of phase) with the tip position.
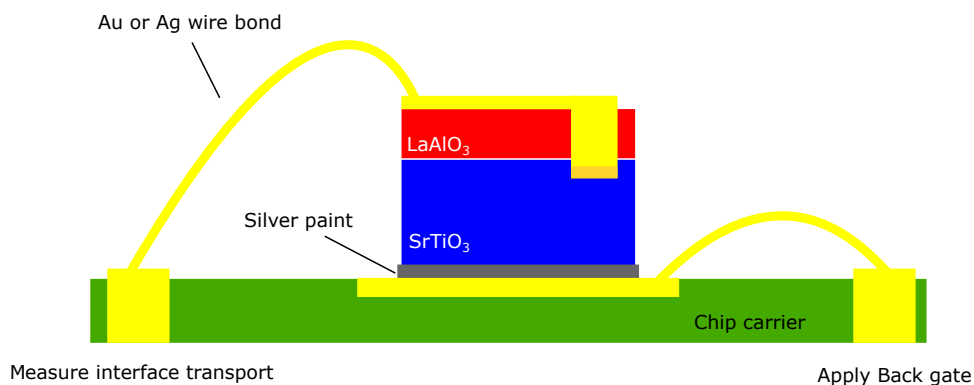
Figure 16: Schematic of an LaAlO$_3$/SrTiO$_3$ sample on a chip carrier to measure interface transport. The sample is attached to the chip carrier using silver paint, which also makes electrical contact between the SrTiO$_3$ substrate and the chip carrier. Gold bonding pads deposited on the LaAlO$_3$ surface are wire bonded to the chip carrier.

the value of the tip. The bottom of the SrTiO$_3$ substrate is typically grounded during writing.

Conductance between interface electrodes is monitored while writing using standard lock-in techniques. A 100 mV AC oscillation amplitude is applied to the sample at a frequency of $\sim$ 25 Hz. A conductance jump can be observed when the c-AFM lithography completes a path between the interface electrodes being monitored (Fig. 17). Typical 2-terminal conductance values of a nanowire of $\sim$ 10 μm are between 500 nS and 1 μS. Typical 4-terminal resistance measurements are $\sim$ 100 kΩ per 1 μm channel length.

When creating electron waveguide devices the change in the 4-terminal resistance of the main channel is monitored to determine the success of the highly transparent tunnel barriers (Fig. 18A). While writing the barriers the resistance of the device will increase temporarily to several MΩs then quickly decay back down to several hundred kΩs. After both barriers have been written the resistance of the main channel will typically have increased by several hundred kΩs.

The width of the nanowires depends on several parameters, including the voltage applied to the AFM tip (a larger voltage will produce a wider wire), and also on things such as the width of the AFM tip and the humidity of the AFM environment. The width of the wire is determined by cutting it with a small negative voltage (Fig. 19). Given the speed of the AFM tip and the profile of the conductance of the wire as a function of time during the cutting we can estimate the width of the nanowire.

It is also possible to non-destructively image the wires by using piezoforce microscopy (PFM) [89] and microwave impedance microscopy (MIM) [90]. Conductive regions are found to be elongated in the z direction, out of plane, and PFM imaging of the nanowires determines a wire width of less than 30 nm. Wire widths measured by MIM are found to be on the order of 150-250 nm, however it should be noted that measurements are limited by the spacial resolution of the technique.

After the devices were written they begin to decay if left in ambient conditions. This can be seen as a reduction of the conductance over time of the devices. There are several ways to maintain the device after writing. It can be placed in a dry environment such as in vacuum, dry air, helium, or dry nitrogen [87]. Cooling the device will also preserve the conductance. After devices are written they are placed under vacuum and cooled down as quickly as possible. The
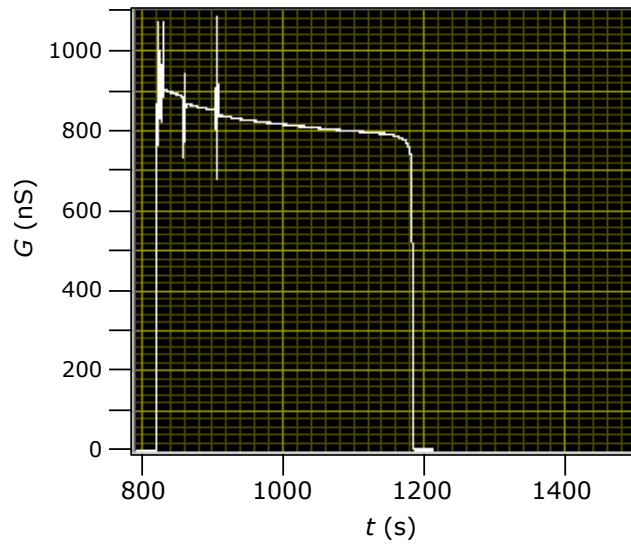
Figure 17: 2-terminal conductance during c-AFM writing test. As the nanowire is completed, at around 820 s, the conductance increases from 0 to ∼ 900 nS. The wire decays slightly until it is cut at around 1160 s. After the wire is cut the conductance is again 0 S. The cutting profile can be used to determine the width of the wire. The wire was cut at a speed of 10 nm/s, and is about 13 nm wide.
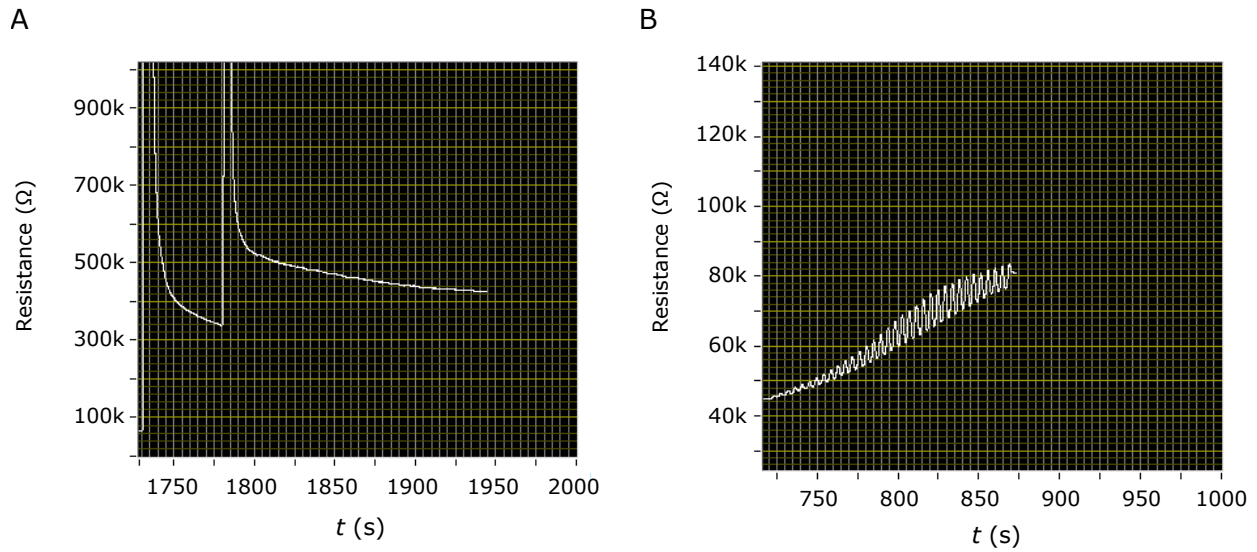
Figure 18: 4-terminal resistance during c-AFM writing. **(A)** Change in resistance when writing highly transparent tunnel barriers for an electron waveguide device. Two negative voltage pulses are applied to the AFM tip which causes the increase in the resistance. **(B)** 4-terminal resistance while writing a chiral 1D superlattice device. The voltage applied to the tip is varied sinusoidally while writing.
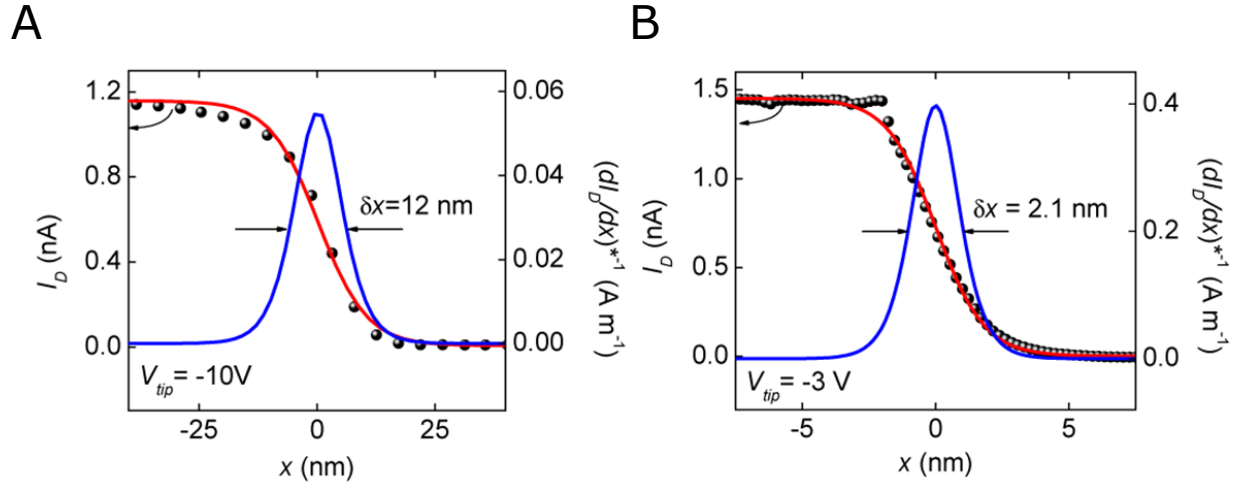
Figure 19: Nanowire width is determined by cutting the nanowire with a negatively-biased AFM tip. The profile of the drop in the current and the speed of the tip as the wire was cut, gives a measure of the width of the wire. **(A)** Nanowire written with a tip bias of $V_{tip} = 10$ V has a with of 12 nm. **(B)** Nanowire written with a tip bias of $V_{tip} = 3$ V has width of 2.1 nm.

lifetime of a device is generally 30 minutes to an hour if left in ambient conditions. The device has a higher chance of surviving at low temperature if it is cooled or pumped on as quickly as possible. Loading devices into dilutions refrigerators can take up to 30 minutes

2.4 TRANSPORT MEASUREMENTS

After devices are created at room temperature using c-AFM lithography they are transferred to cryostats to perform low temperature transport measurements at temperatures of $T = 25-50$ mK. More information about the cryostats used in these experiments can be found in Appendix A.

4-terminal zero bias transport measurements were performed using standard lockin amplifier techniques. A software-based Multichannel Lockin program [91] developed in-house was used to apply and measure the signals from the device. An AC voltage waveform was ap-

34
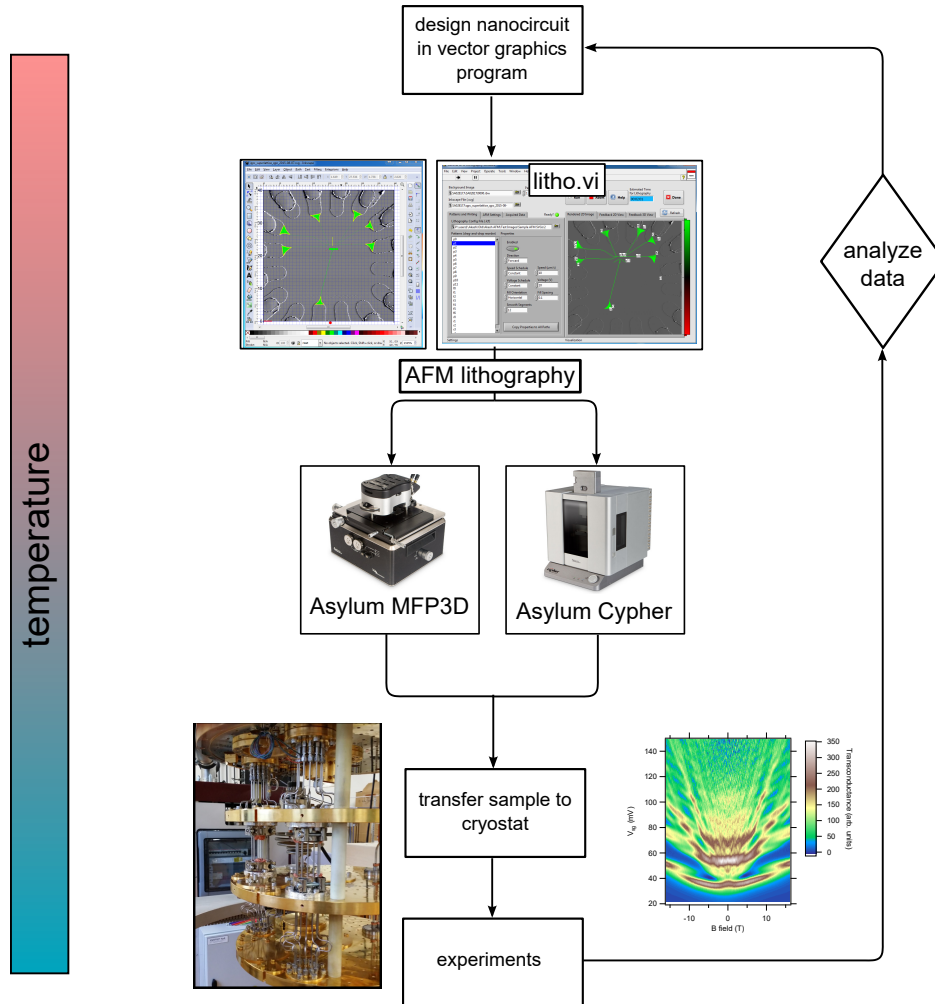
Figure 20: Flow chart showing the process for creating and measuring a typical device. Devices are created at room temperature using c-AFM lithography, then transferred to a cryostat where magnetotransport measurements are made. After analysis of the data a new design is created and the process can be repeated.

plied to the sample with a typical amplitude of 100 μV at frequencies of around 13 Hz. The software performs the lockin demodulation of all measured signals (current and voltage) at the applied source frequency. By measuring the current and the differential voltage across the device, we are able to determine the 4-terminal differential zero bias conductance of the experimental devices. More details about the hardware used in the experiments can be found in Appendix A.

Zero-bias measurements were generally made while sweeping the side gate voltage and the magnetic field. Typically the side gate was swept repeatedly and as rapidly as possible while the magnetic field was slowly varied. Side gate sweeps take on the order of several minutes while the magnetic field sweep takes several hours.

Direct current (dc) measurements, also measured using the Multichannel Lockin, were used to determine the finite-bias characteristics of the devices. Here a larger bias, typically 1-5 mV, was applied to the sample at a very low frequency, 0.2-1 Hz. This was used to measure the current-voltage (I-V) characteristics of the devices. This is a slower type of measurement than the zero-bias lockin measurements and was usually taken at a fixed magnetic field value while the side gate voltage was varied for each I-V curve.

Typical measurement hardware used is shown in Fig. 21. Pictured from top to bottom is the matrix breakout box, differential amplifiers, and a chassis with data acquisition cards (DAQ). The matrix breakout box connects each electrode of the sample to the measurement hardware through a 1 GHz low pass filter. Next are Krohn-Hite model 7008 differential amplifiers. The amplifiers have an input impedance of 1 GΩ and 400 Hz low pass filters. Each sample electrode is connected to the positive side of a differential amplifier. The negative side of the amplifier is connected to the analog output of a DAQ card. For voltage measurements the negative side of the amplifier is grounded. Differential measurements are made by mathematically subtracting the voltages measured at each electrode. For current measurements the negative side of the amplifier is connected to the positive side through a shunt resistor, usually 50 kΩ. The outputs of the differential amplifiers are connected to the inputs of the DAQ cards. The Multichannel Lockin controls voltages to each of the analog outputs and measures signals at the analog inputs. Any side gates are connected to analog outputs through a large resistor (10 MΩ) to limit the amount of current going to the sample. Typical side gate voltages are hun-

dreds of mV. The back of the sample is also connected to an analog voltage source through a 1 GΩ resistor. The backgate voltage is used to globally gate the sample, and is typically tens of V.
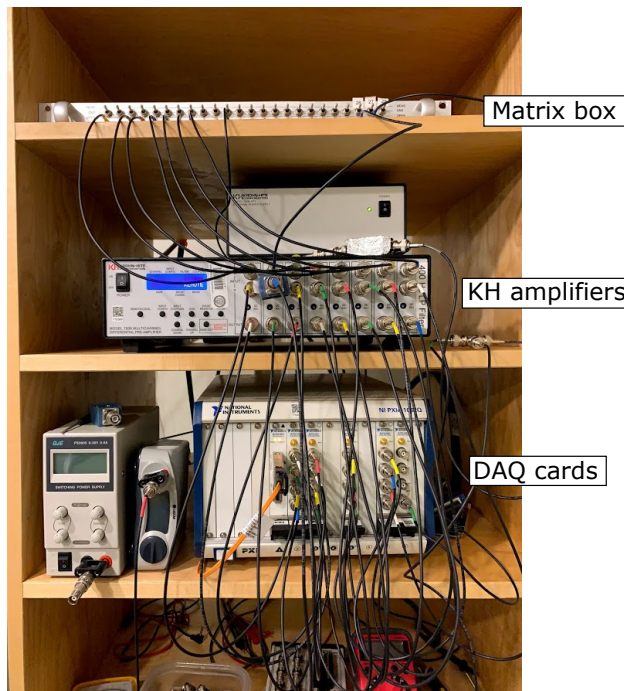
Figure 21: Picture of the measurement hardware for the Leiden MNK system. Top: matrix breakout box which connects the sample to the measurement hardware. Next: Krohn-Hite model 7008 differential amplifiers. Each sample electrode is connected to the positive side of a differential amplifier. For voltage measurements the negative side of the amplifier is grounded. For current measurements the negative side of the amplifier is connected to the positive side of the amplifier through a 50 kΩ shunt resistor. Current is sourced by applying a voltage to the negative side of the amplifier. Next: PXI chassis with 24-bit DAQ cards. The output of the differential amplifiers are connected to the inputs of the DAQ cards. The DAQ cards are controlled by the Multichannel Lockin software.

3.0 Quantized ballistic transport of electrons and electron pairs in LaAlO$_3$/SrTiO$_3$ nanowires

This chapter will discuss experiments which study the magnetotransport of electron waveguide devices created at the LaAlO$_3$/SrTiO$_3$ interface using c-AFM lithography. These electron waveguides provide new insight into the electronic structure of the LaAlO$_3$/SrTiO$_3$ interface and, more fundamentally, provide a platform for studying strongly interacting systems in one-dimension.[1]

3.1 INTRODUCTION

SrTiO$_3$-based heterointerfaces support quasi-two-dimensional (2D) electron systems that are analogous to III-IV semiconductor heterostructures, but also possess superconducting, magnetic, spintronic, ferroelectric, and ferroelastic degrees of freedom. Despite these rich properties, the relatively low mobilities of 2D complex-oxide interfaces appear to preclude ballistic transport in one-dimension (1D). We show that the 2D LaAlO$_3$/SrTiO$_3$ interface can support quantized ballistic transport of electrons and (nonsuperconducting) electron pairs within quasi-1D structures that are created using a conductive atomic-force microscope (c-AFM) lithography technique. The nature of transport ranges from single-mode (1D) to three-dimensional (3D), depending on the applied magnetic field and gate voltage. Quantization of the lowest e^2/h plateau indicates a ballistic mean-free path of $l_{\mathrm{MF}} \sim 20$ µm, more than 2 orders of magnitude larger than for 2D LaAlO$_3$/SrTiO$_3$ heterostructures. Nonsuperconducting electron pairs are found to be stable in magnetic fields as high as $B = 11$ T and propagate ballistically with conductance quantized at $2e^2/h$. Theories of 1D transport of interacting electron systems depend crucially on the sign of the electron-electron interaction, which may help explain the highly ballistic transport behavior. The 1D geometry yields new insights into the electronic structure of the LaAlO$_3$/SrTiO$_3$ system and offers a new platform for the study

---

[1]This chapter is published in a different form in Ref. [83].

of strongly interacting 1D electronic systems.

3.2   TRANSPORT IN 1D SYSTEMS

Dimensionality has a profound effect on electron transport. When electrons are confined in two dimensions (2D), new phases such as the integer [92] and fractional [93] quantum Hall effect emerge. Electrons confined in one dimension (1D) lose nearly all of their recognizable features [94, 95]. For example, the electron spin and charge can separate and move independently of one another [96], and the charge itself can fractionalize [97]. However, in 1D the conductance remains quantized in units of e^2/h [98]. The edges of 2D quantum Hall systems form nearly ideal 1D channels, where magnetic confinement gaps out the 2D bulk and protects electrons from backscattering. The chiral edge transport of the quantum Hall phase is fundamentally different from transport in 1D nanostructures where electrons are electrostatically confined to a narrow channel. Quasi-1D transport was first reported in narrow constrictions, also known as "quantum point contacts" [78, 79]. The conductance through these narrow channels is given by the number of allowed transverse modes, which is tunable by an external gate. The confined regions are generally short, of the order 100-200 nm, with a channel length set by the distance between the top gate electrodes and the buried high-mobility layer. There have been various attempts to engineer more extended 1D quantum wires using other growth techniques and different materials. For example, cleaved-edge overgrown III-V quantum wires exhibit quantized transport [99]. Other 1D systems include carbon nanotubes [100], graphene nanoribbons [101], and compound semiconductor nanowires [99, 102]. In all of these systems, electron transport is sensitive to minute amounts of disorder. For example, when 2D semiconductor heterostructures are patterned into 1D channels, the mobility drops significantly [103]. Theoretically, this sensitivity to disorder can be understood within the framework of Tomonaga-Luttinger liquid theory, which predicts that repulsive interactions promote full backscattering from even a single weak impurity [104, 105]. Conversely, attractive interactions are predicted to strongly suppress impurity scattering [105, 106].

Oxide heterostructures have added new richness to the field of quantum transport in

the past decade. For example ZnO/(Mn,Zn)O heterostructures have achieved sufficiently high mobility to reveal fractional quantum Hall states [107], which has revealed new even-denominator states not visible in III-V hosts [108]. LaAlO$_3$/SrTiO$_3$ heterostructures [34] exhibit a wide range of behavior including gate-tunable conducting [54], superconducting [55], fer-romagnetic [109], and spin-orbit coupled [47, 48] phases. As interesting and rich as its palette of rich phases may be, the 2D electron mobility is still low ($\mu_H \sim 10^3$ cm^2/(V s)) compared with high-mobility GaAs/AlGaAs heterointerfaces ($\mu_H \sim 10^7$ cm^2/(V s)). However, despite the modest mobility of the LaAlO$_3$/SrTiO$_3$ 2D interface, there is an increasing body of evidence suggesting that 1D geometries are able to support ballistic transport [110, 111, 82, 112].

3.2.1 Electron waveguide devices

The expected properties of an ideal few-mode (few subband) electron waveguide are il-lustrated in Fig. 22. The conductance of the waveguide depends on the number of acces-sible quantum channels (shown in Fig. 22D,E as energy shifted parabolic bands), which is controlled by the applied side-gate voltage V_{sg}. Fig. 22B,D depicts a state in which a single spin-resolved subband is occupied. As the chemical potential μ is increased, more subbands in the waveguide become occupied. Fig. 22C,E depicts a state in which $N = 3$ subbands con-tribute to transport. Each spin-resolved subband contributes e^2/h to the total conductance (Fig. 22F). The energy at which μ crosses a new subband (at $k_x = 0$) can generally shift in an applied magnetic field due to Zeeman and orbital effects. When lateral and vertical confine-ment energies are comparable, a more complex subband structure can emerge, as illustrated in Fig. 22G.

3.3 ELECTRON WAVEGUIDES AT THE LaAlO$_3$/SrTiO$_3$ INTERFACE

LaAlO$_3$/SrTiO$_3$ samples are grown by pulsed laser deposition (PLD) under conditions that are described in detail in Ref. [113] and in Chapter 2. The electron waveguides are created using a c-AFM lithography technique [4, 86]. Positive voltages applied between the c-AFM

tip and the $LaAlO_3/SrTiO_3$ interface locally produce conductive regions at the $LaAlO_3/SrTiO_3$ interface (illustrated in Fig. 22), while negative voltages locally restore the insulating phase. The mechanism for writing (erasing) is attributed to $LaAlO_3$ surface protonation (deprotonation) [87, 88]. The protonated $LaAlO_3$ surface in critical-thickness (3.4 u.c.) $LaAlO_3/SrTiO_3$ heterostructures creates an attractive confining potential that defines the nanowire. Because the protons are physically separated from the conducting region by a highly insulating $LaAlO_3$ barrier, this nanofabrication method can be viewed as analogous to the "modulation doping" technique [114] commonly used in III-V semiconductor heterostructures. The separation of dopants from the conducting region minimizes scattering from imperfections. A key difference from III-V nanostructures is the relative proximity between the dopant layer and conducting channel, here only 1.2 nm. Typical nanowire widths at room temperature are $w \sim 10$ nm, as measured by local erasure experiments [4].

3.3.1 Device fabrication

We fabricate $LaAlO_3/SrTiO_3$ electron waveguides using c-AFM lithography [4, 86], as shown in Fig. 22 (also see Chapter 2). The wires are written at a tip voltage $V_{\text{tip}} = 15$ V, except the waveguide, which is created by a two-step voltage sequence. First, we move the AFM tip with $V_{\text{tip}} = 8$ V across the $LaAlO_3$ surface to create the main channel. Next, we repeat the same tip path with a small base voltage ($V_{\text{tip}} = 1$ V) and apply two negative voltage pulses ($V_{\text{tip}} = 7.5$ V) to create the barriers. The barrier height is determined by the amplitude and duration of the negative pulses. The waveguide geometry consists of a nanowire channel of total length L_C, surrounded by two narrow, highly transparent barriers (width $L_B \sim 5-20$ nm) separated by a distance $L_S \sim 10-1000$ nm.

3.3.2 Magnetotransport data

The experimentally measured conductance of $LaAlO_3/SrTiO_3$ waveguides is shown in Fig. 23A-D. We focus on two distinct devices, device W1 ($L_C = 500$ nm, $L_S = 50$ nm, $L_B = 20$ nm) and device W2 ($L_C = 1.8$ μm, $L_S = 1$ μm, $L_B = 20$ nm). Fig. 23A,C shows the zero-bias conductance $G = dI/dV$ as a function of side-gate voltage V_{sg} (or chemical potential μ) for a
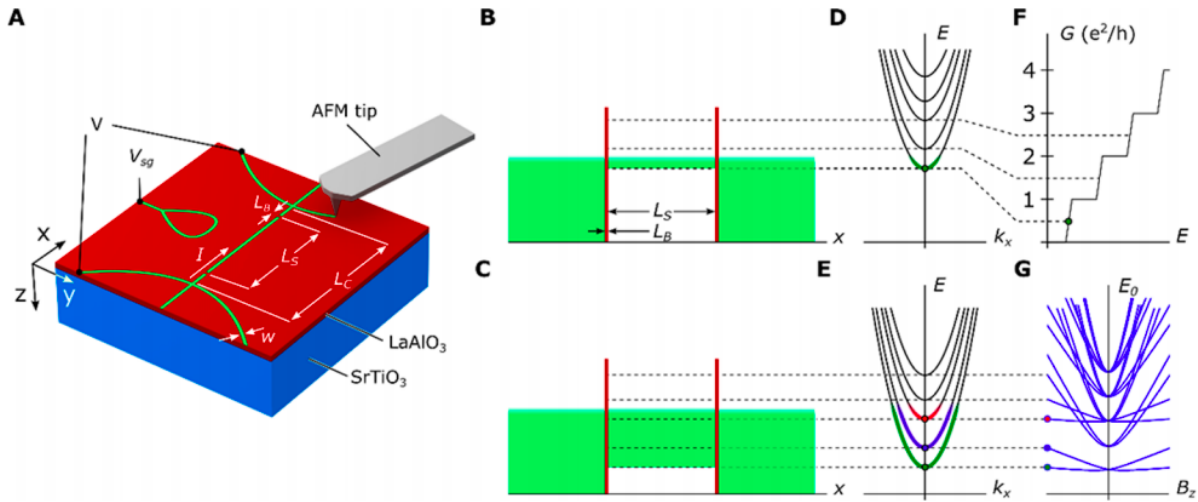
Figure 22: Electron waveguide device schematic and energy diagrams. **(A)** Schematic of an electron waveguide device at the LaAlO$_3$/SrTiO$_3$ interface. The green lines indicate where the positively biased c-AFM tip is moved on the LaAlO$_3$ surface to control the conductivity of the interface. Two barriers L_B are formed by applying negative voltage pulses to the AFM tip which retracing the device. **(B,C)** Energy diagrams of the waveguide for two different values of chemical potential, which is controlled by the side gate voltage V_{sg}. For (B) only a single subband is occupied, whereas for (C) three subbands are occupied. **(D,E)** Energy subbands corresponding to (B,C), colored bands indicate occupied states. **(F)** Zero-bias conductance as a function of energy (chemical potential) showing quantization at integer multiples of e^2/h for each occupied subband. **(G)** Waveguide subband structure (with both lateral and vertical confinement) as a function of out of plane magnetic field (which couples to the electrons via both Zeeman and orbital effects) and chemical potential.

sequence of magnetic fields between $B = 0$ and 9 T. Analysis of the nonequilibrium conductance, described later in this chapter, enables the lever-arm ratio $\alpha \equiv d\mu/dV_{sg}$ and g-factor $g \equiv \mu_B^{-1} d\mu/dB$, where μ_B is the Bohr magneton for the two devices W1 (W2), to be determined: $\alpha_{W1\,(W2)} = 4.5 \pm 0.2\,(9.9 \pm 1.7)\,\mu eV/mV$ and $g_{W1\,(W2)} = 0.62 \pm 0.03\,(0.61 \pm 0.04)$. For Device W1 (Fig. 23A), clear conductance steps of $G = 2e^2/h$ are visible for magnetic fields above ~ 1 T. These steps split into e^2/h steps up to $N = 6$ at fields above ~ 3 T. These electron waveguides exhibit no valley degeneracies and can be tuned to the lowest spin-polarized conduction plateau ($G = e^2/h$) with no signatures of substructure or "0.7 anomalies" [115]. When only a single barrier is present, no conduction quantization is observed (see discussion later in this chapter and Fig. 32B). When no barriers are present the overall conductance is very large and cannot be tuned to an insulating phase while maintaining the conductance of the voltage leads (Fig. 32A).

We attribute the observed conduction plateaus to Landauer quantization [98] for which the total conductance depends on the number of available quantum channels (subbands). The subband structure of these $LaAlO_3/SrTiO_3$ electron waveguides is clearly revealed by examining the transconductance $dG/d\mu$ as a function of μ and external magnetic field B (Fig. 23B,D). The transconductance peaks (bright areas) mark the boundaries where new subbands become available (as illustrated in Fig. 22G). The subbands are separated by regions (dark areas) where the conductance is highly quantized ($dG/d\mu \to 0$). At low magnetic fields (and low μ), the subbands scale roughly as B^2 and become more linear at larger magnetic fields. A pattern of subbands repeats at least twice, spaced by approximately 500 μeV. The transconductance of the two devices W1 ($L_S = 50$ nm) and W2 ($L_S = 1$ μm) are remarkably similar, despite the large difference in channel length and the fact that the lever arm for the two devices differs by a factor of 2.

3.3.3 Ballistic scattering length

Whereas the lowest $N = 1$ state remains highly quantized for both devices (see Fig. 23), the plateaus do not fully reach the integer values for higher N for device W2. The relationship between two length scales, the length scale of the device and the elastic scattering length

44
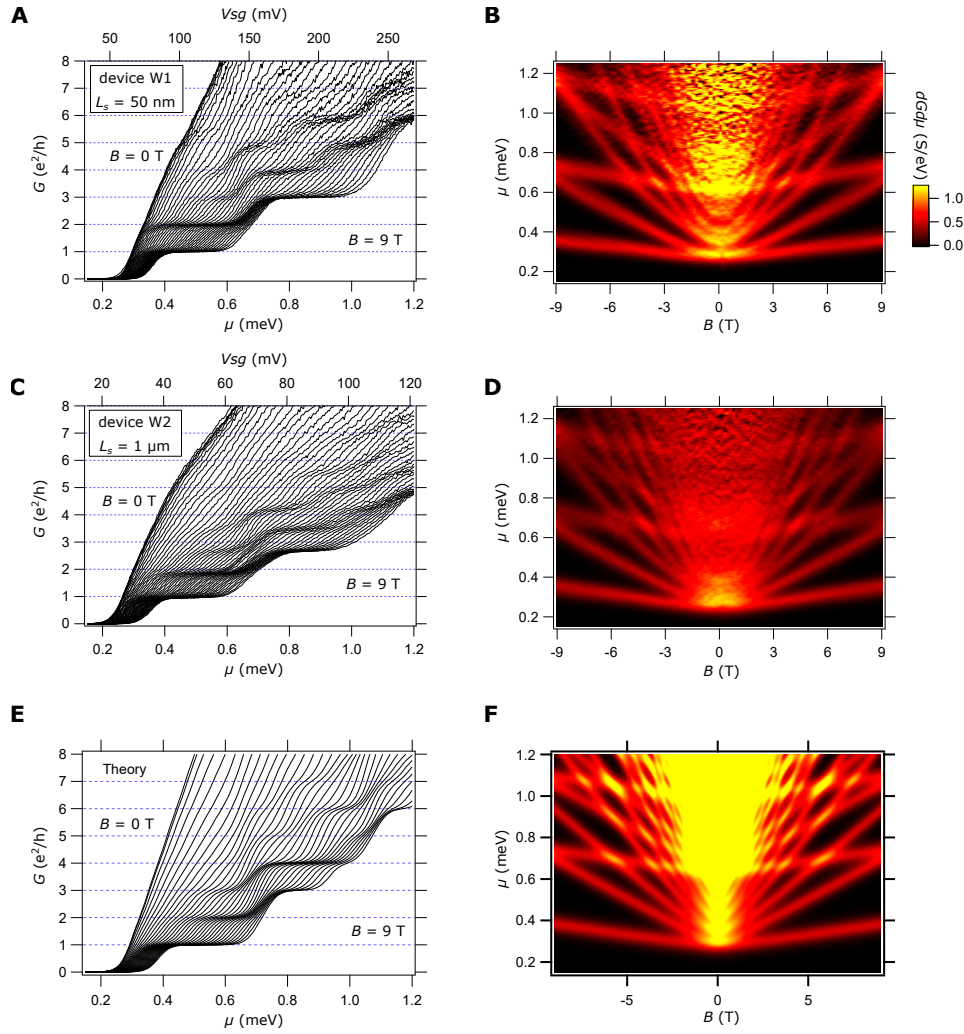
Figure 23: Magnetotransport data for devices W1, W2, and single-particle model. **(A,C)** Zero-bias conductance for device W1 ($L_B = 20$ nm, $L_C = 500$ nm, $L_S = 50$ nm) and device W2 ($L_B = 20$ nm, $L_C = 1800$ nm, $L_S = 1000$ nm) as a function of chemical potential μ and magnetic field B in the range $0-9$ T at $T = 50$ mK. **(B,D)** Transconductance $dG/d\mu$ shown as a function of μ and B for device W1 (panel B) and device W2 (panel D). Each bright band marks the crossing of a subband, dark regions indicate plateaus in the conductance. The subband structure between the two devices is remarkably similar. **(E)**. Theoretical zero-bias conductance curves modeling device W1, for a non-interacting channel. **(F)**. Corresponding transconductance for theoretical curves in panel E. Transitions have been broadened by a 65 μeV wide Lorentzian.
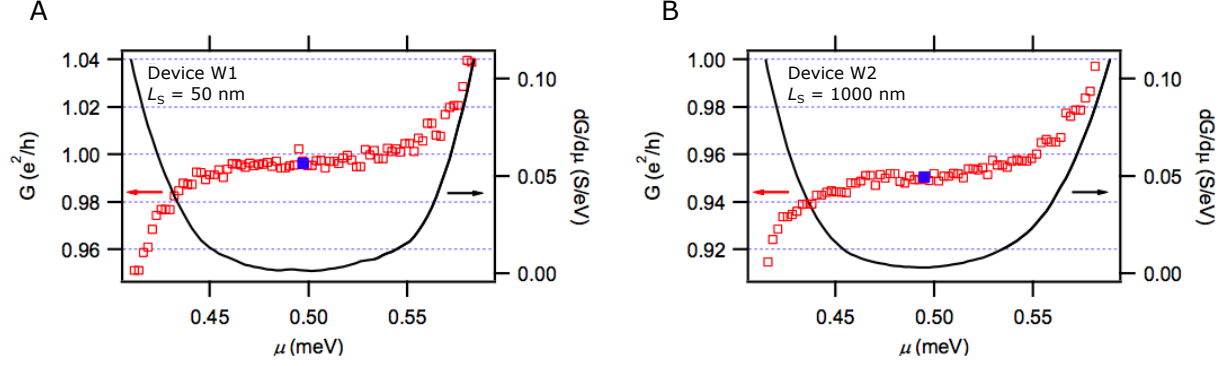
Figure 24: Estimation of ballistic scattering length and quantization of the 1 e^2/h plateau. First conductance plateau (red squares) and transconductance (black line) for device W1 **(A)** and device W2 **(B)**. Fits of the conductance at the transconductance minimum are used to calculate scattering lengths.

(which is typically much shorter than the inelastic scattering length in quantum devices), determines whether transport is ballistic. The conductance of these modes are not exactly e^2/h, however, in part because they are not topologically protected edge modes, nor are they quantum Hall edge states [116]. In electron waveguides at the $LaAlO_3/SrTiO_3$ interface, the elastic scattering length can be estimated by assuming an exponential decay of the conductance $G = G_0\exp(L/L_0)$, where L_0 is the scattering length and L is the length of the device. The location of the minimum in the transconductance is used to find the value of the plateaus, as seen in Fig. 24. The scattering lengths greatly exceed the length of the devices (Table 1), implying that the transport is fully ballistic. The error estimate for Device W1 is limited by the short length of the channel. For Device W2, the channel length is long enough to yield (with 10% accuracy) a measure of the scattering length $L_0 = 22$ μm which is surprising given how low the 2D mobility is for $LaAlO_3/SrTiO_3$. We also note that systematic errors (e.g., reflections of incident electrons at one or both of the barriers) are only expected to increase these estimates.

Table 1: Measured scattering lengths and standard errors for waveguide devices W1 and W2, based on deviations from precise quantization $N\, e^2/h$ of conductance.

Device	Plateau N	L (nm)	ΔL (nm)	G (e^2/h)	ΔG (e^2/h)	L_0 (µm)	δL_0 (µm)
A	1	50	10	0.995	0.004	10	8
A	2	50	10	0.964	0.12	2	14
B	1	1000	10	0.955	0.003	21.7	1.4
B	2	1000	10	0.899	0.076	7.8	4.6

3.4 WAVEGUIDE MODELS

3.4.1 Non-interacting waveguide model

A waveguide model of noninteracting electrons in a 3D waveguide captures many of the features in the transconductance spectra shown in Fig. 23A-D. The waveguide's confining potential is translationally invariant along the propagation direction (x) and convex along the two transverse directions (lateral y and vertical z). The measured carrier density in conductive nanostructures created by c-AFM lithography is typically $0.5 - 1.0 \times 10^{13}$ cm^{-2} [117]. At these carrier densities only the titanium d_{xy} band, which is lower in energy than the d_{xz} and d_{yz} bands at the LaAlO$_3$/SrTiO$_3$ interface, is expected to by occupied. We describe the potential of the lateral confinement as $U_y = \frac{1}{2} m_y^* \omega_y^2 y^2$, where $m_x^* = m_y^*$ is the effective mass in the $x - y$ plane and $\omega_y = \hbar/m_y^* l_y^2$ is the confinement frequency with l_y being the characteristic width of the waveguide. In the vertical direction, the confinement at the interface is modeled by a half-parabolic potential, $U_z = \frac{1}{2} m_z^* \omega_z^2 z^2$ for $z > 0$ and $U_z = \infty$ for $z \leq 0$, where m_z^* is the effective mass of the d_{xy} band in the z direction, $\omega_z = \hbar/m_z^* l_z^2$ is the confinement frequency, and l_z is the penetration depth into the SrTiO$_3$. Within this single-particle picture, the full Hamiltonian can be written in the Landau gauge as

$$H = \frac{(p_x - eBy)^2}{2m_x^*} + \frac{p_y^2}{2m_y^*} + \frac{p_z^2}{2m_z^*} + \frac{m_y^* \omega_y^2}{2} y^2 + \frac{m_z^* \omega_z^2}{2} z^2 - g\frac{\mu_B}{2} B\sigma_z, \tag{3.1}$$

where σ_z is the Pauli matrix. This Hamiltonian is solved to yield energy eigenstates $|n_y, n_z, s\rangle \otimes |k_x\rangle$ with corresponding energy

$$E_{m,n,s,k_x} = \hbar\Omega\left(n_y + \frac{1}{2}\right) + \hbar\omega_z\left((2n_z + 1) + \frac{1}{2}\right) - g\mu_B Bs + \frac{\hbar^2 k_x^2}{2m_x^*}\left(1 - \frac{\omega_c^2}{\Omega^2}\right), \qquad (3.2)$$

where p_i, $i = x, y, z$ are momentum operators, $\omega_c = eB/m_y^*$ is the cyclotron frequency, $\Omega = \sqrt{\omega_y^2 + \omega_c^2}$ is the effective frequency of the waveguide and the magnetic field, n_y (n_z) enumerates the lateral (vertical) states, and $s = \pm 1/2$ is the spin quantum number. Distinct spin-resolved subbands [118] are associated with the discrete quantum numbers $|n_y, n_z, s\rangle$. Fig. 25A plots the eigenenergies for parameters that have been adjusted to resemble the experimentally measured transconductance (Fig. 23D). These values are also used to compute the expected conductance and transconductance versus chemical potential (Fig. 23E,F). The corresponding wavefunctions $\Phi_{n_y, n_z, k, s}(y, z)$ (Fig. 25C) are,

$$\begin{aligned}
\Phi_{n_y, n_z, k, s}(y, z) &\equiv \langle y, z, s; k | n_y, n_z, s\rangle \otimes |k_x\rangle \\
&= N_{n_y, n_z, k} e^{-(m_y^*\Omega/2\hbar)(y - (\hbar\omega_c/m_y^*\Omega)k)^2} \\
&\quad \times H_n\left(\sqrt{\frac{m_y^*\Omega}{\hbar}}\left(y - \frac{\hbar\omega_c^2}{m_y^*\Omega}k\right)\right) e^{-(m_z^*\omega_z/2\hbar)z^2} H_{2m+1}\left(\sqrt{\frac{m_z^*\omega_z}{\hbar}}z\right),
\end{aligned} \qquad (3.3)$$

where $H_n(x)$ are the Hermite polynomials. The wave functions are displaced laterally by the magnetic field by an amount that depends quadratically on the kinetic energy (Fig. 25B). The set of parameters for device W1 (W2), $l_y = 26\,(27)$ nm, $l_z = 8.1\,(7.9)$ nm, $m_x^* = m_y^* = 1.9\,(1.8)\,m_e$, and $m_z^* = 6.5\,(6.4)\,m_e$ is obtained by maximizing agreement with a tight-binding model that includes spin-orbit interactions (see Supplemental information of published paper [83]). At low magnetic fields, the energy scales quadratically with magnetic field, as it is dominated by the geometrical confinement contribution; at higher magnetic fields, the confinement from the cyclotron orbits dominates, producing a linear scaling. The crossover occurs near $\omega_B = \frac{eB}{m_y^*} \sim \omega_y$.

The single-particle model captures the overall subband structure but there are several deviations in the experimental results. For example the lowest two subband minima for device W1 and W2 merge not at zero magnetic field, but at a critical field $B_P \approx 1$ T. In other devices,
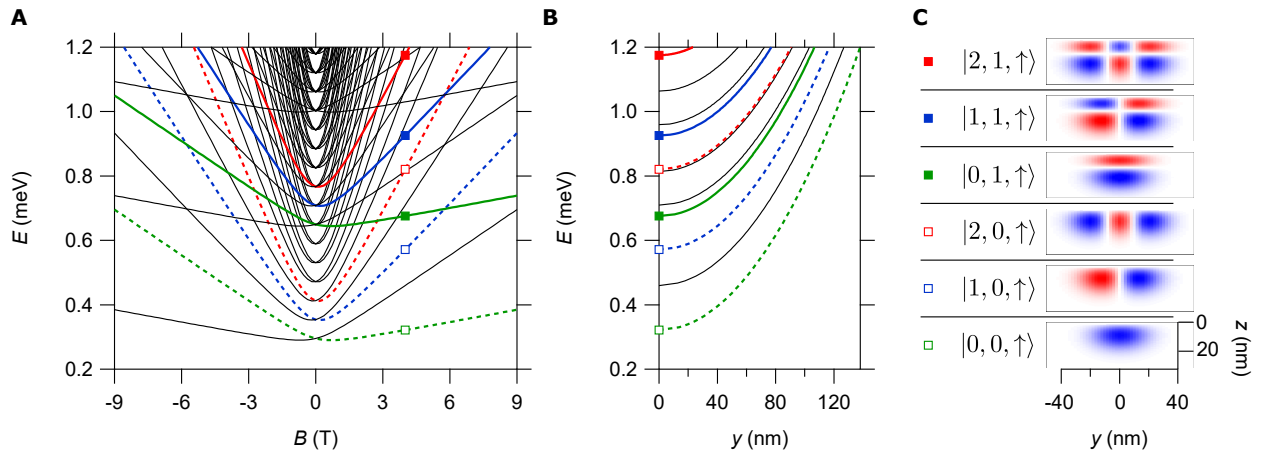
Figure 25: Single-particle model energy diagrams and wavefunctions. **(A)** Eigenenergies for a quantum wire for the Hamiltonian described in Eq. 3.1 are plotted as a function of magnetic field B. Selected spin-up states are highlighted in color. **(B)** Magnetically induced displacement of these states along the y-direction as a function of eigenstate energy for $B = 4$ T. **(C)** Six corresponding wave functions, labeled by $|n_y, n_z, S\rangle$, at $k_x = 0$ and $B = 4$ T. Red and blue colors indicate opposite sign of the wave function.
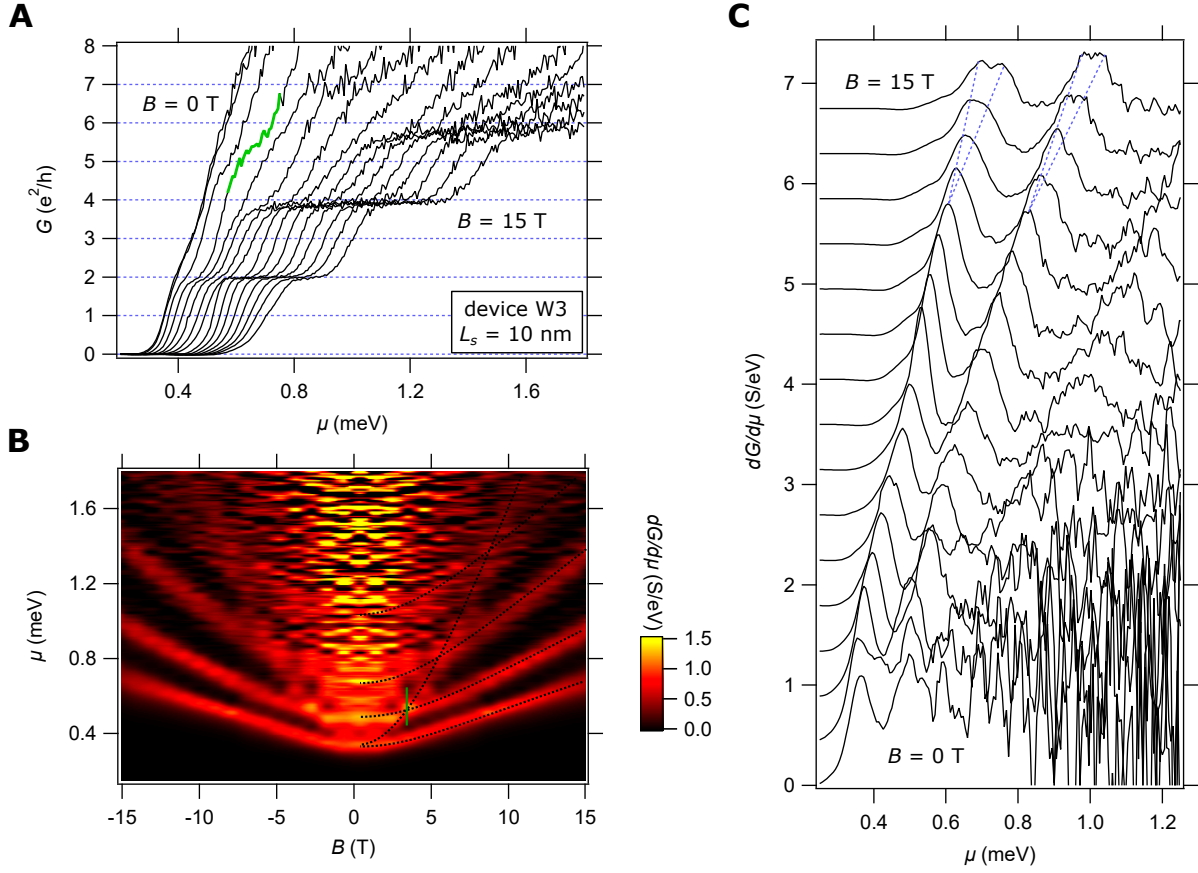
Figure 26: Magnetotransport data for high pairing field device W3. **(A)** Conductance of device W3 ($L_B = 5$ nm, $L_C = 350$ nm, $L_S = 10$ nm) versus chemical potential for magnetic fields ranging from 0 to 15 T at $T = 50$ mK. This device shows strong electron pairing and associated $2e^2/h$ conductance steps. **(B)** Transconductance plot shows three strongly pairing states and a superimposed state with higher curvature associated with a conductance of e^2/h. The value of the later state can be seen at $B = 3$ T in the conductance curve in panel (A) (highlighted in green) where it combines with the second strongly paired subband into a plateau near $5e^2/h$. **(C)** Linecuts of transconductance plotted at magnetic fields from 0 to 15 T in 1 T steps. The $2e^2/h$ peaks split above a pairing field $B_P \approx 11$ T, as indicated by the dashed lines.

this phenomena is even more pronounced. Device W3, written on a different sample, exhibits highly quantized conduction but with a subband structure that differs qualitatively from devices W1 and W2. There are three pairs of subbands that generate $2e^2/h$ steps (Fig. 26A). These states separate at a critical field $B_P \approx 11$ T (Fig. 26C, dashed lines). Superimposed over these pairs is a separate subband (with higher curvature) that contributes e^2/h to the conductance (Fig. 26B). At $B \approx 3$ T, two paired subbands are superimposed with the unpaired subband, leading to a plateau near $5e^2/h$ (highlighted in green).

3.4.2 Interacting model

We investigated other single-particle models (e.g. band anisotropy, spin-orbit interactions), but none were able to reproduce this observed locking phenomena. This locking behavior can be accounted for by introducing attractive electron-electron interactions within the waveguide. Within this framework, locking of subbands is associated with a phase in which electrons are paired but not superconducting[119]. The effects of these interactions become apparent in the transconductance data in the vicinity of subband crossing points (both at zero magnetic field and at finite field). We also observe extended regions of $2\ e^2/h$ conductance steps which we associate with a transition from a vacuum phase directly into a paired phase. That is, when a pair of subbands with opposite spin ($|1,0,\uparrow\rangle$, $|0,1,\downarrow\rangle$) intersect at a finite magnetic field they are found to pair reentrantly before separating again (Fig. 27). This observation is consistent with previous studies of one-dimensional fermions with attractive interactions using both the Bethe ansatz approach [120] (for the case of equal masses) and numerical approaches [121, 122] (for the case of unequal masses). Here, we present a simple self-consistent Hartree-Bogoliubov model of crossing subbands that is both consistent with the more refined approaches and highlights the relevant physics without adding complication. We start with the two-band, one-dimensional Hubbard model

$$H = -\sum_{i,\alpha} t_a (c_{\alpha,i}^\dagger c_{\alpha,i+1} + h.c.) + \sum_{i,\alpha} V_\alpha(V_{sg}, B) n_{\alpha,i} + U \sum_i n_{1,i} n_{2,i} \qquad (3.4)$$

where i is the site index, α is the subband index, $V_\alpha(V_{sg}, B)$ describes the electrochemical potential as a function of the side gate voltage and the magnetic field, and $U < 0$ models the

51

electron-electron attraction. At the mean-field level, this model is described by the single-particle Hamiltonian

$$\begin{pmatrix} \xi_{1,k} + \Sigma_1 & 0 & 0 & \Delta_{\mathrm{rp}} \\ 0 & -(\xi_{1,k} + \Sigma_1) & \Delta_{\mathrm{rp}} & 0 \\ 0 & \Delta_{\mathrm{rp}} & \xi_{2,k} + \Sigma_2 & 0 \\ \Delta_{\mathrm{rp}} & 0 & 0 & -(\xi_{2,k} + \Sigma_2) \end{pmatrix} \Psi_{\beta,k} = E_{\beta,k} \Psi_{\beta,k} \qquad (3.5)$$

where we use the $c_{1,k}, c_{1,k}^\dagger, c_{2,-k}, c_{2,-k}^\dagger$ basis, $1, 2$ are the subband labels, $\Psi_{\beta,k}$ and $E_{\beta,k}$ are the quasi-particle wave functions and eigenenergies, $\xi_{\alpha,k}(\mu, B)$ corresponds to the noninteracting energy of an electron in the transverse subband α with momentum k along the wire, in a magnetic field B, and a chemical potential μ (that is tuned by V_{sg}). Σ_1, Σ_2, and Δ_{rp} are the mean fields that must be found self-consistently. Σ_α represents the Hartree shifts due to the electrons in the opposite subband $\bar{\alpha}$

$$\Sigma_\alpha = U_{\mathrm{H}} \int \frac{\mathrm{d}k}{2\pi} \langle c_{\bar{\alpha},k}^\dagger c_{\bar{\alpha},k} \rangle \qquad (3.6)$$

and Δ_{rp} represents the re-entrant pairing field

$$\Delta_{\mathrm{rp}} = U_{\mathrm{B}} \int \frac{\mathrm{d}k}{2\pi} \langle c_{2,-k} c_{1,k} \rangle. \qquad (3.7)$$

For correctness, we have made the minimal assumption that the interactions are momentum-independent (i.e., local in real space) when writing the mean fields. We caution that a nonzero value of Δ should not be interpreted as a signature of superconductivity but only as a signature of pair formation as we are working in one-dimension. Finally, when computing the matrix elements, we must keep in mind that the basis we are using is twice as big as the physical basis and consequently, quasi-particle wave functions come in conjugate pairs. Only one member of the pair should be used (e.g., the one that has the positive eigenvalue and thus corresponds to the quasi-particle creation operator).

We solve the Hartree-Bogoliubov model self-consistently to obtain a phase diagram near the crossing point of the $|0, 1, \downarrow\rangle$ and $|1, 0, \uparrow\rangle$ subbands (Fig. 27C. The locations of the non-interacting subbands are plotted with dashed lines. By turning on the attractive intersubband interaction, the Hartree shift tends to pull down the upper subband away from the crossing

point, and pairing prevails closer to the crossing point which results int eh merger of the two subbands into a single paired subband. Following the Maslov and Stone theorem, the conductance in the paired (spin-gapped) phase must be $2\, e^2/h$ (ref [123]). We expect that these qualitative predictions are generic for systems with attractive interband interactions and not particularly sensitive to the assumptions that we have made, that is, using the Hartree-Bogoliubov model with local interactions.

Using the phase diagram in Fig. 27C, we use a phenomenological model containing the phase boundaries to describe interband re-entrant pairing. The basic scenario is when two subbands $E_1 = (k_1 B + b_1)$ and $E_2 = (k_2 B + b_2)$ with opposite spins are tuned closely in energy, they combine as an electron pair, which breaks when the energies are tuned further away. These two subbands would simply cross (orange dashed lines) if there were no electron-electron interaction. In the presence of the attractive pairing interaction, the higher energy subband undergoes an energy shift of $-2\delta_{1(2)}$ so that it can be written as $E'_{1(2)} = k_{1(2)}B + b_{1(2)} - 2\delta_{1(2)}$. A middle section representing the paired phase emerges. The re-entrant pairing energy Δ_{rp} can then be extracted: $\Delta_{\mathrm{rp}} = \delta_1 + \delta_2$. We are now able to use this model to extract these parameters from the experimental data using the fittings shown in Fig. 27C. This process then gives a pairing field range 3.3 T $< B <$ 3.5 T and a pairing energy $\Delta_{\mathrm{rp}} = 13$ μeV for subbands $|1, 0, \uparrow\rangle$ and $|0, 1, \downarrow\rangle$ in device W1 (see Table 2 for the full fitting parameters). More details about the model can be found in the supporting information of the published manuscript [83].

3.5 CONCLUSION

The observed conductance plateaus are not consistent with a quantum Hall state. The integer quantum Hall effect is defined by an insulating 2D bulk with chiral edge states that are responsible for the quantized conductance. By contrast, $LaAlO_3/SrTiO_3$-based electron waveguides lack the insulating bulk region that prevents backscattering. That is to say, the magnetic length ($l_B \sim 15$ nm for $B = 3$ T) and the confinement length ($l_y = 26$ (27) nm for device W1 (W2)) are comparable and no well-defined bulk region is present.

The 3D structure of the electron waveguides is also inconsistent with quantum Hall
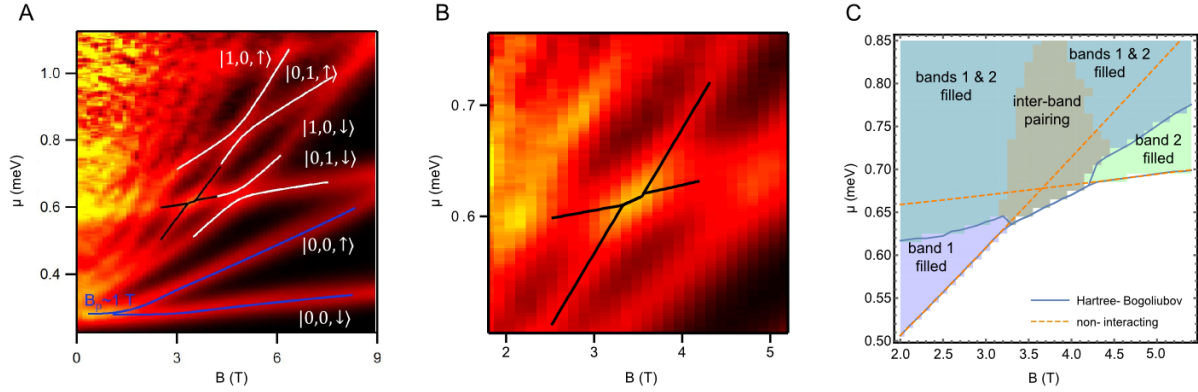
Figure 27: Electron-electron interactions in electron waveguides. **(A)** Electron pairing (blue lines), avoided crossing (white lines), and re-entrant pairing (black lines) fittings of transconductance for device W1. **(B)** Detailed view of re-entrant pairing data in (A). Here the black lines show the fitting of re-entrant pairing between subband $|0, 1, \downarrow\rangle$ and $|1, 0, \uparrow\rangle$ with $\Delta_{\mathrm{rp}} = 13\,\mu$eV. The white lines are the fitting to the avoided crossing between subband $|0, 1, \downarrow\rangle$ and $|1, 0, \downarrow\rangle$ with $\Delta_{1,2} = 16\,\mu$eV. **(C)** Phase diagram of the Hartree-Bogoliubov model in the $\mu - B$ plane and near the crossing point of $|0, 1, \downarrow\rangle$ and $|1, 0, \uparrow\rangle$. We used the band parameters for device W1 and set the attractive interaction constants to be $U_H = U_B = 100\,\mu$eV to produce this diagram.

Table 2: Re-entrant pairing fitting parameters for electron waveguide devices W1 and W2.

device	subbands	k (μeV/T)	b (μeV)	Δ_{rp} (μeV)
device W1	$|1, 0, \uparrow\rangle$	133	168	13
	$|0, 1, \downarrow\rangle$	15	566	
device W2	$|1, 0, \uparrow\rangle$	130	120	10
	$|0, 1, \downarrow\rangle$	14	585	

physics. The cross-section of our waveguides is ellipsoidal with an aspect ratio of 0.5 (vertical/lateral, see Fig. 25C, which is well within the 3D regime). This regime is not expected to support stable quantum Hall bilayer states as multiple vertical subbands are occupied. For example in Fig. 27A the $|0,0,\uparrow\rangle$ and $|0,1,\downarrow\rangle$ subbands would be unstable and therefore not quantized in a quantum Hall regime, according to Ref. [124]. The fact that quantized transport is observed provides further proof that this form of transport is not described by quantum Hall effects.

Finally, the lack of observable quantization at low fields is a consequence of the close spacing of lateral subband modes. The single-particle theory, illustrated in Fig. 23E,F, shows that broadening of the subband transitions prevents the individual subbands from becoming resolvable at low magnetic fields; however, they become visible as soon as the magnetic dispersion can clearly separate them in energy. In other waveguides with larger subband spacing, conductance quantization is observable at small magnetic fields (Fig. 31).

The observation of quantized conduction in the paired regime ($G = 2e^2/h$ and $|B| < B_P$) signifies that these (non single-particle) states propagate ballistically, forming an extended state in which electron pairs are bound together while the center-of-mass coordinate remains delocalized. Conduction quantization with steps of $2e^2/h$, rather than $(2e)^2/h$, is consistent with the notion that dissipation takes place not within the channel itself but in the leads, and that electron pairs unbind before they dissipate energy [125, 126]. This interpretation is also consistent with the theorem of Maslov and Stone, who argued that the conductance of a Luttinger liquid is determined by the properties of the leads [123]. Specifically, the charge conductance of the channel remains $2e^2/h$ when a spin (i.e., pairing) gap is opened in the channel.

Previous reports of electron pairing in confined 1D structures [119] revealed a range of pairing fields that is consistent with the variation observed in these electron waveguides. For devices W1 and W2, $B_P \sim 1$ T is relatively low compared to $B_P \sim 11$ T in device W3. Fig. 31 shows additional variation of B_P in two other devices. No specific dependence of B_P on device length can be inferred. Clearly, there are hidden variables that regulate the strength of electron pairing that have yet to be revealed experimentally.

The experiments described here show that electron wave-guides provide remarkably detailed insight into the local electronic structure of these oxide interfaces. The level of repro-

ducibility and reconfigurability illustrated by these experiments represents a significant advance in control over electronic transport in a solid-state environment. Correlated electron waveguides offer unique opportunities to investigate the rich physics that is predicted for 1D quantum systems [95]. For example, the number of quantum channels can be tuned to the lowest spin-polarized state (with $G = e^2/h$), forming an ideal spin-polarized Luttinger liquid. The ballistic nature of the transport in 1D is highly surprising, but may be related to the existence of strong electron-electron interactions, which are known to suppress impurity scattering [105, 106]. These 1D channels form a convenient and reproducible starting point for emulating a wider class of 1D quantum systems or for creating quantum channels that can be utilized in a quantum computing or quantum simulation platform.

3.6 ADDITIONAL INFORMATION

3.6.1 Finite bias spectroscopy

Finite-bias spectroscopy is performed through current-voltage (I-V) measurements as a function of V_{sg} and B to gain more information about the electron waveguides. As shown in Fig. 28A, a large finite bias ($V_{sd} \geq V_{sd}^*$) can unevenly populate subbands occupied by oppositely travelling electrons, which gives rise to the so-called half plateaus [127, 128]. Fig. 28B is the finite-bias transconductance plot of device W1 at $B = 7$ T. The dark regions marked by the numbers are conductance plateaus, where conductance is quantized. The 0.5 e^2/h and 1.5 e^2/h plateaus can be clearly seen in the conductance plot at $V_{sd} = V_{sd}^* = 200\,\mu$V (Fig. 28C). The observation of these half plateaus in indicative of very clean transport of the electron waveguide devices, since back scattering is more likely to occur when unoccupied subbands become available at finite biases.

Finite-bias spectroscopy is used to extract the lever-arm α, which converts gate voltage V_{sg} to chemical potential μ. As illustrated in Fig. 28B, the bright crossing at $V_{sd}^* = 200\,\mu$V and $V_{sg} = 80$ mV marks the transition from one subband to another due to the bias. At this condition, the energy gain induced by the bias V_{sd}^* should be equal to the subband spacing
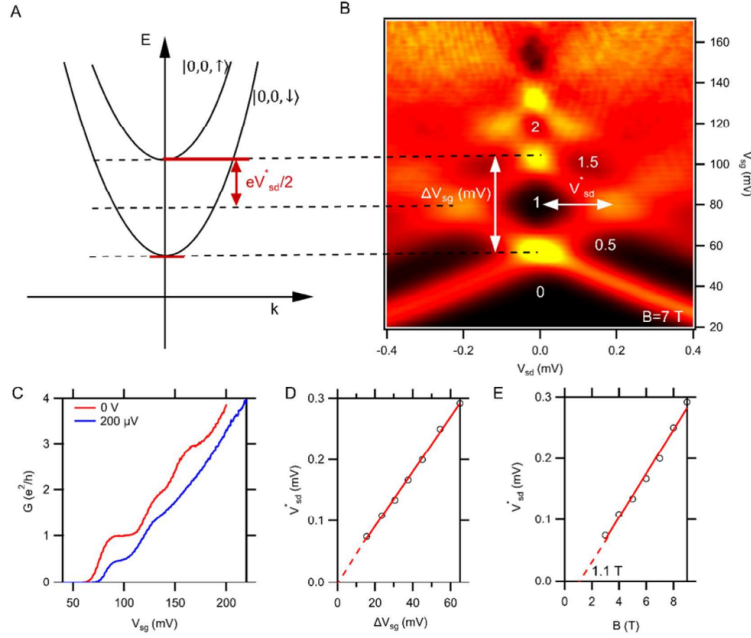
Figure 28: Electron waveguide finite bias analysis. **(A)** Illustration of electron occupation sub-bands $|0,0,\downarrow\rangle$ and $|0,0,\uparrow\rangle$ at a finite bias V_{sd} in a magnetic field $B = 7$ T. The application of V_{sd} alters the chemical potentials of the source μ_s and drain μ_d to $E_F \pm e\,V_{sd}/2$. The energy difference $\mu_d - \mu_s = e\,V_{sd}^*$ (as indicated by the two red lines) equals the spacing between the two subbands. When $V_{sd} < V_{sd}^*$, electrons travelling in opposite directions occupy the same subband, $|0,0,\downarrow\rangle$ with conductance quantized at e^2/h. When V_{sd} reaches $|V_{sd}^*|$ ($-|V_{sd}^*|$), subband $|0,0,\uparrow\rangle$ becomes available for electrons transmitting from the drain (source) and gives rise a half plateau conductance $1.5e^2/h$. **(B)** Transconductance map of device W1 as a function of V_{sd} and V_{sg} at $B = 7$ T. Each light band marks the transition between conductance plateaus, the values of which are labeled in white. According to (A), the conversion factor α can be extracted through the relation $V_{sd} = \alpha \Delta V_{sg}$. **(C)** Conductance G vs V_{sg} curves for zero bias ($V_{sd} = 0$ V) and finite bais ($V_{sd} = V_{sd}^* = 200\,\mu$V) at $B = 7$ T. Half plateaus are visible at finite bias (blue curve). **(D)**. V_{sd} vs ΔV_{sg} at magnetic fields from 3 T to 9 T in 1 T steps. The linear relationship and negligible intercept establishes $V_{sd}^* = \alpha \Delta V_{sg}$ with $\alpha = 4.5\,\mu$eV/mV. **(E)** V_{sd} vs B for Device W1 shows the Zeeman splitting between subbands $|0,0,\downarrow\rangle$ and $|0,0,\uparrow\rangle$. The g factor can be extracted, and is found to be $g = 0.6$. This plot also illustrates the pairing field, that the subbands only split above a critical magnetic field $B_P = 1.1$ T, the intercept on the B axis.

57

marked by $\alpha \Delta V_{\text{sg}}$ at zero bias, namely $e\,V_{sd} = \alpha \Delta V_{sg}$. Then, $\alpha = e\,V_{sd}^*/\Delta V_{\text{sg}}$ can be precisely extracted by the slope of the V_{sd}^* - V_{sg} plot at different magnetic fields (Fig. 28D). For device W1, α_{W1} is found to be 4.5 μeV/mV, and the fitted linear curve passes across zero as supposed. Similarly, $\alpha_{\text{W2}} = 9.9$ μeV/mV can be extracted for device W2, suggesting a stronger coupling of side age to the waveguide due to the larger size.

The Zeeman splitting between two spin-resolved subbands $|0,0,\uparrow\rangle$ and $|0,0,\downarrow\rangle$ can be used to extract the electron g factor. Fig. 28D shows the energy splitting ($e\,V_{sd}^*$) between these two subbands at various magnetic fields, where spin degeneracy is moved. The g factor is given by $g = \frac{e\,V_{sd}^*}{\mu_B B'}$, where μ_B is the Bohr magneton. The extracted g factors for device W1 and W2 are the same (within measurement error): $g_{W1\,(W2)} = 0.6$.

3.6.2 Temperature dependence

The temperature dependence of the conductance plateaus at $B = 9$ T is shown in Fig. 29. Temperatures were varied from $T = 100$ mK to 500 mK. As the temperature increases the plateaus become less distinct because of thermal averaging.

3.6.3 Impact of side gate location

The physical location of the side gates for $LaAlO_3/SrTiO_3$ nanostructures affect the overall lever arm (α) but, somewhat surprisingly, impacts the electronic structure within the conducting regions only negligibly. To illustrate, we show transport results for a single-electron transistor device with multiple side gates (Fig. 30A). The differential conductance is shown as a function of four-terminal source-drain voltage V_{sd} and either of the side gates located near the barriers V_{sg1} or V_{sg2}. The results for both gates are nearly identical (Fig. 30C,D), which shows that the electric fields are effectively screened and the main result of gating is to change the chemical potential uniformly within the conducting wire segment. The near equivalence of both gates is also shown by plotting the conductance at zero bias versus the two gates (Fig. 30B). Differences between the two gates are negligibly small, apart from the factor-of-two difference in lever arms. This insensitivity is likely related to the very large dielectric constant of $SrTiO_3$ at low temperatures.
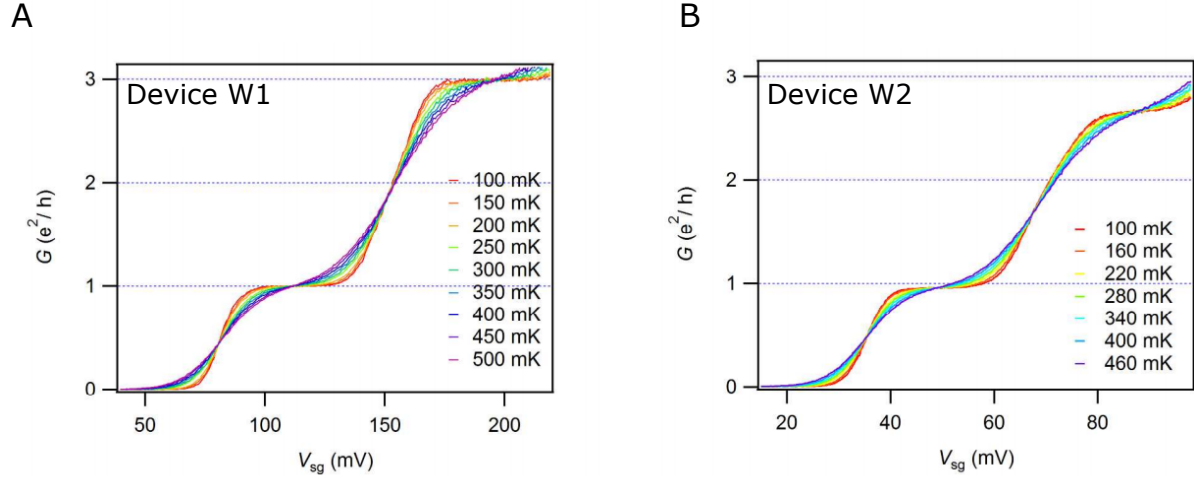
Figure 29: Temperature dependence of conductance plateaus. Conductance as a function of side gate voltage at different temperatures for Device W1 **(A)** and Device W2 **(B)** in an applied magnetic field of 9 T.

3.6.4 Additional electron waveguide devices

Transport for several additional electron waveguide devices W4 and W5 is shown in Fig. 31. Device W4 has a pairing field of $B_P \sim 2.5$ T and device W5 has a pairing field larger than $B_P > 9$ T, the largest applied field.

3.6.5 Zero-barrier, single-barrier, and double-barrier geometry

In GaAs-based heterostructure devices, the number of transverse channels that are transmitted through a quantum point contact (QPC) is typically controlled by a spit top gate. Varying the potential on the split gate controls the effective width of the conducting region. In the case of $LaAlO_3/SrTiO_3$ similar behavior may be expected in the case where the side gate is used to control a QPC created by a single weak barrier. In Fig. 32B, we show the results of varying the side gate V_{sg} for a device with a single barrier in the channel. At all values of magnetic field, there is no clear quantization of the conductance. This is consistent with the single particle

59
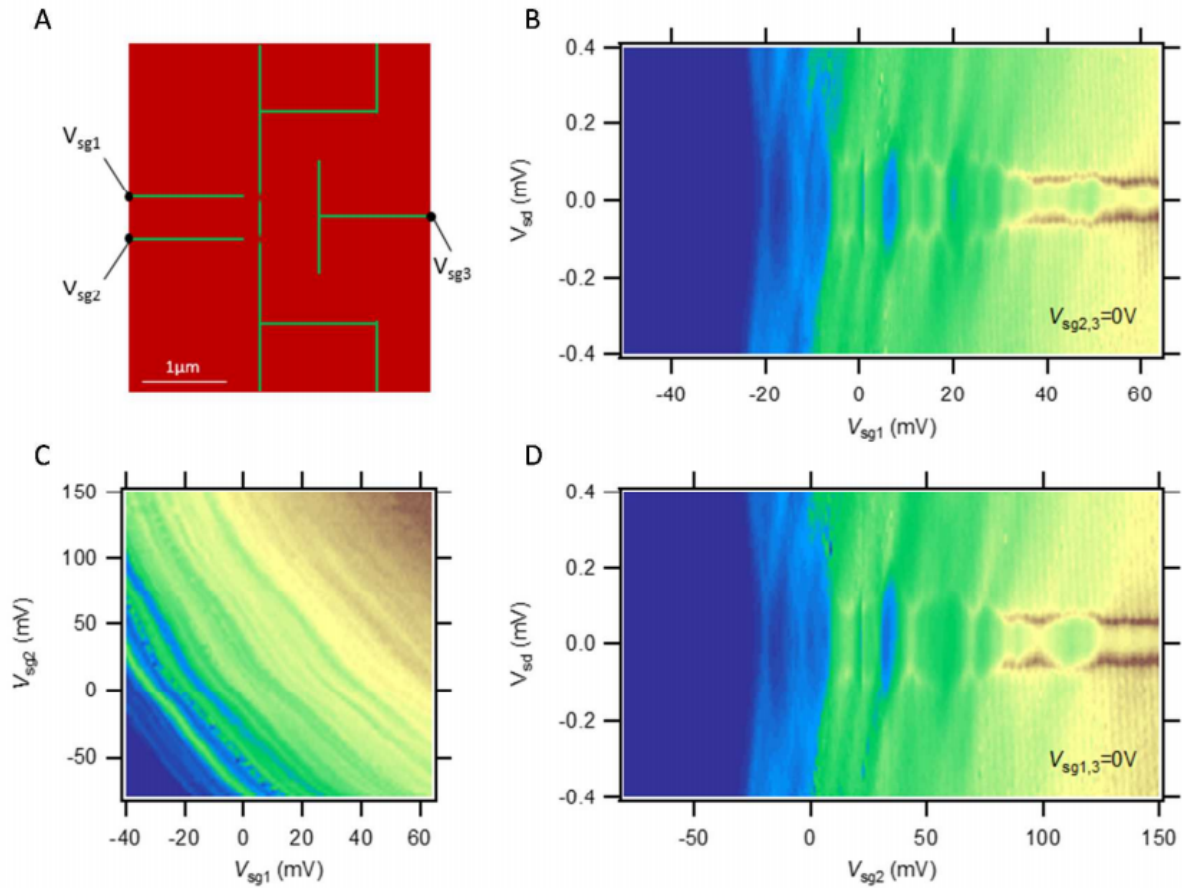
Figure 30: Dependence of transport on gate location. **(A)** Device schematic for a three gate device. **(B)** Conductance as a function of V_{sg1} and V_{sg2} (with V_{sg3} floating). While the lever arm of the gates differ, the conductance features are similar for both gates. **(C)**,**(D)** Conductance as a function of source-drain bias across the device V_{sd}, and V_{sg1} (C) and V_{sg2} (D) with the other gates fixed at 0 V. The transport through the device does not depend on the location of the gate.
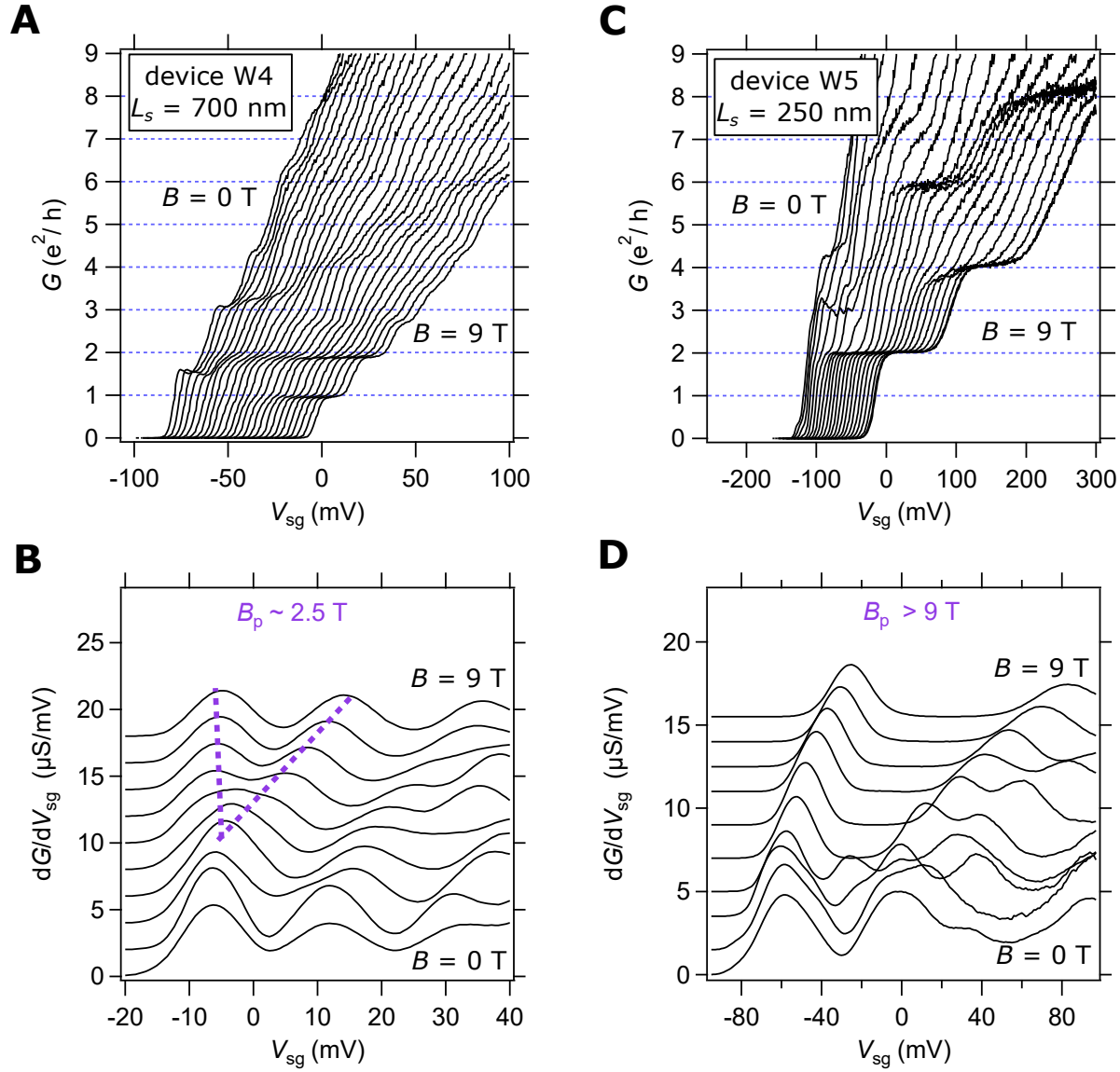
Figure 31: Data for additional electron waveguide devices showing different pairing fields. (**A** and **C**) Zero bias conductance G as a function of side gate V_{sg} and B for device W4 ($L_B = 20$ nm, $L_C = 1500$ nm, and $L_S = 700$ nm) and device W5 ($L_B = 20$ nm, $L_C = 500$ nm, and $L_S = 250$ nm) fabricated on different canvases. Curves are offset for clarity. (**B** and **D**) Corresponding transconductance dG/dV_{sg} plots to reveal the pairing field B_P at which subbands $|0,0,\downarrow\rangle$ and $|0,0,\uparrow\rangle$ start to split. B_P values are high for device W4 (~ 2.5 T) and device W5 (> 9 T) compared to device W1 and W2.
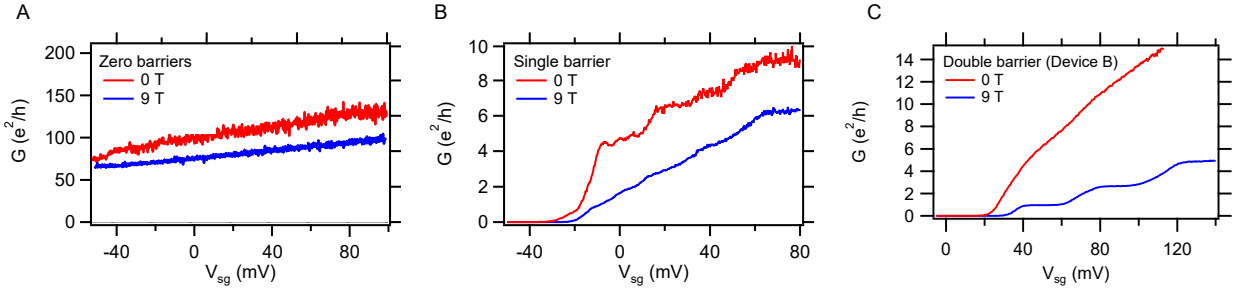
Figure 32: Conductance data for devices with different numbers of barriers. Conductance at 0 T and 9 T for devices with zero **(A)**, one **(B)**, and two **(C)** barriers. Devices with zero barriers and one barrier do not exhibit well quantized conductance plateaus. Devices with no barriers are not able to be effectively tuned with the side gate because they are not isolated from the leads, and are not able to be tuned to an insulating state with the side gate.

theory shown in Fig. 23 and 25 which holds the width of the conducting channel, l_y, fixed as V_{sg} is varied. Thus we conclude that, as in the case for the quantum dot geometries used in Ref [118], varying V_{sg} controls the chemical potential of the region between the two barriers, as illustrated in Fig. 22. When no barriers are present (Fig. 32A) there is no observed quantization and the conductance in the nanowire is very large and cannot be tuned to an insulating state using the side gate.

4.0 Pascal conductance series in ballistic one-dimensional LaAlO$_3$/SrTiO$_3$ channels

In a subset of the electron waveguide devices, discussed in Chapter 3, we observed a new series of conductance plateaus, $G = (1, 3, 6, 10, ...)e^2/h$, reminiscent of the third diagonal of Pascal's triangle. This series of conductance steps arises from the locking together of the 1D subbands in increasing number, and the formation of bound states of $n = 2$, 3, 4, ... electrons in what we call a Pascal liquid phase.[1]

4.1 INTRODUCTION

The ability to create and investigate composite fermionic phases opens new avenues for the investigation of strongly correlated quantum matter. We report the experimental observation of a series of quantized conductance steps within strongly interacting electron waveguides formed at the LaAlO$_3$/SrTiO$_3$ interface. The waveguide conductance follows a characteristic sequence within Pascal's triangle: $(1, 3, 6, 10, 15, ...) \cdot e^2 h$, where e is the electron charge and h is the Planck constant. The robustness of these steps with respect to magnetic field and gate voltage indicate the formation of a new family of degenerate quantum liquids formed from bound states of $n = 2$, 3, 4, ... electrons. These experiments could provide solid-state analogues for a wide range of composite fermionic phases ranging from neutron stars to solid-state materials to quark-gluon plasmas.

This investigation of strongly fermionic systems and their resulting phases benefits from focusing on one-dimensional (1D) systems [130, 94, 95, 131]. By restricting the phase space for transport, correlations are significantly enhanced. A variety of techniques have been developed for understanding strongly-correlated 1D systems, ranging from the Bethe ansatz to density matrix renormalization group (DMRG) approaches [132]. Experimental investigations of degenerate, 1D gases of paired fermions have been explored in ultracold atom systems with attractive interactions [133]. In the solid state, attractive interactions have been engineered

---

[1]This chapter is published in a different form in Ref. [129].

in carbon nanotubes using a proximal excitonic pairing mechanism [134]. Electron pairing without superconductivity, indicating strong attractive interactions, has been reported in low-dimensional $SrTiO_3$ nanostructures [119, 83]. However, color superfluids [135] - bound states of three or more particles - have only been observed in few-body bosonic systems [136].

$SrTiO_3$-based electron waveguides can provide insight into strongly interacting fermionic systems. The total conductance through an electron waveguide is determined by the number of extended subbands (indexed by orbital, spin, and valley degrees of freedom) available at a given chemical potential μ [98, 76]. Each subband contributes one quantum of conductance e^2/h with transmission probability $T(\mu)$ to the total conductance $G = (e^2/h)\sum_i T(\mu)$ [75]. Quantized transport was first observed in III-V quantum point contacts [78, 79] and subsequently in 1D systems [99, 100, 102]. Quantized conduction within 1D electron waveguides was recently demonstrated within $LaAlO_3/SrTiO_3$ heterostructures [83], see Chapter 3. A unique aspect of this $SrTiO_3$-based system is the existence of tunable electron-electron interactions [137] that lead to pairing [119] and superconductivity [58].

4.2   RESULTS

4.2.1   Device fabrication

Here we investigate $LaAlO_3/SrTiO_3$-based 1D electron waveguides that are known to exhibit quantized ballistic transport as well as signatures of strong attractive electron-electron interactions and superconductivity. A thin film of $LaAlO_3/SrTiO_3$ (3.4 unit cells) is grown on TiO_2-terminated $SrTiO_3$ using pulsed laser deposition using growth conditions described in detail in Ref. [113], and in Chapter 2. Electrical contact is made to the interface in several locations that surround a given "canvas", typically a 30 μm by 30 μm area. An electron waveguide (Fig 33A) is created by first scanning a positively-biased ($V_{tip} \sim 10$ V) conductive atomic force microscope (c-AFM) tip in contact with the $LaAlO_3$ surface [4, 5]. This process locally protonates [87, 88] the top $LaAlO_3$ surface and accumulates conducting electrons in the $SrTiO_3$ region near the $LaAlO_3/SrTiO_3$ interface. To restore an insulating state, negative voltages are

64

applied to the tip, which locally de-protonates the LaAlO$_3$ surface. During a second pass of the tip along the channel, following the same path, two negative voltage pulses ($V_{\text{tip}} \sim -15$ V) are used to create two weakly insulating, $L_{\text{B}} \sim 20-30$ nm-long barriers, separated by a length $L_{\text{S}} \sim 50-1000$ nm. A side gate is written ~ 1 μm away from the electron waveguide. These devices are qualitatively the same as the electron waveguide devices discussed in Chapter 3. However, in over a dozen specific devices we observed different signatures of transport which will be discussed below. Parameters and properties for seven representative devices P1-P7 are given in Table 3.

4.2.2 Pascal series conductance plateaus

The conductance of these electron waveguides depends principally on the chemical potential μ and the applied magnetic field $\vec{B}$. The chemical potential is adjusted with a local side gate V_{sg}, and for most experiments described here the external magnetic field is oriented perpendicular to the LaAlO$_3$/SrTiO$_3$ interface: $\vec{B} = B_z\hat{z}$. Quantum-point contacts formed in semiconductor heterostructures [78, 79] exhibit conductance steps which typically follow a linear sequence: $2 \times (1, 2, 3, 4, ...)\cdot e^2/h$, where the factor of 2 reflects the spin degeneracy. In an applied magnetic field, the electronic states are Zeeman-split, and resolve into steps of $(1, 2, 3, 4, ...)\cdot e^2/h$. By contrast, here we find that for certain values of magnetic field, the conductance steps for LaAlO$_3$/SrTiO$_3$ electron waveguides follow the sequence $(1, 3, 6, 10, ...)\cdot e^2/h$, or $G_n = n(n+1)/2\cdot e^2/h$. As shown in Fig. 33B, this sequence of numbers is proportional to the third diagonal of Pascal's triangle (Fig. 33C, highlighted in red).

4.2.3 Transconductance data

In order to better understand the origin of this sequence, it is helpful to examine the transconductance $dG/d\mu$ and plot it as an intensity map as a function of B and μ. Transconductance maps for Devices P1-P6 are plotted in Fig. 34. A peak in the transconductance demarcates the chemical potential at which a new subband emerges; these chemical potentials occur at the minima of each subband, and as such we refer to them as subband bottoms (SBB). The peaks generally shift upward as the magnitude of the magnetic field is increased, some-
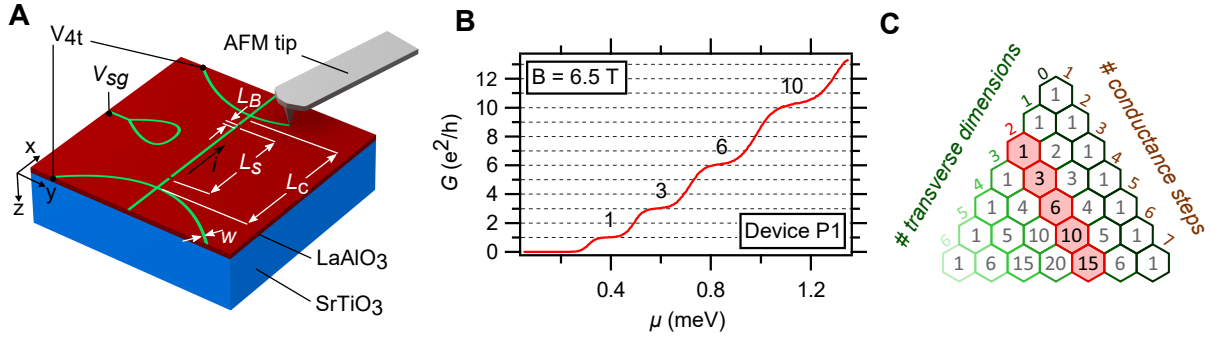
Figure 33: Pascal series of conductance steps in an electron waveguide. **(A)** Electron waveguide device schematic. Green lines indicate paths taken by AFM tip with a positive voltage applied, to create nanowires at the $LaAlO_3/SrTiO_3$ interface. The device consists of a main channel length L_C with highly transparent tunnel barriers, with width L_B, and separated by length L_S. Nanowire width w measured at room temperature is typically ~ 10 nm. **(B)** Conductance as a function of chemical potential for Device P1 at $T = 50$ mK and $B = 6.5$ B. Plateaus in conductance are observed at values of $G = (1,\ 3,\ 6,\ 10) \cdot e^2/h$. **(C)** Pascal triangle representation of observed conductance steps, represented in units of e^2/h. Highlighted row represents the sequence for an electron waveguide with two transverse degrees of freedom.

times bunching up and then again spreading apart. We observe many of the same features that were previously reported in 1D electron waveguides in LaAlO$_3$/SrTiO$_3$ [83] such as electron pairing and re-entrant pairing, which indicate the existence of electron-electron interactions. Near a special value of the magnetic field, locking of multiple subbands contribute to the total conductance as a function of chemical potential (see the labeled conductance plateaus in Fig 34A), which follows a Pascal series that is quantized in units of e^2/h.

4.3   DISCUSSION

Our approach to understanding the transport results described above begins with a single-particle description and incorporates interactions when the original description breaks down. Outside of the locked regions, the system is well described by a set of non-interacting channels, which places strong constraints on the theory of the locked regions. Any theory of the locked phases would need to both explain the locking of the transconductance peaks as well as quantized conductance steps away from the locked regime. Before settling on an attractive interaction interpretation of the locking phenomenon we considered a number of alternative mechanisms: spin-orbit, anharmonic confining potential, and impurity scattering but found that none of these resulted in the observed locking behavior. Within the single-particle description, we find that by fine-tuning the magnetic field and a single geometrical parameter of the waveguide, the ratio of vertical to lateral confinement strength, we can obtain the Pascal series of conductance plateaus. Next, we explore the addition of attractive electron-electron interactions to the model. The resulting calculations produce phases that are stable over a finite range of magnetic fields and geometrical parameters, thus lifting the requirement for fine-tuning that was imposed by the single-particle picture. In transconductance maps, the phases manifest themselves as the locking of peaks over a finite range of magnetic fields.

4.3.1   Single-particle model

The single-particle model used here is the same one discussed in Chapter 3, but is included here again for completeness. Our single-particle description excludes interactions but takes
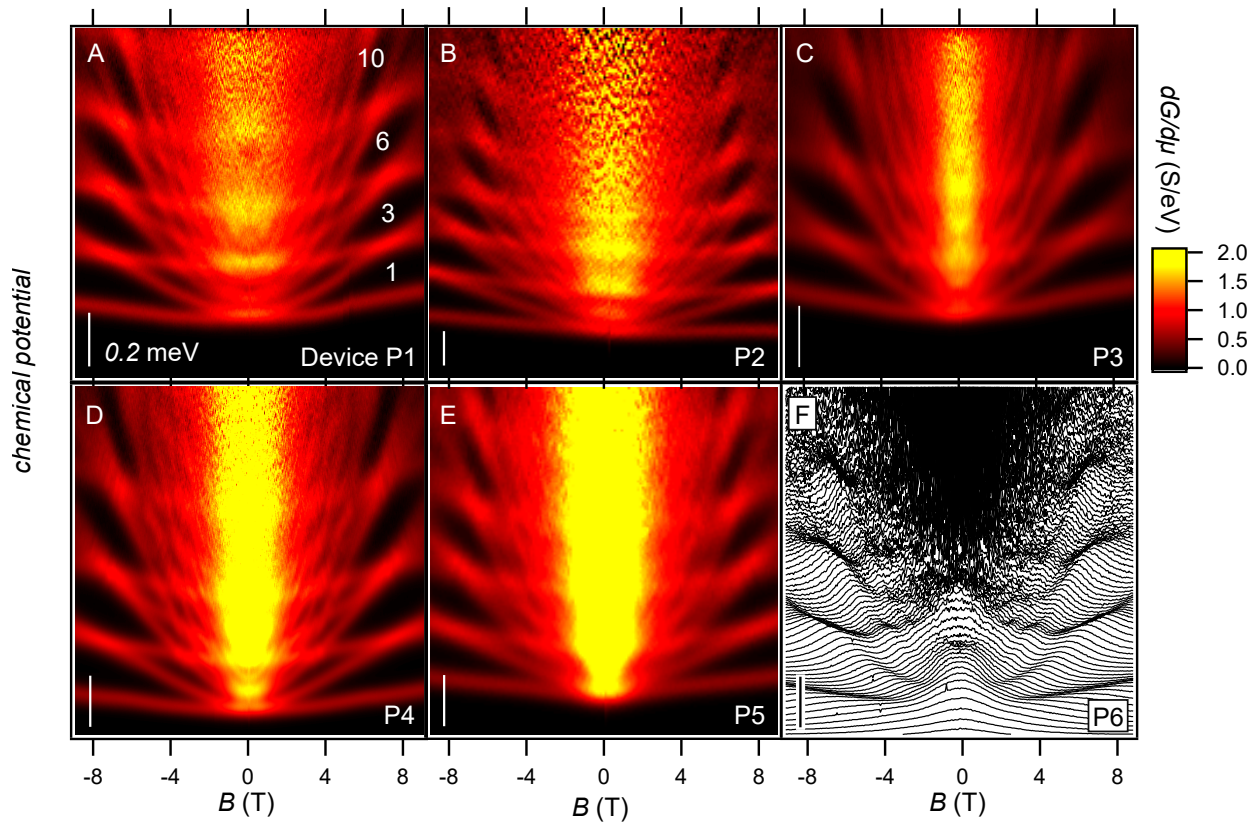
Figure 34: Transconductance maps of Pascal electron waveguide devices. Transconductance $dG/d\mu$ as a function of chemical potential μ and out of plane applied magnetic field B for representative Devices P1-P6. Bright regions indicate increasing conductance as new subbands become occupied, and dark regions indicate conductance plateaus where the conductance is flat. Conductance values for several plateaus are indicated in white in panel A, highlighting the Pascal series seen in all six devices shown here. Vertical scale bars in each panel represent 0.2 meV in chemical potential. The transconductance in Device P6 is displayed as a waterfall plot with vertical offsets given by the chemical potential at which the curve was acquired.

into account the geometry of the electron waveguide that produces the underlying subband structure. The four ingredients of the single-particle model are electrons confined in the (i) vertical and (ii) lateral directions by the waveguide and an external magnetic field that affects the electrons via the (iii) Zeeman and the (iv) orbital effect. *The intersection of more than two SBBs requires a special condition to be satisfied in the single particle model.* The degeneracy requirement for obtaining the Pascal series (i.e. the crossing of 1, 2, 3, 4, ... SBBs) is satisfied by a pair of ladders of equispaced levels. Indeed, a pair of ladders of equispaced levels is naturally produced by a waveguide with harmonic confinement in both vertical and lateral directions. In the presence of Zeeman interactions, the waveguide Hamiltonian can be written [83]

$$H = \frac{(p_x - e B_z y)^2}{2m_x^*} + \frac{p_y^2}{2m_y^*} + \frac{p_z^2}{2m_z^*} + \frac{m_y^* \omega_y^2}{2} y^2 + \frac{m_z^* \omega_z^2}{2} z^2 - g\mu_B B_z s, \tag{4.1}$$

where m_x^*, m_y^*, and m_z^* are the effective masses in the x, y, and z directions; ω_y and ω_z are frequencies associated with parabolic transverse confinement in the lateral (y) direction and half-parabolic confinement in the vertical ($z > 0$) direction, respectively; g is the Landé factor; μ_B is the Bohr magneton; and $s = \pm 1/2$ is the spin quantum number. Eigenenergies corresponding to the SBBs are given by

$$E_{n_z,n_y,s} = \hbar\Omega\left(n_y + \frac{1}{2}\right) + \hbar\omega_z\left((2n_z + 1) + \frac{1}{2}\right) - g\mu_B B_z s, \tag{4.2}$$

where the electron eigenstates $|n_z, n_y, s\rangle$ are indexed by the orbital quantum numbers n_z and n_y and spin quantum number s, $\Omega = \sqrt{\omega_y^2 + \omega_c^2}$ is the magnetic field-dependent frequency associated with parabolic confinement of the electron in the lateral direction (being made of the bare frequency ω_y and the cyclotron frequency $\omega_c = e B_z / \sqrt{m_x^* m_y^*}$). To obtain two equispaced ladders of states we use the states associated with Ω for the first ladder and the states associated with ω_z, split by the Zeeman splitting, for the second ladder. The Pascal series is produced by the "Pascal condition": $\Omega = 4\omega_z = 2g\mu_B B_z/\hbar$. This condition requires finetuning of the magnetic field B_z and the geometry of the waveguide (ω_y/ω_z). Meeting this condition results in crossings of increasing numbers of SBBs at a unique Pascal field B_{Pa}. By fitting the SBB energies given by Eq. 4.2 to experimental data, we are able to generate a peak structure (shown in Fig. 35A) that is in general agreement with and has the same sequence of

peak crossings as the experimentally observed transconductance. (Estimates for the single-particle model parameters are listed in Table 3.) By intentionally detuning the parameters away from the Pascal condition (e.g. Fig. 35B), the SBBs no longer intersect at a well-defined magnetic field. Fits of the single-particle model to experimental data for devices P1-P7 (Fig. 35C) show the expected correlation between ω_z and $\Omega(B_{\text{Pa}})$, but we do observe small deviations from the Pascal condition for all samples.

4.3.2 Experimental deviations from the single-particle model

The experimental data deviates from the single-particle model in several important ways. At low magnetic fields, the predicted linear Zeeman splitting of subbands is not obeyed; instead, the two lowest subbands ($|0, 0, \pm 1/2\rangle$) are paired below a critical magnetic field, B_{P} [83]. At higher magnetic fields, re-entrant pairing is observed as subbands intersect and lock together over a range of magnetic field values, near the Pascal field B_{Pa}. In our non-interacting model (Eq. 4.1), there is a unique Pascal field B_{Pa}; however, experimentally we find that the value of the Pascal field depends on the degeneracy n: $B_{\text{Pa}}^{(n+1)} < B_{\text{Pa}}^{(n)}$. This shift in B_{Pa} with the degeneracy may be due to an anharmonic component to the confinement. Adding an anharmonic term to the single-particle model produces similar shifts of B_{Pa} (see [129] SM for more details). The pairing field B_{P} and the Pascal field B_{Pa}^2 for devices P1-P7 are shown in Table 3. Devices with similar geometries display a variety of pairing fields and Pascal fields. This is not unexpected based on previous work [119] where the pairing field was found to vary significantly from device to device and can be as large as $B_{\text{P}} = 11$ T. The cause for the differing strength of the pairing field is unknown but likely plays a role in the differing strengths of the locking (re-entrant pairing) for the Pascal degeneracies in this work. Fits of the transconductance data were made (shown in white on Fig. 36A) for the $n = 2$ and $n = 3$ Pascal phases to determine if the states are, in fact, locking together over a finite range of magnetic fields. Details about the fitting procedure are described later in this chapter. As shown in Fig. 36B, the standard deviation for the fitted locations for the SBBs versus magnetic field for the first Pascal-liquid phase, $n = 2$, indicates a locking over a magnetic field range of 0.54 ± 0.08 T. This re-entrant pairing also occurs for the case of $n = 3$ intersecting modes (Fig. 36C) where

70
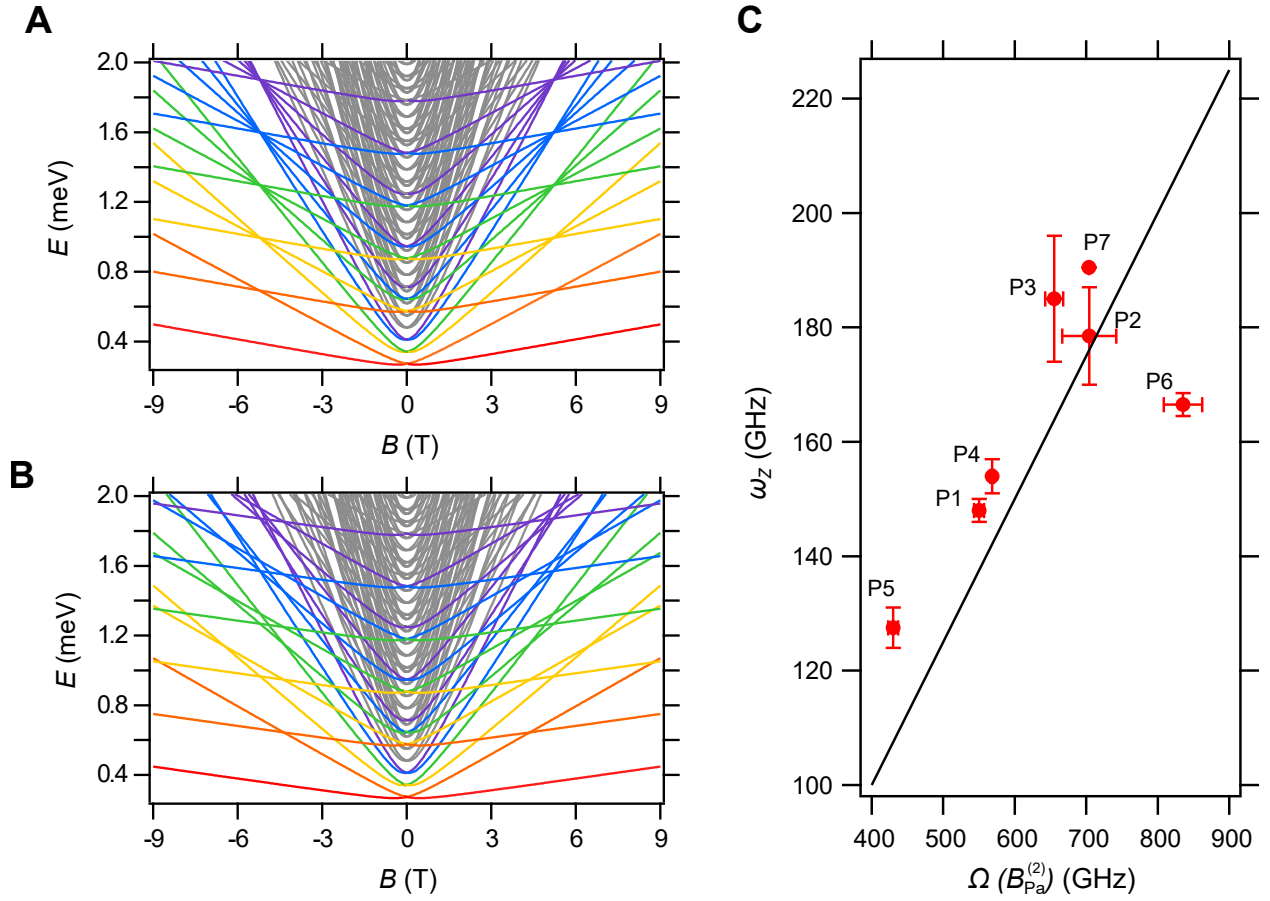
Figure 35: Subband energies for non-interacting electron waveguide model. **(A)** Energy E vs B calculated from the single-particle model, with parameters tuned to give Pascal degeneracies: $l_y = 33$ nm, $l_z = 10$ nm, $m_y = 1\ m_e$, $m_z = 5\ m_e$, $g = 1.0$. States are colored to highlight the bunching of increasing numbers of states to form the Pascal series conductance steps. **(B)** E vs B calculated from the single-particle model, where the parameters are detuned by 20%, destroying the crossing of the electron states: $l_y = 33$ nm, $l_z = 10$ nm, $m_y = 1\ m_e$, $m_z = 5\ m_e$, $g = 1.2$. **(C)** Plot of ω_z vs $\Omega(B_{\text{Pa}}^{(2)})$ for Devices P1-P7, shows that while ω_z and $\Omega(B_{\text{Pa}}^{(2)})$ vary significantly from sample to sample they are all near the theoretically-predicted critical value of $\omega_z/\Omega(B_{\text{Pa}}^{(2)}) = 0.25$, denoted by the solid black line.

a fit of the transconductance data indicates that the states are locked together over a range of 1.14 ± 0.15 T. Re-entrant locking of as many as $n = 6$ ($G = 21 \ e^2/h$) distinct intersections are observed (Fig. 34, Device P2). Pascal-liquid behavior is observed for a variety of devices written with both short (50 nm) and long (1000 nm) electron waveguides, and at different angles, ϕ, with respect to the crystallographic axis of the sample. These angles are listed in Table 3 and represent the angle of the waveguide device with respect to the (100) crystallographic direction. Devices with wires written at angles of 0°, 45°, or 90° show no significant difference.

4.3.3 DMRG analysis

A theoretical analysis more sophisticated than the single particle model discussed previously is required to capture the effects of electron-electron interactions. In the absence of interactions, the single-particle model described by Eq. 4.1 has band crossings but cannot predict any locking behavior. Prior work has demonstrated the existence of attractive electron-electron interactions in $LaAlO_3/SrTiO_3$ nanostructures [119, 137]. We therefore construct an effective lattice model for the waveguide by extending the non-interacting model to include phenomenological, local, two-body interactions between electrons in different modes. This effective model is investigated using the density matrix renormalization group (DMRG), a numerical method which produces highly-accurate results for strongly interacting systems in one dimension [132, 138, 139, 140, 141, 142, 143]. The DMRG phase diagrams in the vicinity of the $n = 2$ and $n = 3$ plateaus are shown in Fig. 37. The first set of calculations reveal a phase boundary line between a vacuum phase and an electron pair phase that is characterized by a gap to single-electron excitations. We associate this line to the $n = 2$ conductance step ($G = 3e^2/h$, Fig. 34B). Extending this calculation to three electron modes with attractive interactions ($n = 3$ plateau) reveals a transition line from the vacuum phase to a "trion" phase" which we associate with the $n = 3$ conductance step ($G = 6e^2/h$, Fig. 34B). The trion phase; is a 1D degenerate quantum liquid of composite fermions, each made up of three electrons, in which all one- and two-particle excitations are gapped out, but three-particle excitations are gapless. More details about our theoretical model and DMRG calculations can be found the supplementary materials of Ref. [129].
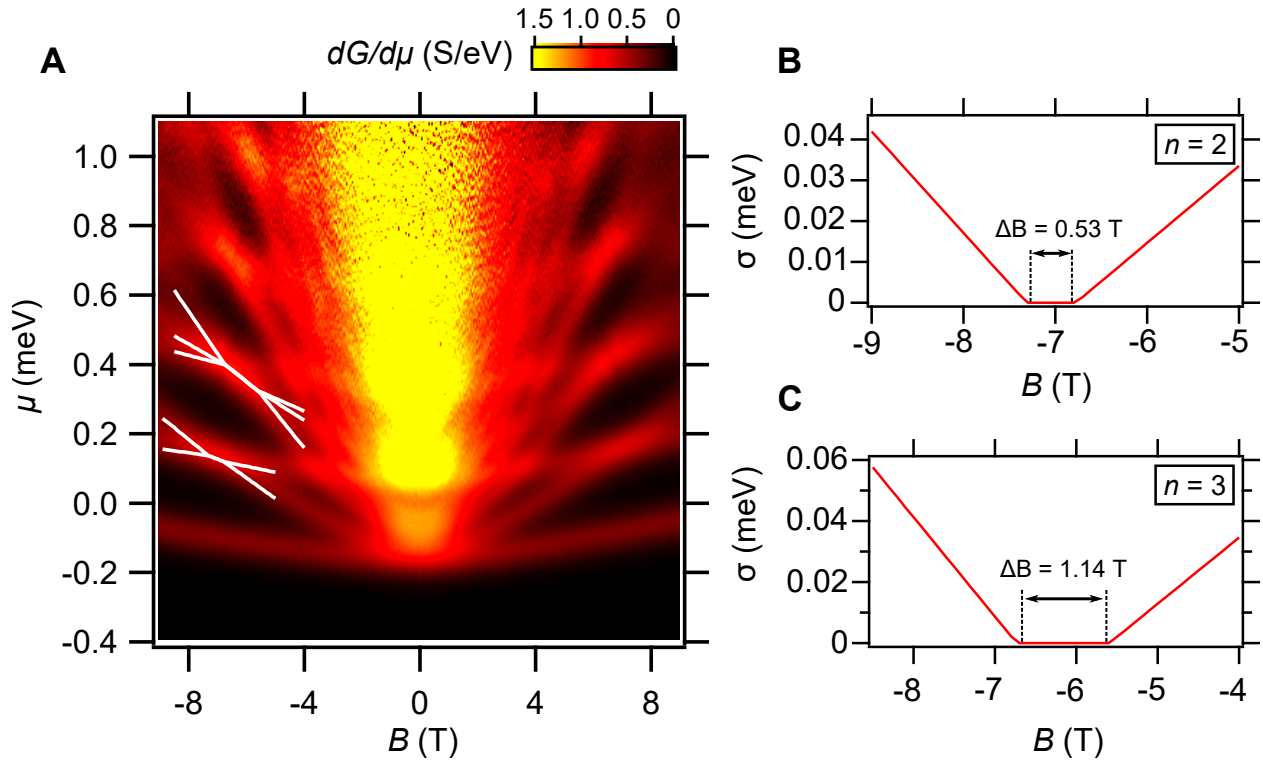
Figure 36: Pascal liquid phase transconductance fits. **(A)** Transconductance data for Device P6. White lines are fits of the peak locations for the $n = 2$ and $n = 3$ Pascal states calculated using a nine parameter non-linear least squares fit. **(B)** Standard deviation between states $|0,0,\uparrow\rangle$ and $|0,1,\downarrow\rangle$, forming the $n = 2$ Pascal state, from a fit of the experimental transconductance data in panel (A) showing the re-entrant pairing as the states come together and are locked for a range of magnetic field values, indicated by ΔB. **(C)** Fits for the trion state ($n = 3$) also produce a standard deviation that shows the three states converge and lock together for a range of magnetic field values, ΔB. A description of the fitting method can be found later in the chapter
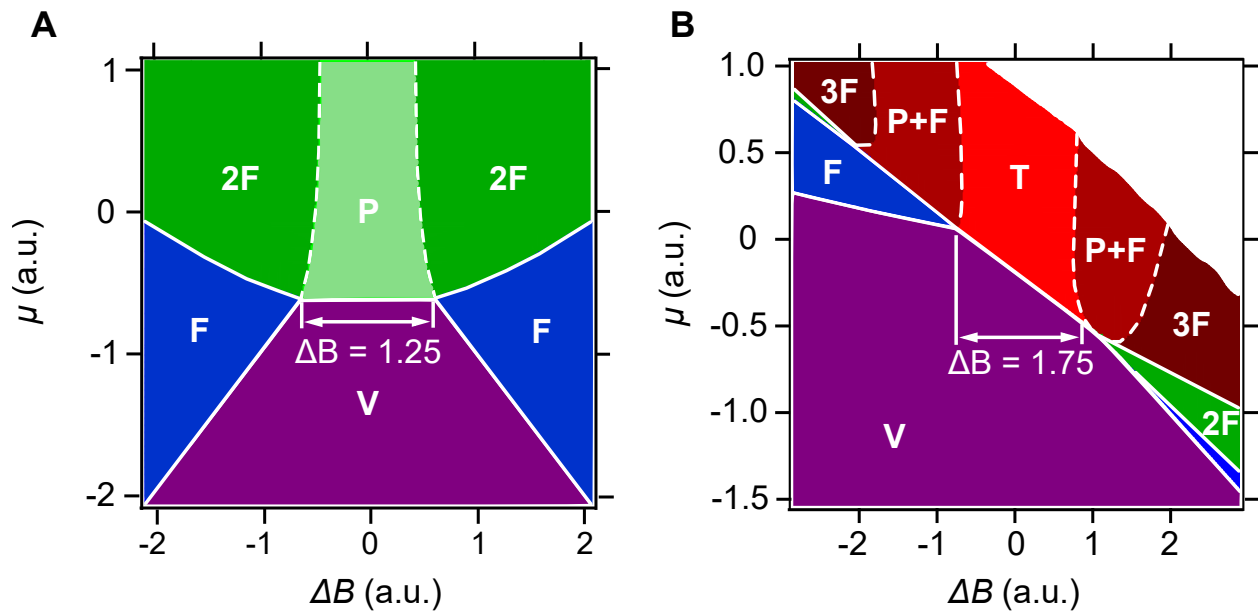
Figure 37: DMRG phase diagrams calculated for two **(A)** and three **(B)** fermions with attractive interactions in one dimension. Abbreviations for various phases: mF: m distinct Fermi surfaces, P: paired phase, T: trion phase, V: vacuum, A+B: phase composed of A and B. Solid while lines correspond to the fits highlighted in Fig. 36A. The white numbers on the plots indicate the strength of the locking for thee pair (A) and trion (B) phases. Similar to what is observed in fits of the experimental data, the trion phase is locked over a larger range of magnetic field values.

Here we discuss other theoretical explanations that we have considered. The addition of spin-orbit coupling to the non-interacting model modifies the subband structure, producing avoided crossings of the transconductance peaks. Anharmonicity of the confining potential, in the absence of interactions, bends the subband structure but also does not produce locking. We rule out impurity scattering effects due to the ballistic nature of the transport. Moreover, without inter-electron interactions (e.g. negative U center [144]), an impurity cannot produce locking phenomena. We are not aware of other mechanisms for locking, but cannot rule them out. Finally, we remark, that any theory of the locking phenomenon would need to have a non-interacting limit that matches with experiments, e.g. predict conductance quantization.

4.4 ANGLE-DEPENDENT MAGNETOTRANSPORT

The Pascal Condition assumes that the magnetic field is oriented out-of-plane. To investigate the effect of in-plane magnetic field components on the Pascal conductance series, we measure angle-dependent magnetotransport, with the magnetic field oriented at an angle θ with respect to the sample normal, within the y-z plane, $\vec{B} = B(\sin\theta\,\hat{y} + \cos\theta\,\hat{z})$ (Fig. 38A). In the out-of-plane orientation ($\theta = 0°$), characteristic Pascal behavior is observed, with subband locking taking place near 6 T (Fig. 38D, $\theta = 0°$). As θ increases, the trion phase associated with the $n = 3$ plateau destabilizes, while another (non-Pascal series) trion phase forms in a different region of parameter space (Fig. 38D, $\theta = 20°$, indicated by white lines). At larger angles (Fig. 38D, $\theta = 50°$), a dense network of reentrant pairing, disbanding, and re-pairing is observed. (See SOM for a video showing the evolution of the transconductance spectra from $\theta = 0°$ to $\theta = 90°$.) The strength of the re-entrant pairing of the $|0,0,\downarrow\rangle$ and $|0,1,\uparrow\rangle$ subbands is strongly-dependent on the angle θ of the applied magnetic field (Fig. 38C). The lower (B_R^-) and upper (B_R^+) magnetic fields over which these SBBs are locked together is indicated in Fig. 38D with red and blue circles. The magnetic field range ($\Delta B_R = B_R^+ - B_R^-$) is shown as a function of angle (Fig. 38C). The strength of the re-entrant pairing, ΔB_R, initially increases with angle, jumps discontinuously at $\theta = 30°$, as the SBBs (which have been shifting closer) snap together, and then decreases again. At $\theta = 0°$ there is a non-Pascal series crossing (no locking)

of like-spin states ($|0, 0, \downarrow\rangle$,$|0, 1, \downarrow\rangle$), highlighted by crossed lines, which evolves into an avoided crossing at $\theta = 10°$. This feature is explored in Fig. 38B where we plot conductance curves at $B = 3$ T for different angles.
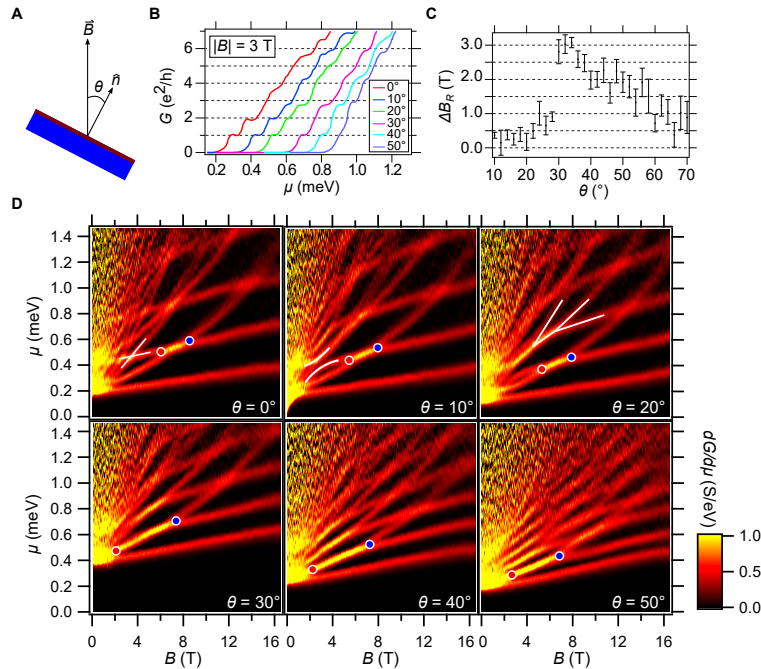
Figure 38: Angle-dependence of transport for Device P7. **(A)** Schematic of the sample with respect to the applied magnetic field $\vec{B}$, $\hat{n}$ is the vector normal to the sample and $\theta = 0°$ is the out-of-plane magnetic field angle. The magnetic field is in the YZ plane (perpendicular to the waveguide). **(B)** Conductance curves as a function of angle at $|B| = 3$ T. At $\theta = 10°$ an avoided crossing opens up, a plateau begins to form near $3e^2/h$. Evidence of reentrant pairing is seen when $\theta > 30°$ with conductance steps of $2e^2/h$. **(C)** Reentrant pairing strength as a function of θ. **(D)** Transconductance $dG/d\mu$ as a function of magnetic field strength B and chemical potential μ, at angle θ. The reentrant pairing strength is indicated where the states first lock together (red circles) and break apart (blue circles). $T = 30$ mK.

4.5 CONCLUSION

The "Pascal-liquid" phases reported here may constitute a new class of quantum degenerate electronic matter. Pascal composite particles would have a charge ne, where $n = 2, 3, 4, ...,$ and as-yet-undetermined spin quantum numbers. As with fractional fermionic states, it seems likely that the expected charge could be verified from a shot-noise experiment [145]. The particular Pascal sequence observed here experimentally is a consequence of the number of spatial dimensions in which they exist. Hypothetically, a material with four dimensions (three transverse to a conducting channel) could exhibit a conductance sequence $(1, 4, 10, 20, ...) \cdot e^2/h$, the next diagonal in the Pascal triangle. The Pascal sequence of bound fermions is reminiscent of the "quantum dot periodic table" used to categorize multi-electron states in semiconductor nanostructures [146]; the difference here is that the Pascal liquids are comprised of composite particles that are free to move in one spatial dimension, held together by mutual attraction rather than by an external potential profile. Pascal composite particles with $n > 2$ can be regarded as a generalization of Cooper pair formation, analogous to the manner in which quarks combine to form baryonic and other forms of strongly interacting, degenerate quantum matter. Interactions among Pascal particles are in principle possible—for example, trions could in principle "pair" to form bosonic hexamers. Coupled arrays of 1D waveguides can be used to build 2D structures. This type of structure is predicted to show a wide variety of properties ranging from sliding phases [147, 148, 149] to non-abelian excitations [73]. This highly flexible oxide nanoelectronics platform is poised to synthesize and investigate these new forms of quantum matter.

4.6 ADDITIONAL INFORMATION

4.6.1 Fits of transconductance data

To find the strength of the locking for the pair and trion phases we performed a nine parameter non-linear least squares fit of the transconductance data, where one of the param-

Table 3: Parameters for Pascal waveguide devices P1-P7. L_B is the width of the barriers in the waveguide, L_S is the separation between the barriers, L_C is the total length of the channel between the voltage sensing leads, ϕ is the angle between the nanowire and the (100) crystallographic direction. B_P indicates the pairing field, B_{Pa}^2 indicates the field at the center of the $n = 2$ Pascal phase. Single-particle model fits of experimental data determine the Landé factor g, the effective mass in the y direction m_y, frequencies associated with parabolic confinement in the lateral (y) direction and half-parabolic confinement in the vertical ($z > 0$) direction ω_y and ω_z, and the effective trapping frequency in the y-direction $\Omega(B_{Pa}^2)$.

Device	L_B (nm)	L_S (nm)	L_C (nm)	ϕ (°)	B_P (T)	$B_{\mathrm{Pa}}^{(2)}$ (T)	g	m_y (m_e)	ω_y (GHz)	ω_z (GHz)	$\Omega(B_{\mathrm{Pa}}^{(2)})$ (GHz)
P1	20	50	500	0	0.89	7.23	0.53	2.34	81	148	550
P2	20	50	500	0	3.01	6.66	1.11	1.68	94	178	704
P3	20	500	1500	0	1.66	4.79	0.95	1.45	131	131	596
P4	20	50	500	45	1.12	7.37	0.56	2.32	103	154	568
P5	20	50	500	45	1.42	6.69	0.55	2.81	97	127	429
P6	20	50	500	90	1.68	5.93	0.89	1.25	34	166	835
P7	30	1000	1800	0	0.22	7.68	0.58	1.94	99	190	703
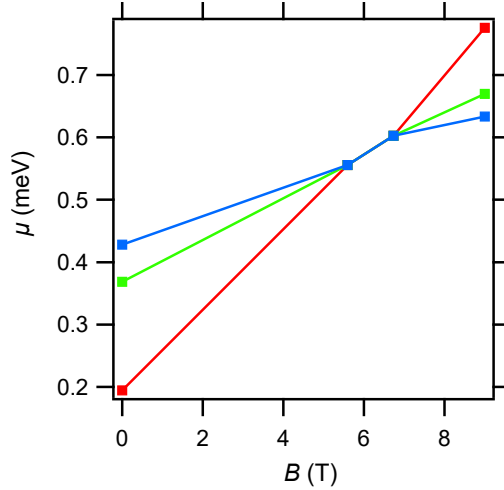
Figure 39: Model for transconductance fitting. Profile created from the nine parameter model to fit the transconductance data for the trion state. The results of the fit show a finite magnitude for the locked region.

eters in the model is the magnitude of the locked region. The nine parameters are used to create a profile of the phase, where two (pair) or three (trion) states come together and are locked over a range of magnetic field values. The nine parameters include the critical point at the center of the locked region, (B_c, μ_c), the magnitude and orientation of the locked region, the locations of each state at $B = 0$ T, and the magnitude and width of a $\sec^(x)2$ function, which is how the transconductance data is modeled. The profile used for fitting a trion state can be seen in Fig. 39. The fit was performed by minimizing the error function, which is the sum of the square of the difference between the transconductance data and the profile. To calculate the uncertainty of the results of the fit we calculated the Hessian of the error function.

4.6.2 Fits of conductance data

We also fit experimental data using a second method. The second method was used to fit the angle dependent data shown in Fig. 38, and find the strength of the reentrant pairing for the $|0, 0, \downarrow\rangle$ and $|0, 1, \uparrow\rangle$ subbands. The second fitting method involves a line by line nonlinear

least squares fit of the conductance data where each step in the conductance is modeled as a $\tanh(x)$ function, so that the total conductance is given as

$$G = \frac{A_1}{2}\left(1+\tanh\left(\frac{x-v_1}{w_1}\right)\right) + \frac{A_2}{2}\left(1+\tanh\left(\frac{x-v_2}{w_2}\right)\right) + ..., \tag{4.3}$$

where A_i is the amplitude of the ith step, v_i is the position of the step, and w_i is the width of the step. The step amplitude is restricted to be within 0.9 and 1.1 e^2/h. To determine how many steps are needed for each curve, the fit is performed with a range of possible steps, based on the maximum conductance of the curve, and the fit with the smallest residue (weighted mean square error between the best fit and the data) is chosen. The conductance curve at each magnetic field value was fit independently and by taking the difference between the step position of the second and third steps (the subbands that form the first paired state) we are able to determine the magnetic field value where the states pair (where the step positions are the same) and where the states break apart again, shown as red and blue circles in Fig. 38D.

5.0   One-dimensional Kronig-Penney superlattices at the LaAlO$_3$/SrTiO$_3$ interface

This chapter discusses 1D vertical superlattice devices created at the LaAlO$_3$/SrTiO$_3$ interface. The devices are created by adding a periodic vertical modulation to an electron waveguide device. The devices exhibit dispersive features not found in control devices and represent a first step towards developing a solid state quantum simulation platform.[1]

5.1   INTRODUCTION

The paradigm of electrons interacting with a periodic lattice potential is central to solid-state physics [150]. Semiconductor heterostructures [26, 27, 28] and ultracold neutral atomic lattices [14, 15, 16] capture many of the essential properties of 1D electronic systems. However, fully one-dimensional superlattices are highly challenging to fabricate in the solid state due to the inherently small length scales involved. Conductive atomic force microscope (c-AFM) lithography has recently been demonstrated to create ballistic few-mode electron waveguides with highly quantized conductance and strongly attractive electron-electron interactions [83]. Here we show that artificial Kronig-Penney-like superlattice potentials can be imposed on such waveguides, introducing a new superlattice spacing that can be made comparable to the mean separation between electrons. The imposed superlattice potential "fractures" the electronic subbands into a manifold of new subbands with magnetically-tunable fractional conductance (in units of e^2/h). The lowest $G = 2e^2/h$ plateau, associated with ballistic transport of spin-singlet electron pairs [83], is stable against de-pairing up to the highest magnetic fields explored ($|B| = 16$ T). These findings represent an important advance in the ability to design new families of quantum materials with emergent properties, and they mark a milestone in the development of a solid-state 1D quantum simulation platform.

Quantum theory provides a unified framework for understanding the fundamental properties of matter. However, there are many quantum systems whose behavior is not well

---

[1]This chapter is in preparation in another form for submission to Nature Physics.

understood because the relevant equations are are not able to be solved using known approaches. The idea of "quantum simulation", first articulated by Feynman [1], aims to exploit the quantum-mechanical properties of materials to compute the properties of interest and gain insight into the quantum nature of matter. There are two main "flavors" of quantum simulation: one based upon the known efficiency of circuit-based quantum computers to solve the Schrödinger equation, and the other based on control over open quantum systems to emulate a given Hamiltonian. The former approach is limited by the capabilities of present-day quantum computers. The latter approach has shown great promise using a variety of methods including ultracold atomic lattices [14, 15, 16], ion trap arrays [17, 18, 19] (which can simulate spin systems readily), superconducting Josephson junction arrays [20, 21, 22], photonic systems [23, 24, 25], and various solid-state approaches [26, 27, 28, 29, 151]. Platforms capable of quantum simulation of Fermi-Hubbard models would be of enormous value in condensed matter physics and beyond.

Complex oxides offer new opportunities to create a platform for quantum simulation in a solid-state environment. Their complexity gives access to important quantum phases of matter, such as superconductivity, where the model Hamiltonians (e.g., 2D Hubbard model) are challenging to understand theoretically, while their nanoscale reconfigurability makes it possible to engineer new forms of quantum matter with extreme nanoscale precision [4, 5].

Here we present experiments which constitute a first step towards developing a solid-state quantum simulation platform based on a reconfigurable complex-oxide material system. Using conducting atomic force microscope (c-AFM) lithography, we create Kronig-Penney-like [152] 1D superlattice structures by spatially modulating the potential of a 1D electron waveguide device at the $LaAlO_3/SrTiO_3$ interface. Two main effects are found. The superlattice modulation introduces new fractional conductance features that are believed to be the combined result of enhanced electron-electron interactions and the new periodic structure. The potential modulation also significantly enhances the stability of spin-singlet pair transport. The unique combination of strongly attractive electron-electron interactions, combined with the engineered properties demonstrated here, hold promise for the development of new families of quantum materials with programmable characteristics.

C-AFM lithography has been used to create a variety of devices at the $LaAlO_3/SrTiO_3$ in-

terface [33]. A conductive AFM tip, moving in contact with the $LaAlO_3$ surface and positively-biased with respect to the $LaAlO_3$/$SrTiO_3$ interface, locally creates ("writes") conducting regions at the interface (Fig. 40(A)), while a negatively biased tip locally restores ("erases") the interface to an insulating state. The mechanism behind the writing (erasing) is the local (de)protonation of the $LaAlO_3$ surface [87, 88]. The protons on the surface create a confining potential which defines the conducting regions at the interface. This technique achieves nanoscale control, with precision as high as 2 nm, over the conductivity of the $LaAlO_3$/$SrTiO_3$ interface and most of its properties.

The work described here concerns $LaAlO_3$/$SrTiO_3$ electron waveguide devices [83] that have been perturbed by a spatially periodic potential, similar to the one first envisioned by Kronig and Penney [152]. Unperturbed waveguides exhibit highly quantized ballistic transport with conductance steps at or near integer values of the conductance quantum e^2/h. The subband structure of $LaAlO_3$/$SrTiO_3$ electron waveguides can be described by a waveguide model which takes into account vertical, lateral, and spin degrees of freedom [83]. Representative orbitals for electron waveguides, subject to parabolic lateral confinement and half-parabolic vertical confinement, are shown in Fig. 40(B), where $|m, n, s\rangle$ is a state specified by quantum numbers m, n, and s that correspond to the number of lateral (m) and vertical (n) nodes of the wavefunction, and the spin s. The complete set of states form a basis for describing extended states along the waveguide direction x. The periodic modulation of the waveguide may couple different vertical modes (for example those highlighted in black in Fig. 40) with the ground state $|0, 0, \uparrow\rangle$. Due to attractive electron-electron interactions, subband energy minima can "lock" together to form electron pairs [83] that also propagate ballistically. Pairing in electron waveguides arises from the same electron-electron interactions that give rise to superconductivity [119]. In some cases, more exotic locking of subbands can occur, e.g., the Pascal conductance plateaus which indicate the pairing of $n \geq 2$ electron states [129]. The presence of strong, tunable electron-electron interactions makes these electron waveguide devices an interesting starting point for engineering 1D quantum systems.
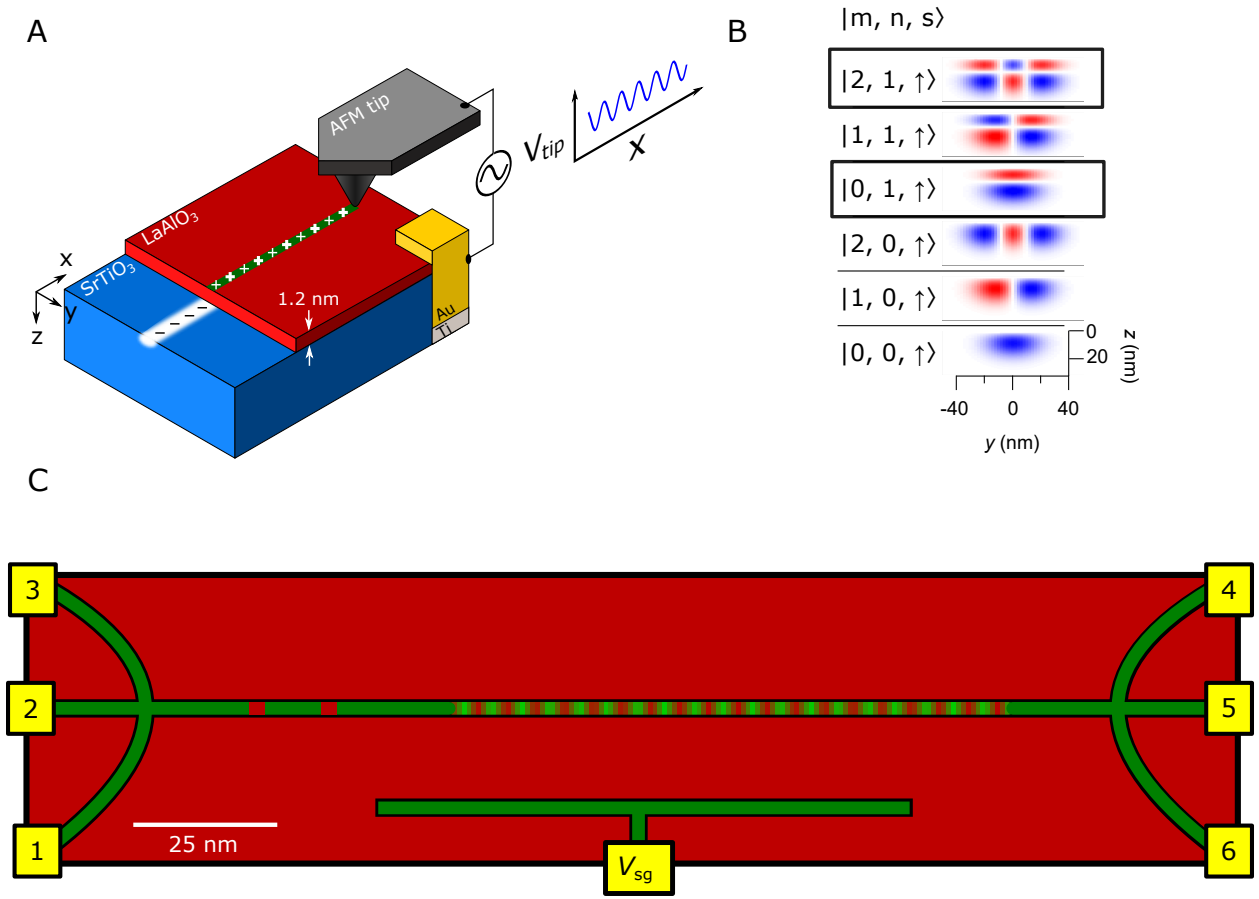
Figure 40: Schematic of c-AFM writing and 1D vertical superlattice device. **(A)** C-AFM writing schematic. A positive bias on the AFM tip protonates the $LaAlO_3$ surface, locally creating a conducting channel at the $LaAlO_3/SrTiO_3$ interface. Modulation of the tip voltage, V_{tip}, while writing adds a Kronig-Penny like periodic structure to the electron waveguide device. **(B)** Chart showing different representative wavefunctions calculated using a single particle model for electron waveguide devices [83]. The imposed vertical superlattice structure may cause mixing of vertical modes of an electron waveguide device, possibly mixing the ground state with modes highlighted in black. **(C)** 1D vertical superlattice device schematic. The superlattice is created by first writing the main channel with a positive tip voltage. The same path is then traced while applying a sinusoidal tip voltage to periodically modulate the confining potential of the device. The superlattice in created in series with two highly transparent tunnel barriers.

5.2   RESULTS

1D superlattice devices are created by first writing a conductive nanowire with a constant positive voltage applied to the AFM tip ($V_{\text{tip}} \sim 10\,\text{V}$). The same path is re-traced along the same direction while applying a sinusoidally varying tip voltage $V_{\text{tip}}(x) = V_0 + V_k \sin(kx)$, to produce a spatially periodic potential modulation. A short unpatterned waveguide is written in series next to the superlattice, which helps to control the chemical potential in the device structure [83]. Four-terminal magnetotransport measurements are carried out in a dilution refrigerator at or near its base temperature $T = 25\,\text{mK}$.

5.2.1   Magnetotransport data

Fig. 41A shows the transconductance dG/dV_{sg} as a function of out-of-plane magnetic field B and side-gate voltage V_{sg} for 1D vertical superlattice device V1. The transconductance map provides a visual indication of the subband structure. Purple regions, where the transconductance is nearly zero, represent conductance plateaus. Bright colored (red/yellow/green/blue) regions signify increases in conductance that generally correspond to the emergence of new subbands. White regions indicate negative transconductance, resulting from an overshoot in conductance. The transconductance is generally found to be highly symmetric with respect to the applied magnetic field. By comparison, Fig. 41B shows a calculated transconductance map for a single-particle model of a straight, unmodulated electron waveguide. The non-interacting waveguide model includes the geometry of a typical electron waveguide device as well as vertical, lateral, and spin degrees of freedom, and is described in more detail elsewhere [83]. The experimental data for the superlattice shows an overall resemblance to the waveguide model, except that the subbands are "fractured" into a manifold of new states with fractional conductances. Fig. 41C shows a series of conductance curves versus V_{sg} for a sequence of out-of-plane magnetic fields B, ranging between 0 T (leftmost) to 16 T (rightmost). Curves are offset by $\Delta V_{sg} \sim 7.5\,\text{mV/T}$ for clarity and curves at 1 T intervals are highlighted in black. At low magnetic fields ($|B| \approx 2\,\text{T}$), a plateau at around 1.8 e^2/h develops before bifurcating into two distinct plateaus, one of which decreases in value, while the

85

other increases towards a nearly quantized value of 1.99 e^2/h. The onset of the two plateaus can be seen clearly in the transconductance (Fig. 41A) as a minigap that appears in the lowest subband.

5.2.2 Fractional conductance features

In addition to the plateau at 2 e^2/h, many other subband features are readily seen at higher conductance values. Some of the subbands that make up this additional manifold of states are shown in more detail in Fig. 42. Conductance curves at several parameter values are shown in Fig. 42C-E. Corresponding colored boxed, as a guide to the eye, indicate where these curves exist within the transconductance map (Fig. 42A) and the full range of conductance curves (Fig. 42B). In Fig. 42B and C there are several conductance plateaus visible. The conductance increases between these plateaus correspond new subbands, the so-called "fractured" states, becoming available in the transconductance map. These appear to be fractional subbands as the increase in conductance between the plateaus are fractions of the conductance quanta e^2/h. Fig. 42E shows the fractional conductance feature occurring below the 2 e^2/h plateau in more detail. The feature first appears in the form of a conductance peak then bifurcates forming the $\sim$ 2 e^2/h plateau, and a lower fractional conductance feature that evolves downward in conductance with magnetic field.

Data for a second superlattice device (device V2), shown in (Fig. 44), yields qualitatively similar behavior. The overall subband structure resembles the subband structure of an electron waveguide device with no superlattice patterning, but the subbands are, like with Device V1, "fractured" into additional manifolds with fractional conductance plateaus. Device V2 also shares the prominent highly quantized conductance plateau at 2 e^2/h.

5.2.3 Finite-bias spectroscopy

Finite-bias spectroscopy for 1D superlattice device V1 (Fig. 43) reveals a characteristic diamond structure in the transconductance. This feature is associated with clean ballistic transport [127, 128] and is due to unevenly populated subbands at large finite biases which give rise to half-plateaus. The diamond visible in the transconductance corresponds to a fractional
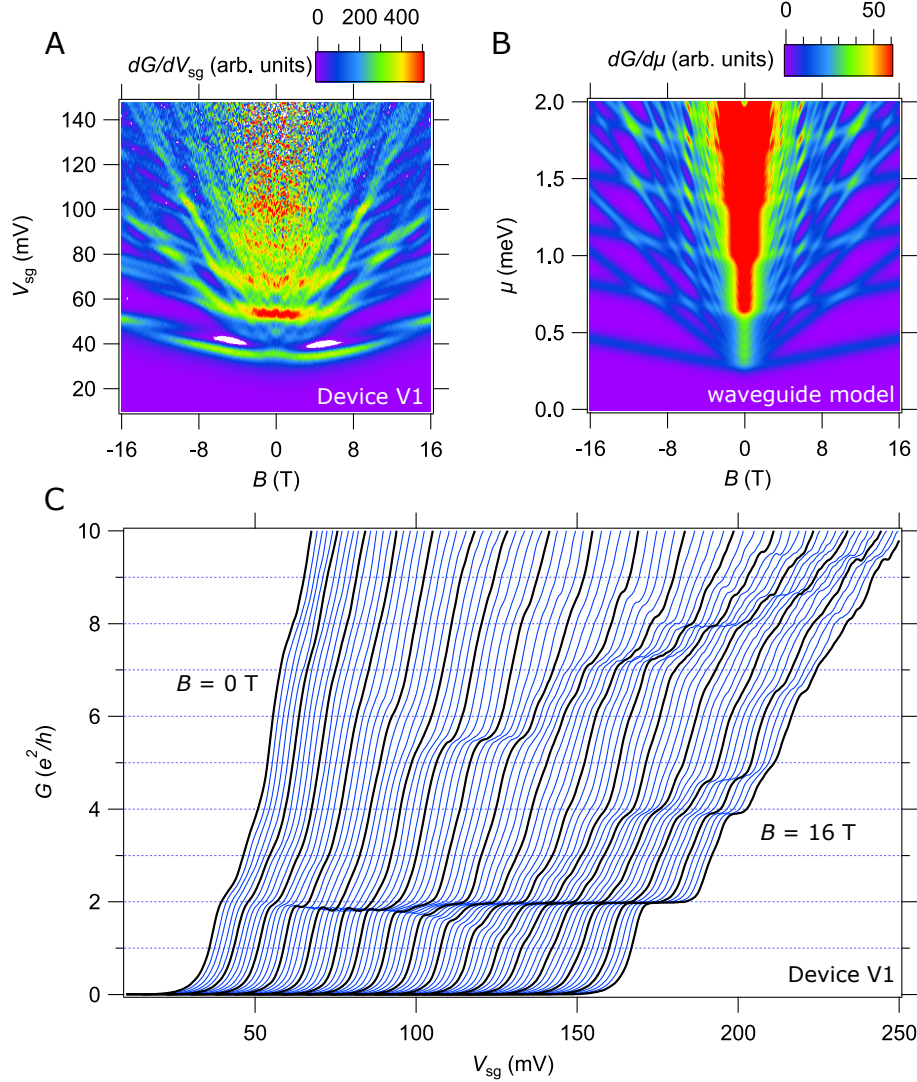
Figure 41: Magnetotransport characteristics of a 1D vertical superlattice. **(A)** Transconductance dG/dV_{sg} as a function of magnetic field B and side gate voltage V_{sg} for vertical superlattice Device V1. Purple regions indicate zero transconductance, or conductance plateaus. Bright regions indicate increasing conductance when new 1D subbands become available. Negative transconductance is indicated in white, mainly in two lobes above the $2\,e^2/h$ plateau around 5 T. **(B)** Transconductance spectra for non-interacting single-particle electron waveguide model. **(C)** Conductance G vs side gate voltage V_{sg} at magnetic fields from $B = 0$ T to 16 T for Device V1. Curves are offset by $\Delta V_{sg} \sim 7.5$ mV/T for clarity. Curves at 1 T intervals are highlighted in black.
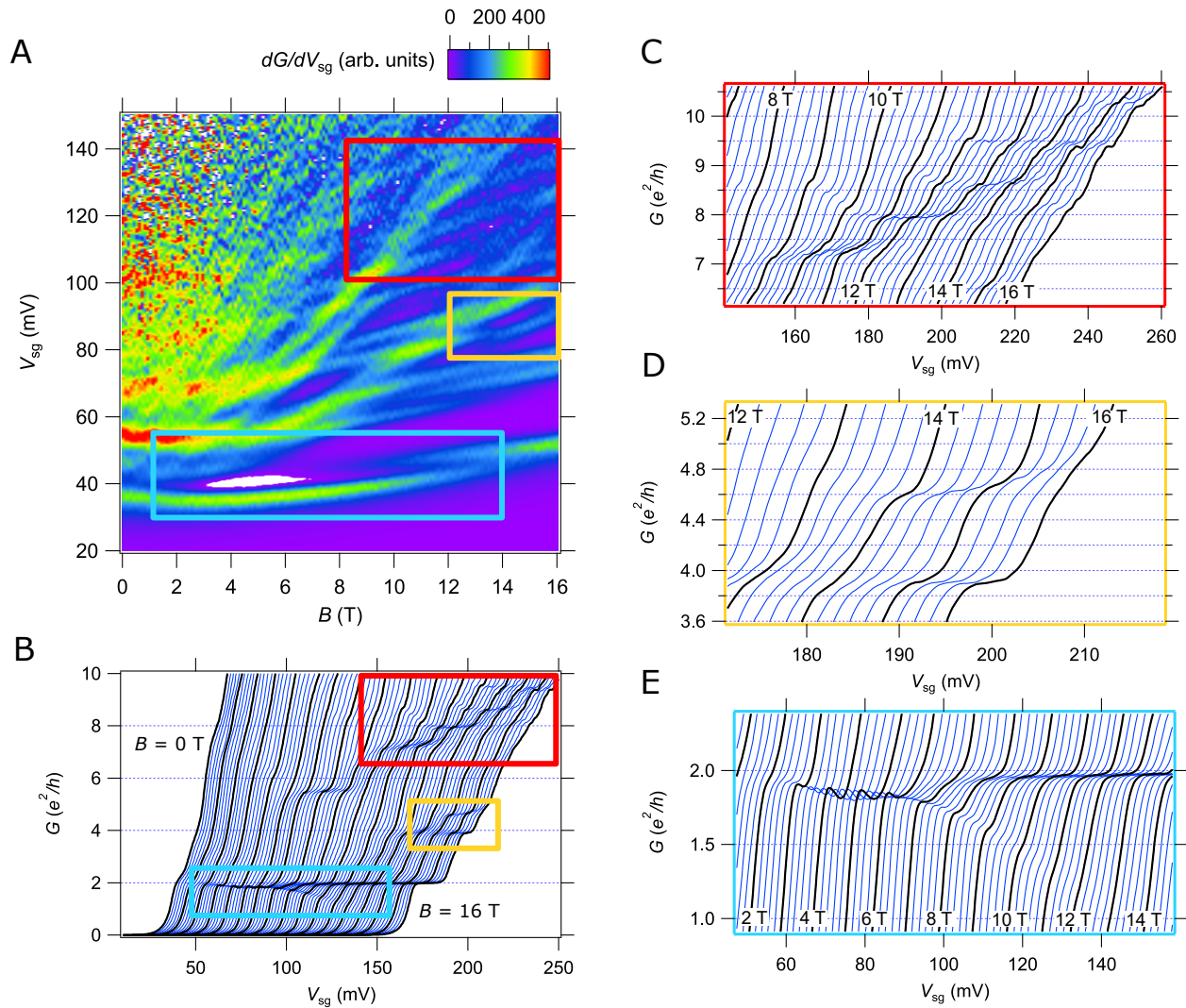
Figure 42: Fractional conductance features for vertical superlattice Device V1. **(A)** Transconductance map with regions highlighted in colored boxes as a guide to the eye to indicate the location of the conductance curves. **(B)** Full conductance curves with colored boxes indicating corresponding locations in the transconductance map and other conductance panels. **(C)** and **(D)** Conductance curves showing conductance plateaus which correspond to the "fractured" states in the transconductance map. The conductance jump between the plateaus are fractions of the conductance quanta e^2/h. **(E)** Conductance curves highlighting the fractional conductance feature occurring below the 2 e^2/h plateau.

conductance feature below the $2\,e^2/h$ plateau at around $0.5\,e^2/h$ (circled in pink curve) at zero-bias and about half that value at finite-bias (circled in blue curve). The presence of this characteristic diamond structure rules out the likelihood that the fractional features are due to reduced transmission in the channel.

Control devices, straight unmodulated waveguides (discussed in more detail in Ref. [83, 129] and Chapter 3 and 4), do not show fractional conductances. Although not shown here, the behavior of such "control" devices consists mainly of conductance plateaus that are quantized in integer values of e^2/h, i.e., lacking in the fractionalized subbands observed here.

5.3   DISCUSSION

The existence of fractional conductance states in 1D transport is generically an indication of strong electron-electron interactions. The fractional quantum Hall state [153] is perhaps the best known and investigated example, although fractional conductances have been observed in 1D quantum point contacts [78, 79] (so-called "0.7 anomaly"). The origin of the "0.7 anomaly" has been under debate since it was first reported [154], but it has recently been found that electron-electron interactions play an important role in the formation of the feature observed at $0.7 \times (2e^2/h)$ [155]. The "0.7 anomaly" has also been observed in 1D quantum point contacts in MgZnO/ZnO oxide heterostructures [80], where they observe features that resemble the "$N.7$ anomaly" below 1D subbands, up to the $N = 5$ subband. The observation of the "0.7" shoulder in higher subbands is uncommon in GaAs-based systems and is possibly due to the strong interactions in this oxide system.

There have been several theoretical predictions of fractional conductance features in few channel 1D systems with strong electron-electron interactions [156, 157]. Shavit *et al.* [157] consider a 1D system with multiple channels and strong (repulsive) electron-electron interactions. The strong electron-electron interactions enable momentum-conserving back-scattering processes in the nanowires which leads to fractional conductance states. Fractional conductance features have recently been observed experimentally in several systems including strained Ge-based hole quantum wires [158] and GaAs-based quantum wires [159]. The
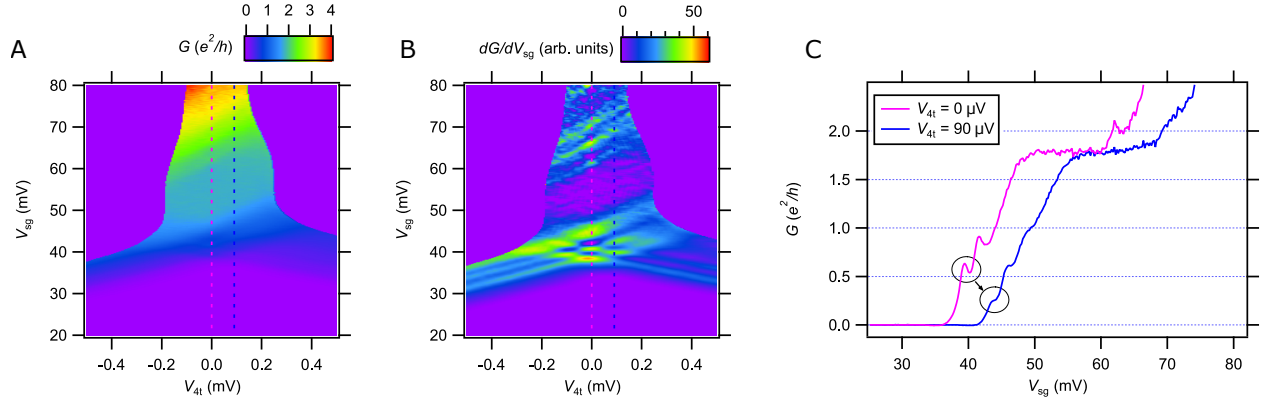
Figure 43: Finite-bias spectroscopy for Device V1. **(A)** Conductance (G) intensity map as a function of four-terminal voltage V_{4t} and side gate voltage V_{sg}, pink and blue dashed lines indicate the locations for the vertical linecuts shown in **(C)**. **(B)** Transconductance (dG/dV_{sg}) intensity map as a function of four-terminal voltage V_{4t} and side gate voltage V_{sg}. The transconductance map shows the diamond features indicating ballistic transport in the superlattice devices. **(C)** Vertical conductance linecuts at $V_{4t} = 0$ and 90 μV. Circles indicate fractional conductance values below the ∼ 2 e^2/h plateau (corresponding to the lowest diamond features visible in the transconductance map in panel **(B)**) that become half of their value at a finite bias. Curves are offset for clarity. Data taken at $B = 13$ T.

fractional conductance features were observed at low carrier concentrations when the confinement of the wire was relaxed to increase the role of interactions. The presence of strong (repulsive) electron-electron interactions were essential to the formation of the fractional conductance features.

Unlike the experimental systems discussed above, which have repulsive electron-electron interactions, a defining characteristic of the $LaAlO_3/SrTiO_3$ system is the prevalence of strong *attractive* electron-electron interactions [119, 137, 83, 129]. However, attractive interactions alone do not produce fractional conductance plateaus.

Devices at the $LaAlO_3/SrTiO_3$ interface exhibit electron pairing without superconductivity [119, 83]. In electron waveguides, this interaction causes electron subband energy minima to lock together, either near zero magnetic field or at re-entrant values, resulting in conductance steps of 2 e^2/h. The superlattice modulation of the electron waveguides is empirically linked to enhanced electron pairing fields. The effect is significant: superlattice devices have pairing fields of $B_P > 16$ T. Control devices written in the same area of the sample (electron waveguide device W3) show smaller pairing fields $B_P \sim 11$ T [83]. The enhanced pairing strength appears to be a consequence of the potential modulation, although the physical mechanism is unclear. Superlattices formed by lateral modulation do not always show an enhanced pairing field [160].

Another effect that is correlated with the vertical modulation is a spin-orbit like effect in the device. The lowest subband in device V1 (seen in the transconductance map in Fig. 41B) bends upward at zero magnetic field, so that the minima of the lowest subband are at a finite magnetic field. This may be due to the engineering of a spin-orbit field, and is not usually observed in quasi-1D electron waveguide devices at the $LaAlO_3/SrTiO_3$ interface. This effect is more pronounced in lateral 1D superlattice devices [160] (discussed in Chapter 6).

The ability to create new superlattice structures, and modulate interactions in 1D systems, opens new frontiers in the development of quantum matter. The systems created here focus on low-dimensional confined structures, which are challenging to create using other methods. The regular superlattice structure can be replaced with quasiperiodic order, artificially imposed disorder, topological defects, or combined with lateral perturbations, to name just a few possibilities. Unlike the Kronig-Penney description, electron-electron interactions play a

defining role in the resulting quantum phases, and future discoveries of emergent phases in this family of 1D systems are highly likely.

5.4   ADDITIONAL INFORMATION

5.4.1   Device writing and measurement parameters

Devices V1, V2 and W3 were written in the same location on the LaAlO$_3$/SrTiO$_3$ sample during different cooldowns. 1D vertical superlattice devices V1 and V2 were written with the same c-AFM writing parameters. The first pass of the main channel was written with a tip voltage $V_{tip} = 12$ V at a speed of 50 nm/s. The barriers for the electron waveguide had a width of $L_B = 5$ nm and were separated by $L_S = 10$ nm and created by applying negative voltage pulses of -9 V at a speed of 5 nm/s. The superlattice was created by applying a tip voltage $V_{tip}(x) = 5$ V $\cdot \sin((\pi/5 \text{ nm})x)$ with 18 periods.

Data was taken at base temperature of a dilution refrigerator $T \sim 30$ mK. Transport data for 1D superlattice devices was taken using standard lockin techniques with an oscillation amplitude of 1 mV (250 μV) at a reference frequency of 11 (13.46) Hz for Devices V1 (V2). More examples of typical electron waveguide devices can be found in Ref. [83, 129] and Chapters 3 and 4.

5.4.2   Device V2

The transport in Device V2 is not as clean as Device V1. There was also an issue with the side gate leaking at low side-gate and magnetic field values, causing the data to be distorted.
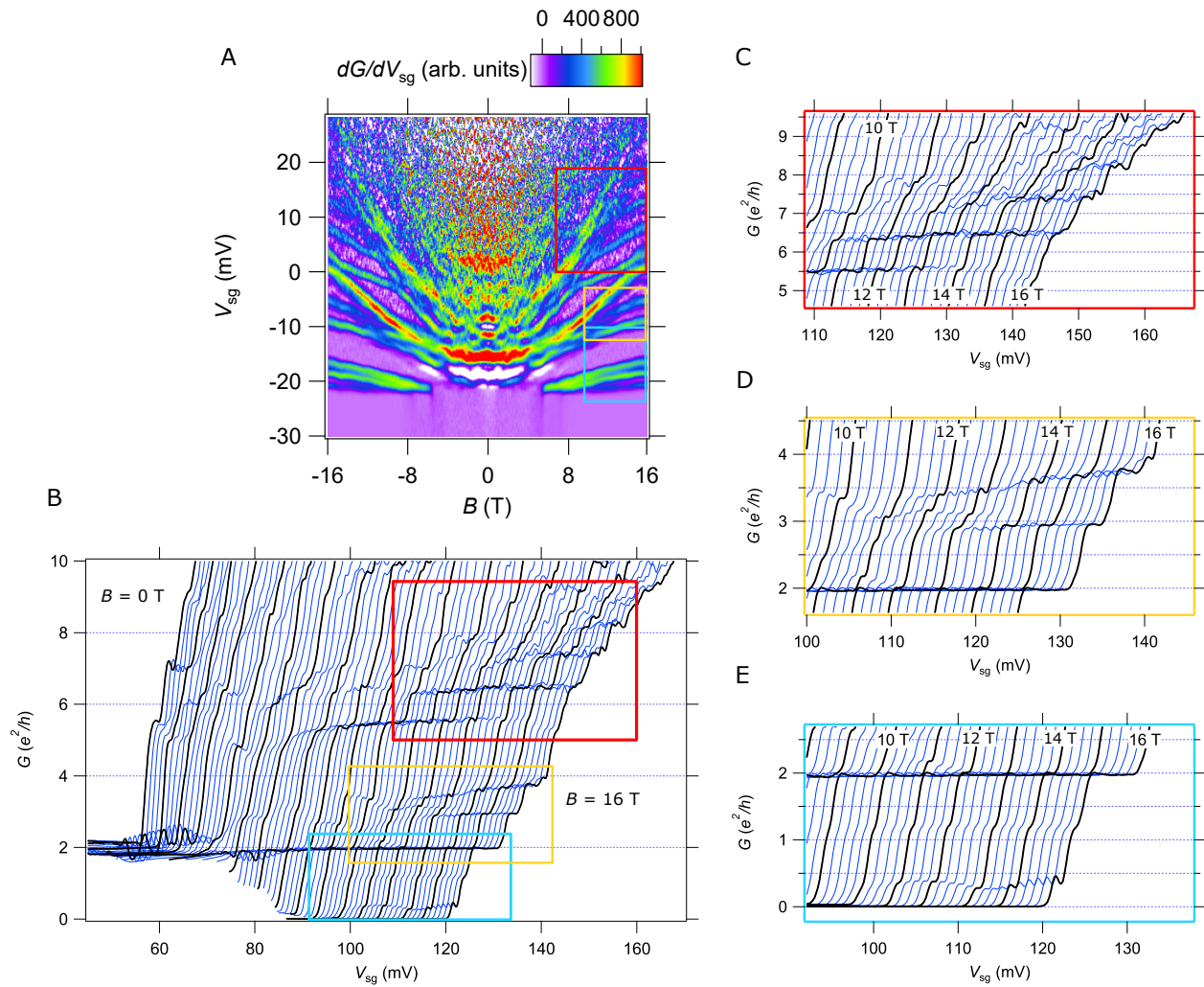
Figure 44: Magnetotransport data for vertical superlattice device V2. **(A)** Transconductance map dG/dV_{sg} as a function of side gate voltage V_{sg} and magnetic field B. Purple regions indicate conductance plateaus, zero transconductance. Red/yellow/green/blue regions indicate increases in conductance when new subbands become available. White regions indicate negative transconductance. Colored boxes are guides to the eye indicating the location of highlighted conductance curves. **(B)** Plot showing full conductance data. Conductance curves at 1T intervals are highlighted in black and are offset clarity. **(C)**-**(E)** Conductance G as a function of side gate voltage V_{sg} curves at different out-of-plane magnetic field B values highlighting some fractional conductance features..

6.0 Engineered spin-orbit interactions in $LaAlO_3$/$SrTiO_3$-based 1D serpentine electron waveguides

This chapter describes experiments studying 1D lateral superlattice devices at the $LaAlO_3$/$SrTiO_3$ interface. The devices were created by adding a periodic lateral or "serpentine" modulation to electron waveguide devices. Transport measurements reveal fractional conductance plateaus and evidence of an engineered spin-orbit interaction in the devices.[1].

6.1 INTRODUCTION

The quest to understand, design, and synthesize new forms of quantum matter guides much of contemporary research in condensed matter physics. One-dimensional (1D) electronic systems form the basis for some of the most interesting and exotic phases of quantum matter [95]. The variety of experimentally-accessible ballistic 1D electronic systems is highly restricted, and furthermore these systems typically have few tuning parameters other than electric and magnetic fields. However, electron waveguides [83] formed from two-dimensional (2D) $LaAlO_3$/$SrTiO_3$ heterointerfaces exhibit remarkable 1D properties, including ballistic multi-mode transport and strong attractive electron-electron interaction [119, 137], but these systems conspicuously lack strong or tunable spin-orbit interactions. Here we describe a new class of quasi-1D nanostructures, based on $LaAlO_3$/$SrTiO_3$ electron waveguides, in which a sinusoidal transverse spatial modulation is imposed. Nanowires created with this "serpentine" modulation display unique dispersive features in the subband spectra, namely (1) a significant shift ($\sim$ 7 tesla) in the spin-dependent subband minima, and (2) fractional conductance plateaus, some of which are continuously tunable with a magnetic field. The first property can be understood as an engineered spin-orbit interaction associated with the periodic acceleration of electrons as they undulate through the nanowire (ballistically), while the second property signifies the presence of enhanced electron-electron scat-

---

[1]This chapter is in preparation in another form for submission to Nature Physics.

tering in this system due to the imposed periodic structure. The ability to engineer these interactions in quantum wires contributes to the tool set of a 1D solid-state quantum simulation platform.

One approach to the grand challenge of understanding new states of quantum matter is through "quantum simulation", the creation of a highly configurable many-body quantum system is developed in which its Hamiltonian description can be related to relevant physical models [1, 12, 13]. Quantum simulation necessarily requires a physical platform that can be configured to match or approximate the system of interest. Among the many quantum systems being developed for this purpose, ultracold atoms trapped within standing waves of light [15] have been particularly successful, in large part because the model Hamiltonians are well characterized and based upon a fundamental understanding of the constituent atomic systems. For example, hyperfine states of trapped ions have been greatly successful in simulating classes of spin chains [18, 19]. Superconducting networks can also be used to simulate a wide range of Hamiltonians [20], while atom-scale manipulation (e.g., donor atoms in silicon [161] or arrangements of CO molecules [162]) has successfully emulated band structure and topological phases.

The type of quantum systems that can be explored in a quantum simulator is often limited by the available interactions of the host material. To increase the available physical interactions, a variety of pseudo-magnetic fields [163, 164], gauge fields [165], and spin-orbit interactions [166], can be added. Inter-particle interactions can be controlled in a variety of ways, e.g., via Feshbach resonance in atomic systems, or by coupling to a polarizable medium [134].

The complex-oxide $SrTiO_3$ possesses a wide range of gate-tunable properties that include superconductivity, magnetism, ferroelectricity, and ferroelasticity [33]. Using a conductive atomic-force microscope (c-AFM) lithography technique, the $LaAlO_3/SrTiO_3$ interfacial conductivity (and related properties) can be programmed with a precision of two nanometers [4, 5], comparable to the mean separation between electrons. The combination of a rich palette of intrinsic properties and the ability to form complex nanostructures provides a suitable foundation for the creation of a 1D quantum simulation platform.

A useful starting point for developing programmable 1D quantum systems is the $LaAlO_3/SrTiO_3$ electron waveguide [83]. These devices exhibit highly-quantized ballistic

transport, in which the conductance is quantized in units of e^2/h, where e is the electron charge and h is the Planck constant. Each of the N occupied 1D subbands (arising due to vertical, lateral, and spin degrees of freedom) contributes one quantum of conductance to the total conductance $G = Ne^2/h$. A variety of correlated electronic phases have been identified, including a paired liquid phase [119, 83], re-entrant pairing [83], and a family of emergent composite electron liquids comprised of bound states formed from 2,3,4,... electrons [129]. The calculated wavefunctions of a representative electron waveguide device are shown in Fig. 45C, where the state $|m, n, s\rangle$ is indentified by its quantum numbers m, n, and s that characterize the transverse orbital and spin degrees of freedom. Much of the unusual transport characteristics come from interactions between these various electronic subbands.

One property that appears to be lacking (or weak) in $LaAlO_3/SrTiO_3$ electron waveguides is spin-orbit coupling. Gate-tunable spin-orbit coupling has been reported at the 2D $LaAlO_3/SrTiO_3$ interface [47, 48]; however, detailed modeling of the subband spectra have ruled out such interactions for the most part in 1D quantum wires [83]. Strong spin-orbit interactions are believed to be the "missing ingredient" in efforts to create Majorana zero modes [167, 168] in these 1D quantum wires. A reasonable goal is therefore to engineer spin-orbit interactions in quantum wires, using the nanoscale control enabled by c-AFM lithography.

Here we present transport experiments on ballistic electron waveguides that are perturbed by a periodic transverse ("serpentine") spatial modulation (Fig. 45). Conductive nanostructures are created at the $LaAlO_3/SrTiO_3$ interface using a positively-biased c-AFM tip placed in contact with the $LaAlO_3$ surface, locally switching the interface to a conducting state because of local protonation of the $LaAlO_3$ surface [87, 88]. We perturb the electron waveguide structure by superimposing a periodic transverse modulation to the device (Fig. 45). The path for a sinusoidal waveguide oriented along the x direction is given by $y(x) = y_0 + y_k \sin(kx)$, where y_0, y_k and k are parameters that can be programmed. The impact of this modulation on the transverse mode, expressed using the basis of unperturbed states ($|m, n, s\rangle$), is expected to be dominated by the $|1, 0, s\rangle$ state, with a higher correction from the $|2, 0, s\rangle$ state (Fig. 45B).
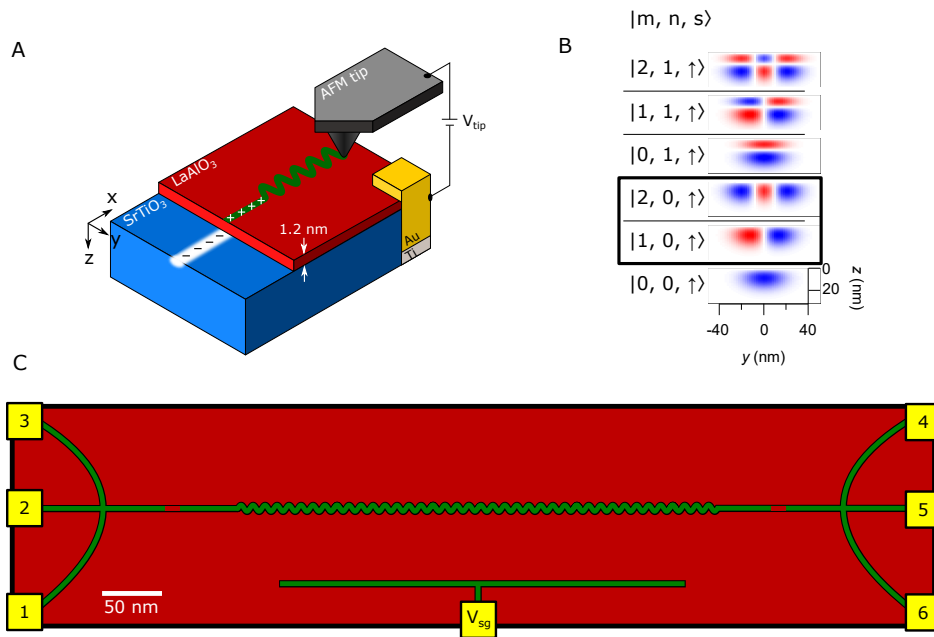
Figure 45: Conductive AFM writing and device schematic for lateral superlattice devices. **(A)** Nanowires created at the LaAlO$_3$/SrTiO$_3$ interface using c-AFM lithography. A positively-biased AFM tip protonates the surface, causing electrons to accumulate at the interface. 1D serpentine superlattice devices are created by laterally modulating the tip position on the LaAlO$_3$ surface. **(B)** Representative wavefunctions calculated for an electron waveguide device with vertical, lateral, and spin degrees of freedom [83]. The serpentine motion of the superlattice couples the ground state of the waveguide with different lateral modes of the waveguide (modes circled in black). **(C)** Schematic for the 1D serpentine superlattice devices. C-AFM written paths (green lines) represent the device and are connected to interface electrodes (yellow). The serpentine lateral modulation is bracketed by highly transparent tunnel barriers similar to those used to create electron waveguide devices [83]. The voltage/current leads are used to take a 4-terminal measurement of the device. A local side gate is also created using c-AFM lithography. A voltage applied to the gate (V_{sg}) changes the chemical potential of the device.

6.2 RESULTS

6.2.1 Magnetotransport data

Four-terminal magnetotransport data for a serpentine superlattice (Device L1) is shown in Fig. 46. Measurements are taken at or near the base temperature of a dilution refrigerator ($T = 25$ mK), as a function of out-of-plane magnetic field $|B| \leq 18$ T and chemical potential μ, which is controlled by the voltage on a local side gate. Device design parameters are summarized in Table 5. The four-terminal conductance G as a function of μ and B (Fig. 46A) shows quantized plateaus that result from Landauer quantization, similar to what is observed for unperturbed (straight) electron waveguides. In addition, the device shows a number of fractional conductance plateaus. Two features are highlighted in red, and shown in expanded detail in Fig. 46C. The conductance value of the fractional feature at high B field evolves down from the $\sim 1\ e^2/h$ plateau, reaching a value of $\sim 0.4\ e^2/h$ at $B = 18$ T. A smaller fractional conductance feature, $\sim 0.2\ e^2/h$ near zero magnetic field, remains stable until about $B = 1$ T, and then decreases in magnitude with increasing B field before disappearing at $B \approx 5$ T. Several fractional conductance states are observable at higher overall conductances, which are also tunable with a magnetic field, e.g., a feature between $1.5\ e^2/h$ and $1.8\ e^2/h$. In many instances, there is significant overshoot (resulting in parameter regimes for which $dG/d\mu < 0$) before a plateau is reached.

Transconductance maps $dG/d\mu$, when plotted versus B and μ (Fig. 46B) provide additional insight into the transport characteristics of these serpentine superlattices. In the color scheme, bright green/yellow/red regions ($dG/d\mu > 0$) represent increases in conductance that generally correspond to introduction of new 1D subbands. Dark blue regions ($dG/d\mu \approx 0$) represent flat conductance plateaus, while purple regions ($dG/d\mu < 0$) correspond to regions of negative transconductance. One standout feature of the transconductance is a shifting of the lowest subband minima to a non-zero value of the magnetic field ($B = -7.4$ T and $B = 7.1$ T). In this range of magnetic fields, a large overshoot in the conductance is also observed, followed by a region of decreasing conductance. A second feature, observed in two ranges of magnetic field, is the existence of magnetic-field-tunable plateaus,
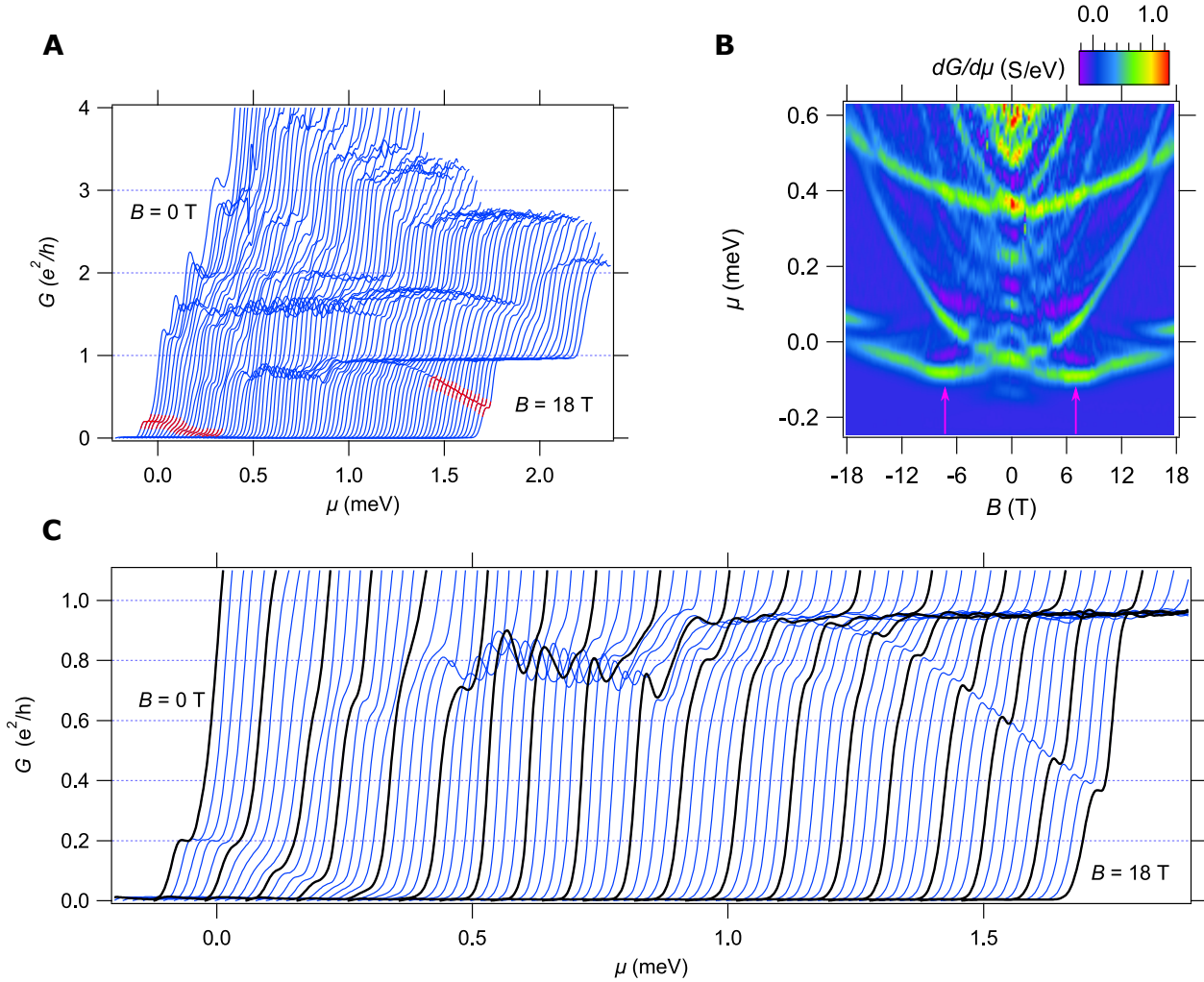
Figure 46: Magnetotransport for serpentine superlattice Device L1. **(A)** Conductance, G, plotted as a function of chemical potential μ and applied magnetic field B from 0 T (leftmost) to 18 T (rightmost). Curves are offset for clarity. Fractional conductance features below the 1 e^2/h plateau are highlighted in red. **(B)** Transconductance $dG/d\mu$ as a function of magnetic field B and chemical potential μ. Light (red/yellow/green) regions indicate increasing conductance, i.e. when new subbands become available. Dark blue regions indicate zero transconductance or conductance plateaus. Purple regions are regions of negative transconductance and indicate decreasing conductance. The minima of the lowest subband occurs at finite B field values, highlighted with pink arrows. **(C)** Zoom in of the fractional conductance features below the 1 e^2/h plateau. Curves at 1 T intervals are highlighted in black.

seen near zero magnetic field and in the range $12-18$ T as gaps in the lowest subband.

Qualitatively similar behavior is also observed for Device L2 (Fig. 49), which is created in a similar manner. Unlike Device L1, Device L2 shows excess conductance characteristic of superconductivity near zero magnetic field rather than a fractional conductance plateau (Fig. 50). The transconductance map (Fig. 49B) also shows some asymmetries in field which are due to slow temporal drifting of the chemical potential.

6.2.2   High magnetic field fractional conductance feature

6.2.2.1   Temperature dependence   Next the high magnetic field fractional conductance feature in Device L1 is examined as a function of temperature T and μ at $B = 18$ T (Fig. 47). At the lowest temperature ($T = 25$ mK) the fractional feature appears as a dip in the conductance at around 0.4 e^2/h. The dip flattens out with increasing temperature until it disappears at ~ 200 mK. The 1 e^2/h plateau however is smeared out at higher temperatures but persists up to 750 mK, the highest temperature that was measured. Fig. 47B shows the transconductance map $dG/d\mu$ as a function of μ and T. All temperatures reported were measured at the mixing chamber stage of the dilution refrigerator.

6.2.2.2   Finite-bias spectroscopy   We also studied the finite-bias spectroscopy of the fractional conductance feature $B = -18$ T. The conductance and transconductance maps as a function of four-terminal voltage V_{4t} and side gate voltage V_{sg} are shown in Fig. 48A and B, respectively. Linecuts of the conductance at zero bias and at a finite bias of $V_{4t} = 75$ μV are shown in Fig. 48C. The transconductance map shows a diamond structure characteristic of transport for ballistic systems [127, 128]. Large finite biases give rise to half-plateaus due to unevenly populated subbands. The diamond structure implies that the conductance features are not the result of energy-dependent transmission through the device. The value of the feature at zero bias is around 0.3 e^2/h and is reduced to approximately half that value at finite bias, 0.15 e^2/h.
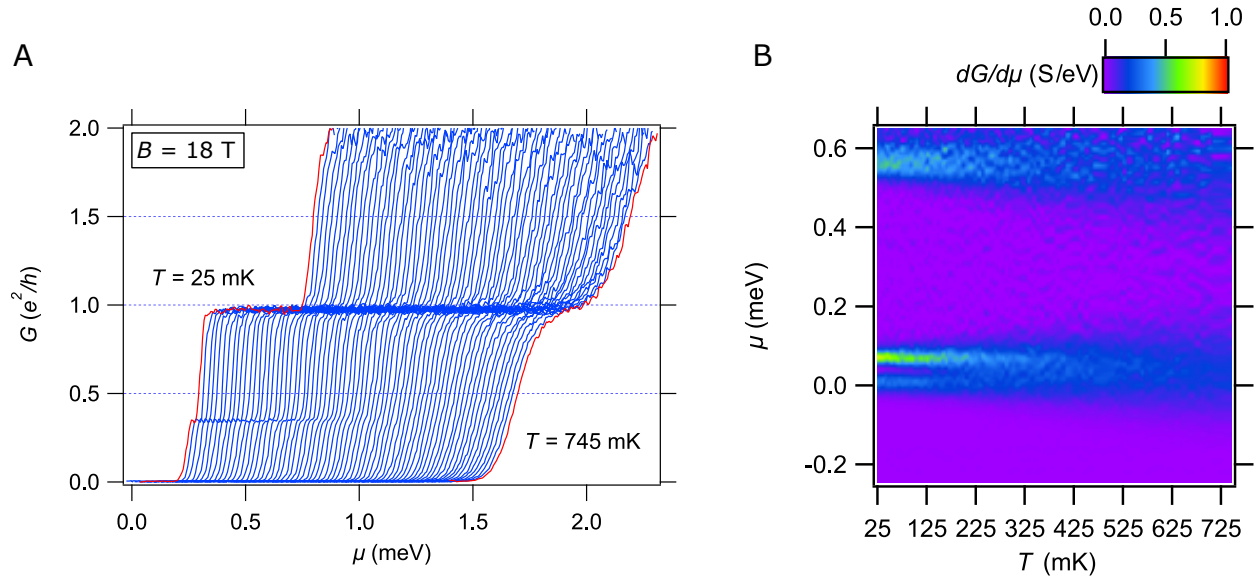
Figure 47: Temperature dependence of Device L1. **(A)** Conductance G as a function of chemical potential μ at $B = 18$ T for temperatures from $T = 745$ mK to 25 mK. Temperatures are measured at the mixing chamber of the dilution refrigerator. **(B)** Transconductance $dG/d\mu$ vs temperature T and chemical potential μ. The fractional conductance feature disappears at around 200 mK, while the 1 e^2/h conductance plateau is still visible at 745 mK, the highest measured temperature.
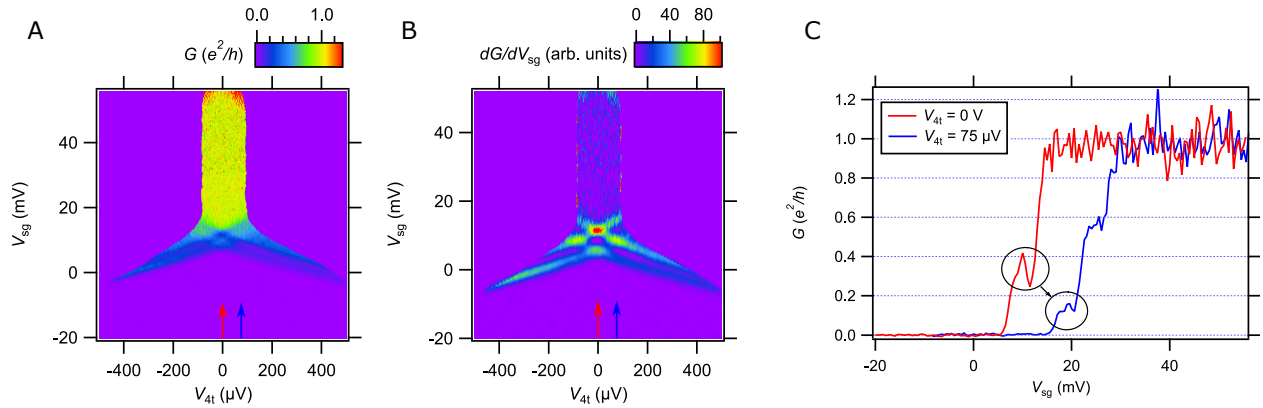
Figure 48: Finite-bias spectroscopy for Device L1. **(A)** Conductance map for Device L1 at $B = -18$ T as a function of 4-terminal voltage V_{4t} and side gate voltage V_{sg}. Conductance line-cuts at $V_{4t} = 0$ V and 75 µV are shown in **(C)**. **(B)** Transconductance map corresponding to panel (A). Red and blue arrows indicate locations of line cuts in (C). The transconductance maps shows the diamond feature characteristic of ballistic transport. Conductance linecuts show fractional conductance features below the 1 e^2/h plateau. At zero-bias the conductance feature appears at ~ 0.3 e^2/h and at finite-bias at around half that value ~ 0.15 e^2/h. Curves are offset for clarity. All data taken at $T = 25$ mK.

6.3 DISCUSSION

By perturbing the path of a ballistic electron waveguide, we find that it is possible to modify the spin-dependent subband structure in a manner that is consistent with an engineered spin-orbit interaction and results in the creation of new fractional conductance states. The origin of the spin-orbit interactions can be understood in a few different ways. The most naive explanation recognizes that the serpentine path of the electrons exposes propagating electrons, with momentum $\vec{k} = k\,\hat{x}$, to a spatially periodic alternating electric field, $\vec{E}_{\text{eff}}(x) = E_0\sin(k\,x)\hat{y}$, which, in the moving reference frame of the electrons, corresponds to an alternating effective magnetic field field $\vec{B}_{\text{SO}} \propto \vec{k} \times \vec{E}_{\text{eff}}$ that is aligned with the $\hat{z}$ axis. The resulting spin-orbit field is expected to cause a spin-dependent energy shift of the subband minima by $\pm|\vec{B}_{\text{SO}}|$, consistent with our experimental findings (Fig. 46B). A more sophisticated approach would take into account the fact that, in the basis of the unperturbed (straight) nanowire, the matrix elements that lead to hybridization with other lateral modes (highlighted in Fig. 45B) are significantly enhanced in the serpentine waveguide, and hence the magnitude of the Rashba spin-orbit interaction is correspondingly enhanced. Details of such a calculation are beyond the scope of this thesis, but are nevertheless important for describing numerically-accurate models of the engineered spin-orbit interactions.

The second main experimental observation concerns the fractional conductance plateaus which exist both in zero magnetic field as well as higher magnetic fields. In some cases the plateaus are preceded by conductance peaks. Fractional conductance states are typically an indication of strong electron-electron interactions. Well known examples are the fractional quantum hall effect [153], and the "0.7" anomaly which is commonly observed in quantum point contact devices [154] and which is attributed to strong interactions [155]. There have been theoretical predictions of fractional conductance states in clean 1D systems with few channels and strong (repulsive) electron-electron interactions [156, 157]. Oreg *et al.* [156] studied 1D wires with spin-orbit coupling and found that in wires with strong interactions and low densities, fractional quantized conductances were predicted. These fractional states arise due to correlated scattering processes from different channels that can lead to fractional conductance plateaus at various rational fractions. The underlying scattering process relies on

two ingredients: (1) multiple channels from which to scatter in the forward and reverse directions, and (2) strong electron-electron interactions that support these correlated exchange of momenta. The Shavit-Oreg theory [157] was recently compared to experiments from Kumar *et al.* [159], in which fractional conductance plateaus were observed in 1D GaAs-based quantum wires at similar fractional values to those observed here. While both the GaAs-based 1D wire and the $LaAlO_3/SrTiO_3$ nanowires are ballistic, the nature of the electron-electron interactions is fundamentally different for these two materials. That is to say, in GaAs it is repulsive, while in $LaAlO_3/SrTiO_3$ it is strongly attractive [119, 137, 83, 129]. The fact that such similar phenomena are identified in both systems is interesting and raises the question: to what extent can the $LaAlO_3/SrTiO_3$ system be modeled as a system with effectively repulsive interactions? It is known theoretically that there is a mapping between the repulsive-U and attractive-U Hubbard models [169]. Perhaps this mapping can be used to understand the attractive side of the phase diagram.

Quasi-1D superlattice devices with engineered properties may provide a building block for more complex quantum systems, for example, topological phases in coupled arrays of quantum wires [72, 170, 73]. It may also be possible to observe Majorana fermions in this system [171]. There are four ingredients needed to observe Majorana zero modes in nanowire systems: one-dimensional quantum wires, superconductivity, spin-orbit interactions, and a magnetic field [167, 168]. With the engineering of a spin-orbit interaction we may have the missing ingredient in $LaAlO_3/SrTiO_3$ nanowire devices. It is also worth emphasizing that these are real electronic materials and not just simulations, with engineerable properties that can be integrated with other materials or incorporated into real electronic devices.
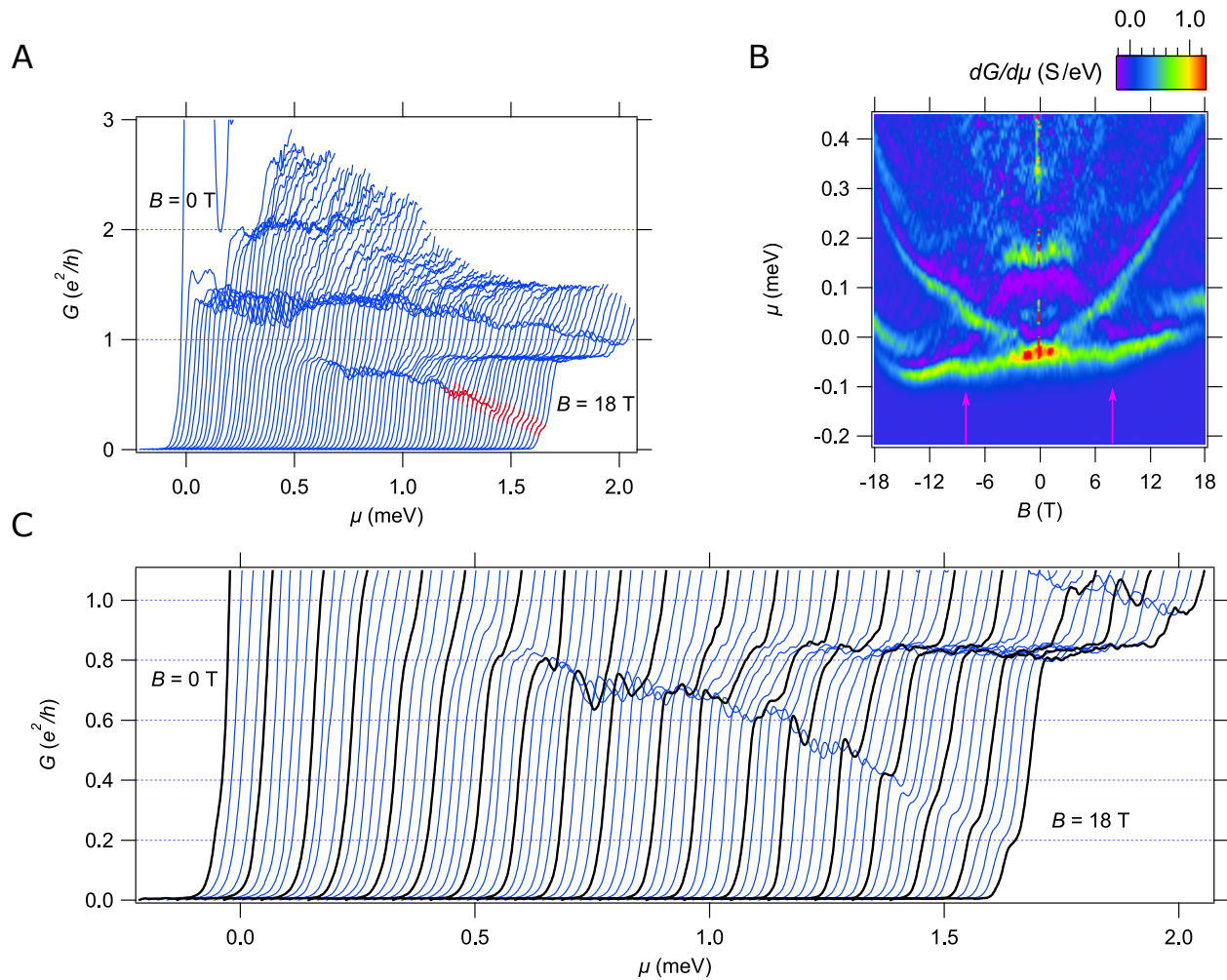
Figure 49: Magnetotransport for serpentine superlattice Device L2. **(A)**. Conductance G as a function of chemical potential μ for device L2. Curves are at different applied out-of-plane magnetic field values from 0 T to 18 T. A fractional conductance feature is observed below the 1 e^2/h plateau at high magnetic fields (highlighted in red). **(B)** Transconductance map as a function of magnetic field B and chemical potential μ. An overall drift while gating effects the subband structure of this device. **(C)** Zoom in of the high field fractional conductance feature. Curves at 1 T intervals are highlighted in black. All data taken at $T = 25$ mK.
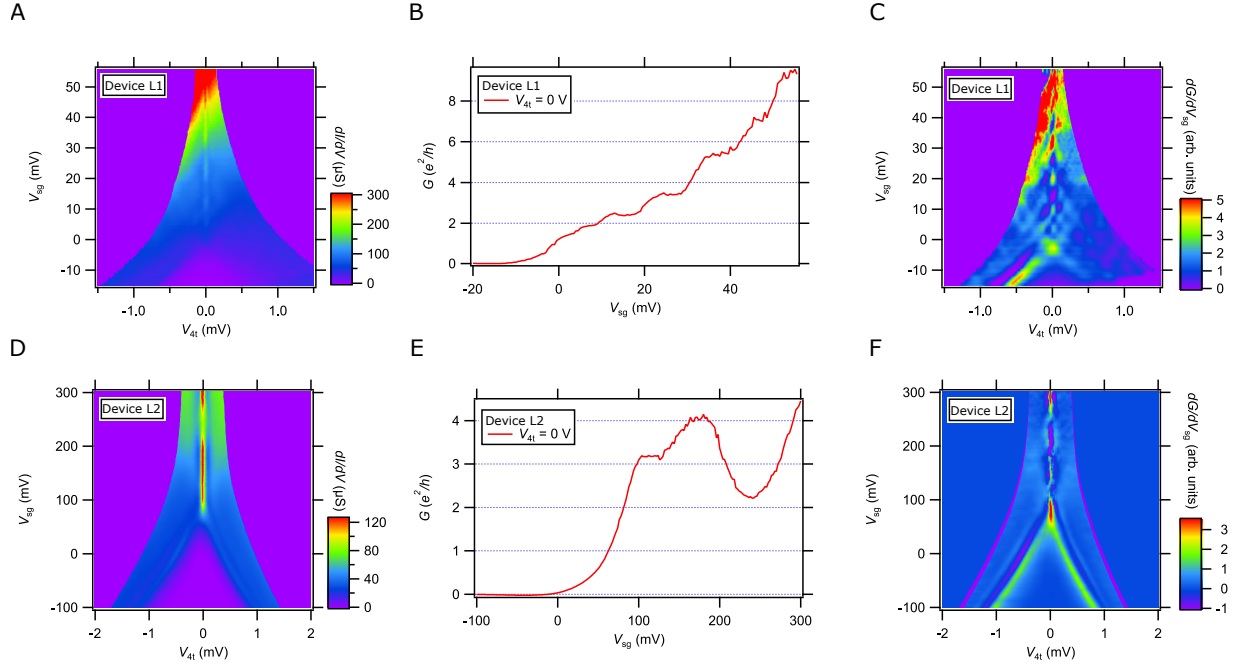
Figure 50: Finite-bias spectroscopy for Devices L1 and L2 **(A)** Conductance dI/dV as a function of four-terminal voltage V_{4t} and side gate voltage V_{sg} for Device L1 at $B = 0$ T. **(B)** Zero bias ($V_{4t} = 0$ V) conductance line cut of Device L1. **(C)** Transconductance map dG/dV_{sg} as a function of four-terminal voltage and side gate voltage. **(D)** Conductance dI/dV for Device L2. This device shows signatures of superconductivity near zero bias. **(E)** Conductance line-cut for Device L2. **(F)** Transconductance dG/dV_{sg} for Device L2. All data taken at $B = 0$ T and $T = 25$ mK.

7.0 Engineered chirality of one-dimensional LaAlO$_3$/SrTiO$_3$ nanowires

This chapter describes experiments studying 1D chiral superlattice devices at the LaAlO$_3$/SrTiO$_3$ interface. The devices were created by adding both vertical and lateral periodic modulation to electron waveguide devices. Transport measurements reveal oscillations in the conductance from an engineered axial spin-orbit coupling due to the 1D chiral superlattice structure.[1]

7.1 INTRODUCTION

Quantum transport in 1D geometries is fascinating in its own right, but it can also be regarded as a building-block for a variety of quantum devices. We have developed a flexible platform for creating 1D nanostructures at the LaAlO$_3$/SrTiO$_3$ interface using a conductive atomic force microscope lithography technique. Straight nanowire segments behave as electron waveguides with subband occupation that can be tuned with a gate and an external magnetic field. We can periodically perturb this waveguide, with 10 nm periodicity, in two ways. "Kronig-Penney" type modulation results in periodic vertical displacement of the electron waveguide, and sinusoidal lateral displacement of the nanowire can also be achieved. Combining the two perturbations in quadrature yields a chiral nanowire which exhibits striking oscillatory transmission as a function of both magnetic field and chemical potential. We discuss these results in terms of an engineered axial in-plane spin-orbit interaction within the spiral electron waveguide.

One of the most vexing mysteries in biology is the pervasiveness of chirality or handedness at the molecular level. The relationship between chirality and spin-polarized electron transport has been investigated for two decades, following pioneering work by Namaan and Waldeck [172] showing that chiral proteins and molecules exhibit the chiral-induced spin selectivity (CISS) effect. It has been postulated that molecular chirality produces an axial spin-

---

[1]This chapter is in preparation for submission to Nature Physics.

orbit interaction that locks the electron spin and momentum, inhibiting back scattering, and providing a rationale for the prevalence of chirality in life forms [173]. There have been numerous reports linking spin-polarized transport to molecular chirality. However, there are no measurements that directly probe the quantum nature of transmission through a single chiral molecule or nanostructure.

One approach to understanding electron transport in chiral quasi-one-dimensional (quasi-1D) structures is via experimental "quantum simulation" [1]. With this approach, a quantum system of interested is mapped onto a configurable quantum system whose parameters can be adjusted to match the system of interest. Ultracold atoms in optical lattices have been used to simulate a wide range of many-body Hamiltonians in two spatial dimensions [14, 174, 175, 27]. They have also been used to engineer gauge fields and spin-orbit interactions [163, 165], and have been used to create quantum point contacts and exhibit quantized transport [176]. Other solid-state approaches to 1D quantum simulation include transport studies in periodic superlattices, created using split gates in a GaAs/AlGaAs heterostructure [177, 178].

Here we describe experiments in which chiral quasi-1D nanostructures are "simulated" within LaAlO$_3$/SrTiO$_3$ heterostructures using conductive atomic force microscope (c-AFM) lithography [4, 5] (Fig. 51A). A positively biased AFM tip in contact with the LaAlO$_3$ locally switches the LaAlO$_3$/SrTiO$_3$ interface to a conductive state ("writes"), while a negatively biased AFM tip locally restores the insulating phase ("erases"). The writing (erasing) mechanism is attributed to local (de)protonation of the LaAlO$_3$ surface [87, 88]. The adsorbed protons create a potential landscape that defines conducting regions at the interface. The high spatial resolution of this technique (2 nm), combined with strong intrinsically attractive electron-electron interactions [119, 137, 129] make this system interesting as a platform for quantum simulation of a wide range of 1D and 2D nanostructures.

The chiral nanowires described below are derived from a well-characterized method for producing highly ballistic electron waveguides [83] which also exhibit strong electron pairing in the absence of superconductivity [119, 83], under applied magnetic fields that fall below a critical "pairing" field B_P. The conductance of these devices is quantized in units of e^2/h, where e is the electron charge and h is the Planck constant. The total conductance $G = N e^2/h$

represents ballistic transport from N occupied subbands (with distinct vertical, lateral, and spin degrees of freedom). For much of the phase diagram (parameterized by external plane-perpendicular magnetic field B and side-gate voltage V_{sg} or chemical potential $\mu = \alpha V_{\text{sg}}$), a single-particle description [83] qualitatively captures the observed transport behavior. But there are several parameter regimes where the single-particle model fails to capture the observed transport behavior. In particular, it is found that below a "pairing field" $|B| < B_{\text{p}}$, the ground state consists of electron pairs with corresponding conductance $2e^2/h$. Above this field, the electron pairs Zeeman split (and occasionally form re-entrant pairs and more complex structures [129].

Chiral nanowires are created through a combination of two different types of perturbation of the "straight" quantum wire. The first perturbation involves replacing a straight section of the nanowire with a shape that varies in space sinusoidally. The path for a horizontal sinusoidal waveguide is given by $y(x) = y_0 + y_k \sin(kx)$, where y_0, y_k and k are parameters that can be programmed. The second perturbation involves performing c-AFM lithography with a sinusoidally varying tip voltage: $V_{\text{tip}}(x) = V_0 + V_k \sin(kx + \phi)$. Combining these two perturbations with $\phi = \pm 90°$ (Fig. 51B) yields a chiral device structure. The expected impact of the two perturbations on the local electron density are: lateral disturbances of the wavefunction due to the horizontal motion of the first perturbation, while voltage modulations are expected to displace the wavefunction in the z direction. Together, a chiral shaped path of the electron is expected to result from these perturbations, with the helicity being controlled by the phase shift ϕ.

A schematic of device H1 is shown in Fig. 51C. The helical superlattice section of the device (right) is written with a sinusoidal modulation of the tip voltage ($V_0 = 10$ V, $V_k = 5$ V, $\phi = 90°$), and a lateral modulation amplitude ($y_k = 5$ nm, $2\pi/k = 10$ nm), with 34 total periods. The superlattice is surrounded by two straight segments written with $V_{\text{tip}} = 12$ V, in which highly transparent tunnel barriers [83] are created by applying negative voltage pulses $V_{\text{tip}} = -10$ V to the tip while writing. The left side of the device contains a "control" waveguide section that is straight and written with a constant tip voltage of $V_{\text{tip}} = 12$ V and bracketed by two highly transparent tunnel barriers, created with negative voltage pulses $V_{\text{tip}} = -10$ V. A side gate is also created using c-AFM lithography, (V_{sg}) which enables the chemical potential of both the

"chiral" and "control" device to be varied. The control and chiral waveguides can be independently characterized using four-terminal transport measurements, sharing only the small section between leads 3 and 4. The tip position and voltage while writing a helical superlattice device are shown in Fig. 15.

7.2   RESULTS

7.2.1   Magnetotransport data

The 4-terminal conductance of 1D superlattice Device H1 as a function of the chemical potential μ, for magnetic fields ranging between 0 T and -18 T is shown in Fig. 52A. Chemical potential values are calculated by finding the lever arm to convert applied side gate voltage to chemical potential [83]. Positive and negative magnetic field sweeps show similar transport. Each curve is taken at a different applied magnetic field B from $B = 0$ T on the left to $B = -18$ T on the right, with curves at 1 T intervals highlighted in black. The curves are offset for clarity. Conductance curves show plateaus at values close to quantized values $G = 2 \ e^2/h$ and $G = 4 \ e^2/h$ up to $B = -18$ T. At low values of magnetic field the $2 \ e^2/h$ plateau is not visible, but there is a feature close to $4 \ e^2/h$. Fig. 52B shows the transconductance $dG/d\mu$ for the superlattice device. The transconductance is calculated by numerical differentiation of the conductance curves in Fig. 52A. The bright red/yellow regions correspond to increases in conductance, when new subbands become occupied. The blue regions correspond to conductance plateaus. The purple regions correspond to decreases in conductance. This transconductance map reveals oscillations/interference patterns in the conductance, purple bands in the region above the lowest subband. These oscillations are at an angle, indicating that they depend both on the strength of the magnetic field and on the chemical potential (energy of electrons in the device). Line cuts of the transconductance and conductance highlighting these oscillations are shown in Fig. 53B and Fig. 53C. Vertical conductance line cuts show that the conductance initially rises above $G = 2 \ e^2/h$ then falls back down to $\sim 2 \ e^2/h$. The number of oscillations increase as the magnetic field is increased. Fig. 53C at $B = 5$ T shows one oscillation which

110
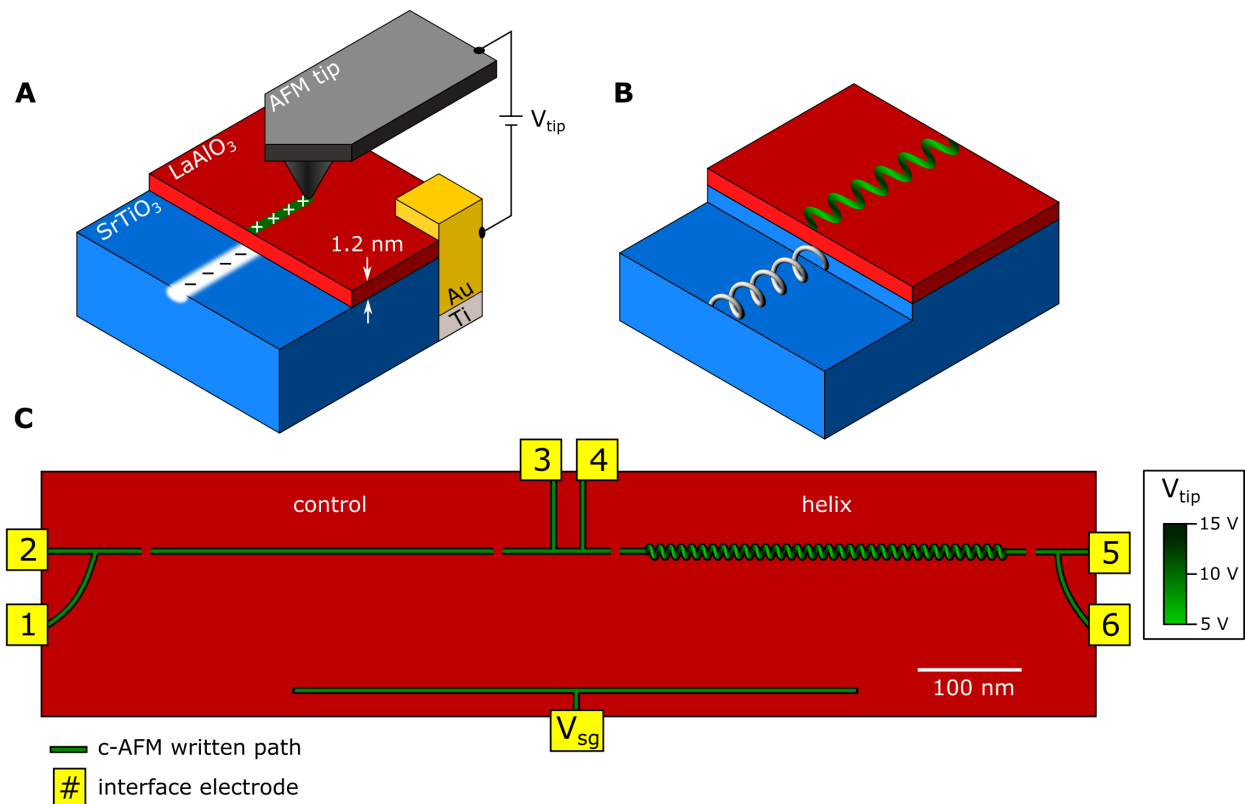
Figure 51: Chiral superlattice device schematic. **(A)** Conductive atomic force microscope (c-AFM) lithography is used to create conducting channels at the $LaAlO_3/SrTiO_3$ interface. **(B)** Schematic of a chiral nanowire at the $LaAlO_3/SrTiO_3$ interface. Vertical and lateral modulations of the tip voltage and tip position respectively creates a helical nanowire at the interface. **(C)** Schematic of Device H1. The device has two sections: a control waveguide (left) and helical superlattice (right). Each section of the device can be probed independently with a 4-terminal measurement, sourcing current through only the section of interest and measuring the voltage drop across that section. Both sections are bracketed by two highly transparent tunnel barriers

increases to 2 oscillations at $B = 6$ T. The magnitude of the oscillations become suppressed at high magnetic field values, but they are still faintly visible, and even at $B = -18$ T the conductance still overshoots then decreases back down to 2 e^2/h. The number of oscillations also increases with increasing values of μ shown in the horizontal line cuts of the transconductance map in Fig. 53B.

Fig. 52C,D shows the conductance and transconductance data from the adjacent control electron waveguide section of Device H1. There are a number of differences between the superlattice and the control waveguide sections of Device H1. There are no oscillations observed in the control device, there is no overshoot and then suppression of the conductance, it is always rising with increasing gate and B field values. It also shows a pairing field, where the lowest subband spin splits, and goes from a conductance step of $G = 2$ e^2/h to steps of 1 e^2/h, at around $B = 8$ T. At low magnetic field values there are steps/features visible at 2 and 4 e^2/h (different than the superlattice which initially shows features only at 4 e^2/h).

7.2.2 Finite-bias spectroscopy

Finite bias spectroscopy for the superlattice section of Device H1 is shown in Fig. 54. Fig. 54A shows the conductance map as a function of V_{4T} and side gate V_{sg} at $B = 0$ T and the corresponding superconducting peak in the conductance. Fig. 54B shows an I-V curve for the helical superlattice section with a superconducting critical current of around 10 nA. I-V curves for the control device do not show a similar superconducting feature. Fig. 54D,F show the conductance and transconductance of the helical superlattice section at $B = 8$ T. The transconductance map reveals characteristic diamonds [127, 128] which indicate that the transport in the device is ballistic. The finite bias spectroscopy is used to find the lever arm of both sections of the device and calculate the chemical potential.

7.2.3 1D superlattice device H2

Data from Device H2 is shown in Fig. 55. This device was written with the same lateral modulation parameters, but the vertical modulation was first written with a constant tip voltage $V_{tip} = 10$ V, then the same path was written modulating the voltage $V_{tip} = \pm 2.5$ V. This
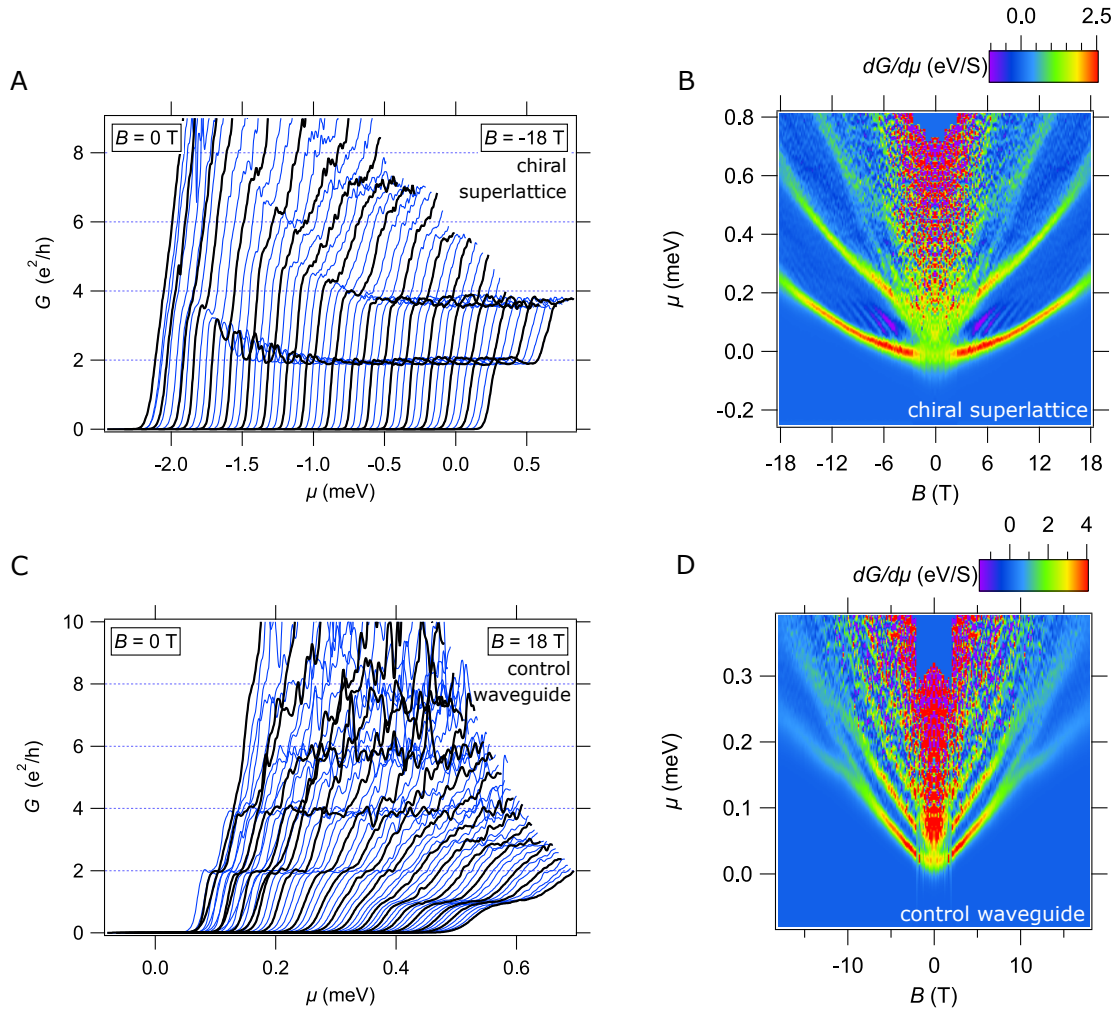
Figure 52: Device H1 transport data. **(A)** Conductance data for the helical superlattice section of Device H1. Conductance G vs chemical potential μ, each curve is at a different applied magnetic field from $B = 0$ T to $B = -18$ T. Curves at 1 T intervals are highlighted in black. Curves are offset for clarity. **(B)** Transconductance $dG/d\mu$ as a function of magnetic field B and chemical potential μ. Bright (red/yellow/green) regions indicate increases in the conductance when new subbands become occupied. Light blue regions are zero transconductance and indicate conductance plateaus. Dark regions (purple/dark blue) are negative transconductance and indicate decreases in conductance. **(C)** Conductance data for the control waveguide section of the device. **(D)** Transconductance map of the control section of the waveguide. Data taken at $T = 25$ mK.
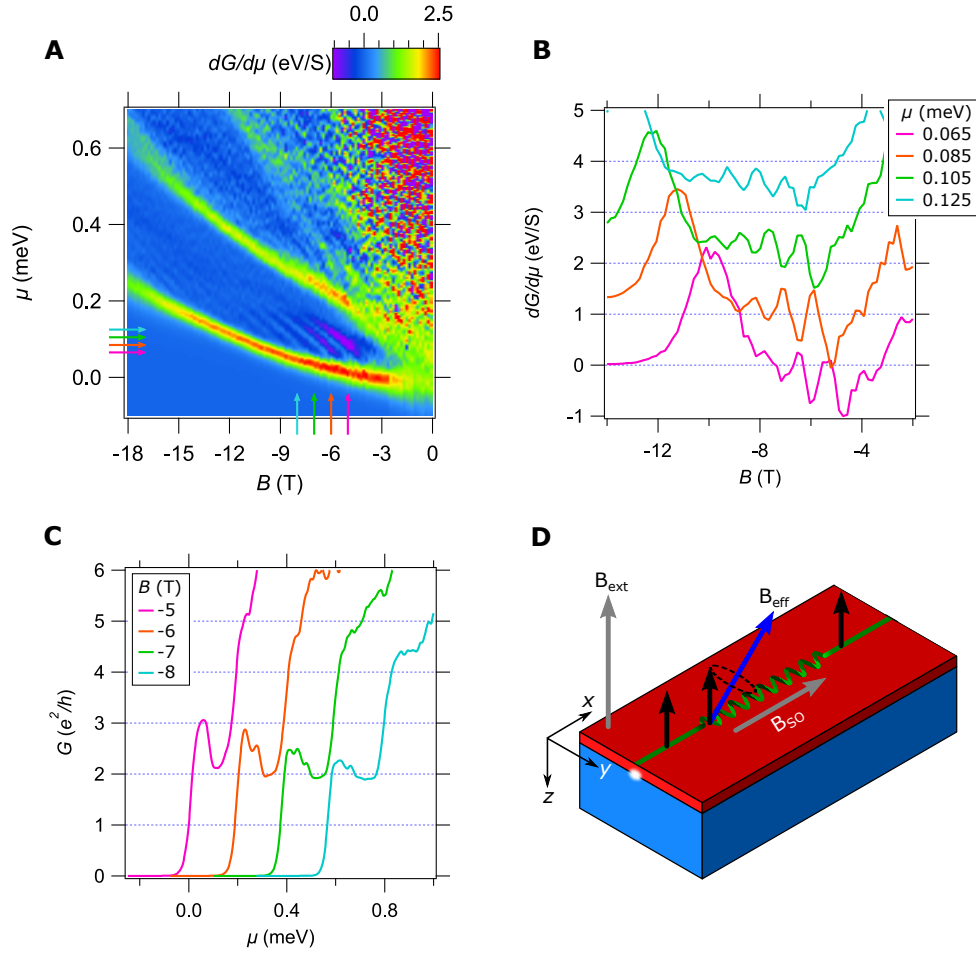
Figure 53: Line cuts showing oscillations in Device H1. **(A)** Transconductance $dG/d\mu$ showing oscillations in the region of the $2\,e^2/h$ plateau, the region between the lowest subband and the next subband (bright red and yellow regions). **(B)** Horizontal line cuts of the transconductance data as a function of magnetic field B. Each curve is taken at increasing values of chemical potential μ, curves are offset for clarity. **(C)** Vertical line cuts showing conductance values as a function of μ at different magnetic field values. **(D)** Schematic of how the helical superlattice device effects the electrons in the device. The applied external field and engineered spin orbit field from the superlattice create a new effective field inside the superlattice. When spins, polarized in the z direction, enter the superlattice portion of the device they precess around the new effective field. If they don't make a full precession by the time they exit the superlattice the conductance will be suppressed giving rise to the oscillations.
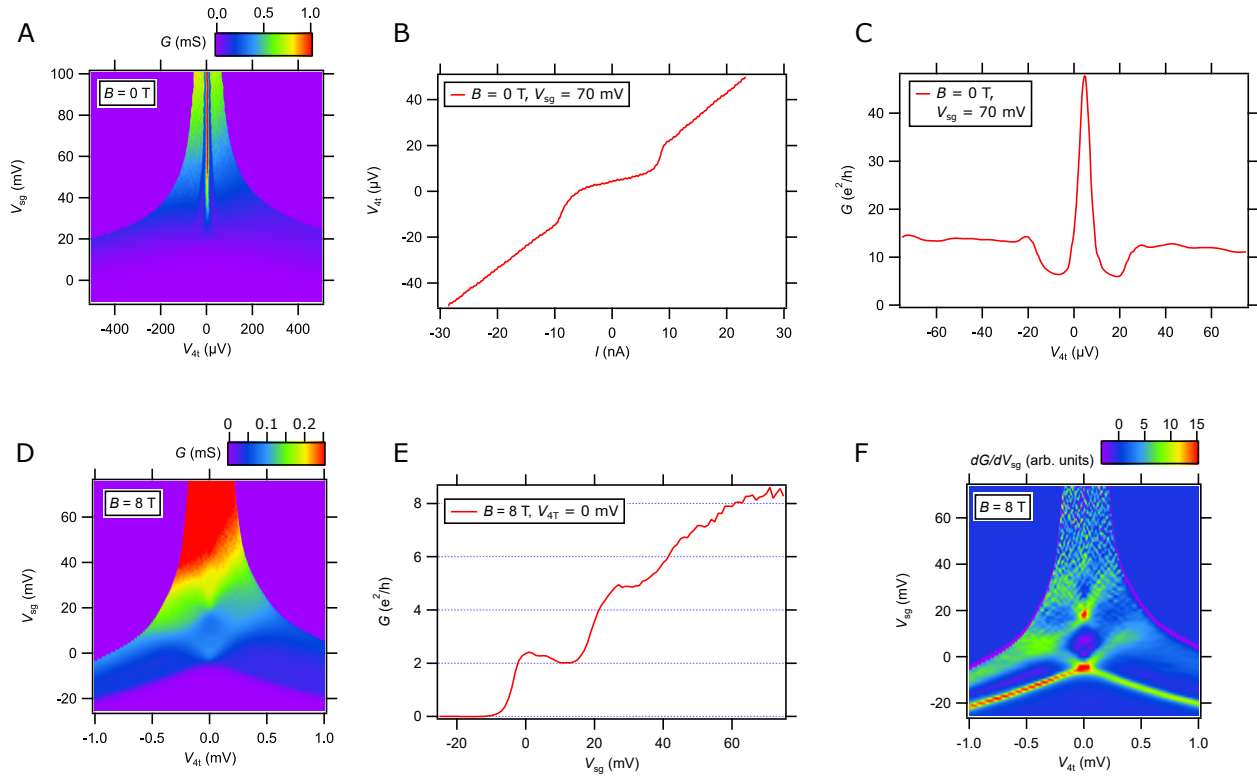
Figure 54: Finite bias spectroscopy for the chiral superlattice section of Device H1. (A) IV curve spectroscopy for Device H1 at $B = 0$ T. (B) 4-terminal voltage as a function of current for the helical superlattice section at $B = 0$ T and $V_{sg} = 70$ mV showing the superconducting state with a critical current of around 10 nA. (C) Horizontal linecut of the conductance map in (A) at $V_{sg} = 70$ mV showing the peak in conductance corresponding to the superconducting state. (D) IV curve spectroscopy at $B = 8$ T. (E) Vertical line cut at zero bias showing the conductance steps. (F) Transconductance showing characteristic diamond structure of ballistic transport through the superlattice device.

writing process is similar to how the electron waveguide devices are created. This device also shows oscillations in conductance above the $G = 2 \, e^2/h$ plateau (Fig. 55D). Additionally there are some periodic features in the lowest subband which are visible in Fig. 55C. In the conductance these features are due to a periodic change in the slope of the conductance jump from an insulating state to the $2 \, e^2/h$ plateau. The features in device H2 are qualitatively similar; the amplitude of the oscillations decreases and the number of oscillations increases at higher magnetic fields. There is also a high conductance feature at low B fields.

We have observed qualitatively similar oscillations in conductance in several helical devices, though not all helical superlattice devices show these types of oscillations. Devices with only lateral or vertical modulations or unmodulated control electron waveguide devices do not show the oscillations, over 50 superlattice devices were studied.

7.3 DISCUSSION

The helical motion of electrons in chiral materials (like DNA) is predicted to produce an axial magnetic field B_{SO} [173]. Fig. 53D shows a schematic of how this engineered axial spin-orbit magnetic field can produce oscillations in the transport through a helical superlattice device. The engineered axial magnetic field in the x direction and the applied external magnetic field in the z direction will produce an effective magnetic field in the superlattice. Electrons in the straight portion of the device will be spin polarized in the direction of the applied magnetic field. As they enter the superlattice they will begin to precess around the new quantization axis of the effective B field. If they do not make a complete number of precessions by the time they exit the superlattice the conductance will be suppressed, leading to the observed oscillations. The precession will depend on the orientation of the effective field, which changes with the strength of the applied B field, and also the energy of the electrons (how quickly they move through the superlattice), which changes with the chemical potential. The oscillations appear on top of a base conductance of $G = 2 \, e^2/h$, these paired electrons are a spin singlet, and won't be effected by this spin-orbit field. Observation of $4 \, e^2/h$ feature at low B fields in the superlattice devices is another possible indication of an engineered spin-orbit interaction.

116
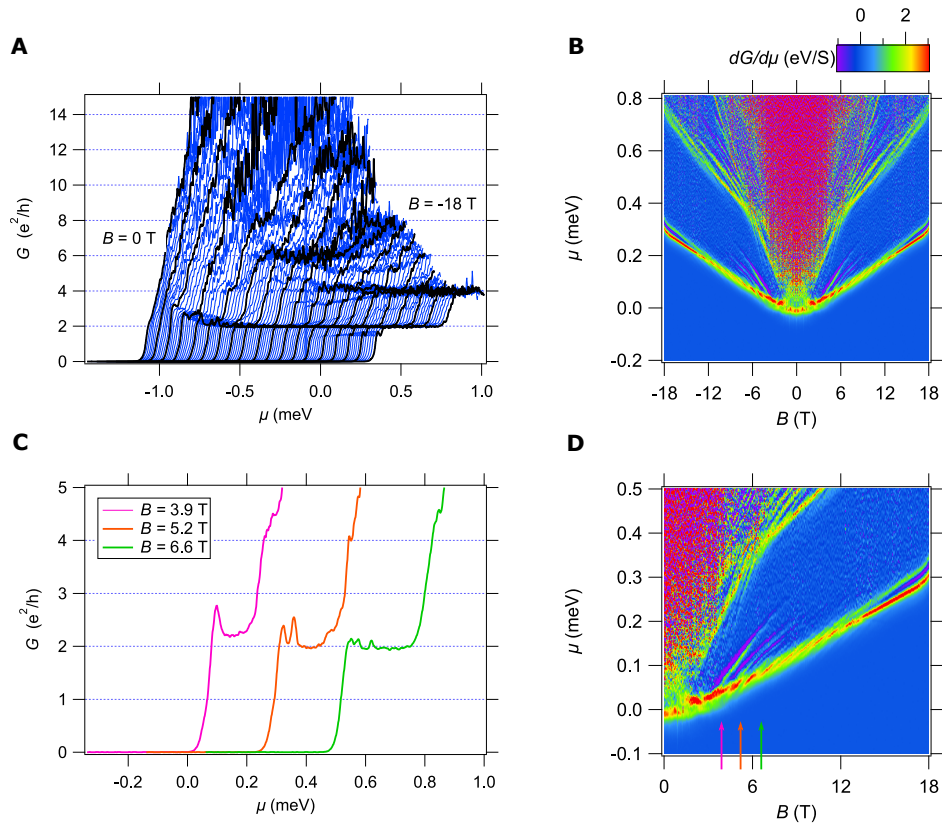
Figure 55: Magnetotransport data from helical superlattice Device H2. **(A)** Conductance data as a function of μ, curves are at different magnetic field values from $B = 0$ T to $B = -18$ T, curves are offset for clarity. The value of the first conductance plateau is at $G = 2\ e^2/h$ up to high magnetic field values, although there is a feature that appears at around $B = 15$ T. **(B)** Transconductance $dG/d\mu$ as a function of magnetic field B and chemical potential μ. Data is symmetrized. **(C)** Conductance line cuts at three magnetic field values showing the oscillations with a base conductance values of $G = 2\ e^2/h$. The number of oscillations increases with increasing B field. **(D)** Zoom in of the transconductance showing the oscillations and the lowest subband. Oscillations also appear in the lowest subband, where the conductance is increasing (bright regions) as well as on the plateau (dark regions).

The superlattice section of the device also exhibits a stronger pairing field than the control electron waveguide section. The pairing field in the superlattice is enhanced to $B = 18$ T, the highest applied magnetic field, while the adjacent control section has a pairing field of $B \sim 8$ T. The mechanism for the pairing seen in electron waveguide devices is unknown but several of the periodic modulations discussed here have shown an enhanced pairing effect in superlattice devices.

We have demonstrated the use c-AFM lithography to create chiral 1D superlattices at the $LaAlO_3/SrTiO_3$ interface by adding a periodic modulation to an electron waveguide device. This 1D superlattice appears to engineer an axial spin-orbit interaction in the nanowire which causes oscillations in the conductance that are dependent on both the external applied magnetic field and the applied side gate voltage, or energy, of the device. This is a first step towards developing a quantum simulation platform using this oxide heterostructure system which is configurable on the nanoscale and has exhibited strongly correlated phases. The advantage of this system a quantum simulation platform is that these are real electronic devices that can be incorporated (along with their engineered properties) into other systems. They also naturally support some of the interesting many body physics being studied using quantum simulation. The challenges are that the Hamiltonian of the system is not precisely understood (as it is with cold atoms in optical lattices). But it is the hope that the results of these experiments can be compared with effective 1D model Hamiltonians to bridge experiment and theory and enable quantum simulation of more complex systems.

8.0 Conclusions

The experiments presented in this thesis represent the first steps toward developing a solid state quantum simulation platform using the complex oxide heterostructure $LaAlO_3/SrTiO_3$. This material is configurable on the nanoscale and hosts both superconductivity and strong, tunable electron-electron interactions, making it a very promising platform for both engineering and simulating quantum systems. Future work will involve expanding on the 1D superlattice devices presented here. For example, the flexibility of the c-AFM lithography technique will enable the creation of 1D superlattices geometries that are different than the lateral, vertical, and chiral devices presented here. By engineering spin-orbit coupling in one dimension it may be possible to observe Majorana fermions in $LaAlO_3/SrTiO_3$ nanowire devices. Further study of 1D superlattices in rotated magnetic fields and using low temperature scanning probe microscopy will help shed light on the engineered properties of these devices. 2-dimensional (2D) devices, composed of 2D lattices or arrays of 1D nanowires, could also be created.

The straight waveguide devices discussed in Chapters 3 and 4 are highly reproducible. The superlattice devices presented in Chapters 5-7, however, show many qualitatively similar features but it has been difficult to create the same features from device to device. Reproducibility will need to be improved in order to develop the tools needed to engineer properties on demand. One approach to device reproducibility is to better understand the role ferroelastic domain walls play in the transport properties. The effect of ferroelastic domains on 1D devices at the $LaAlO_3/SrTiO_3$ interface is an area of current research that may have a large impact on 1D superlattice reproducibility. Thermal cycling of $LaAlO_3/SrTiO_3$ samples has shown that the ferroelastic domain formation can vary greatly [61]. It has become increasing apparent that the formation of ferroelastic domains plays a large role in the 1D transport at the $LaAlO_3/SrTiO_3$ interface [64, 179].

Patterning conducting nanowires using c-AFM lithography may offer a method to seed the formation of the ferroelastic domains along defined directions [89]. The geometry of the 1D nanostructures may also help to pin the ferroelastic domains, as shown in nanoscale Hall crosses [179]. Further evidence of domain wall seeding and pinning is shown in "zigzag"
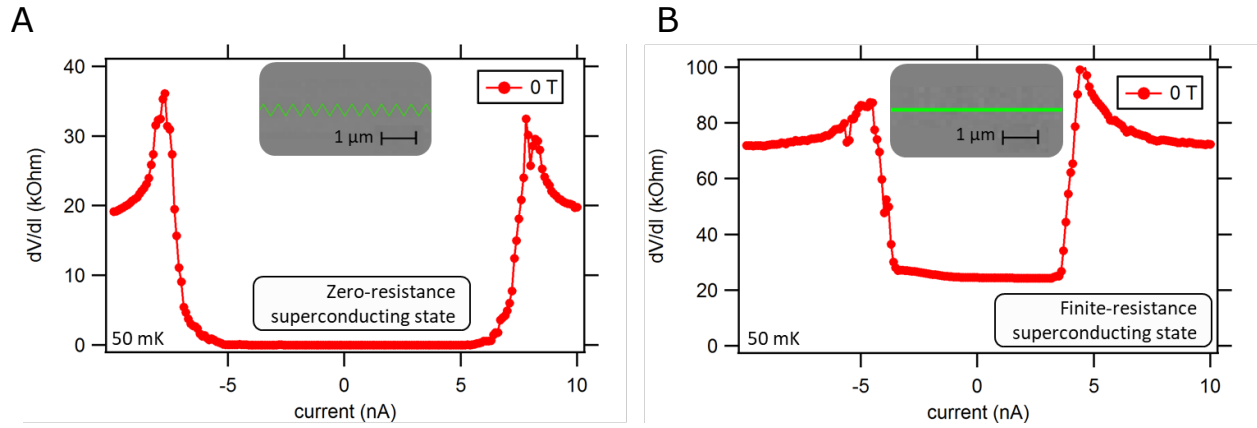
Figure 56: Enhanced superconductivity in zigzag nanowire devices. **(A)** dI/dV for a zigzag shaped nanowire showing a zero resistance superconducting state. **(B)** dI/dV for a straight nanowire section showing a weaker superconducting state with a finite resistance. $T = 50$ mK and $B = 0$ T for both curves.

shaped nanowire devices, which have been found to have enhanced superconductivity when compared to straight nanowires. As shown in Fig. 56A, the superconducting state in a zigzag wire has a lower resistance and a larger critical current than the superconducting state in a straight nanowire (Fig. 56B). Superconductivity was found to exist at the domain boundaries (which form along crystallographic axes) [64], and zigzag shaped nanowire devices could facilitate the formation of more well-defined domain walls. The ability to reliably control the location of domain boundaries, using c-AFM lithography or other methods, could have a great impact on the reproducibility of transport in 1D devices at the interface.

Appendix A Instrumentation

A.1   ATOMIC FORCE MICROSCOPES

Atomic force microscopes are an integral part of the experiments discussed in this thesis. They are used extensively to image prepare and image the $LaAlO_3/SrTiO_3$ surface and to write nanostructures at the interface.

The atomic force microscope (AFM) is used to image surfaces with atomic resolution by detecting the tip-sample forces. The AFM was first invented by Binnig *et. al.* in 1986 [180]. The basic principle is to detect the deformation of a spring to measure the atomic forces between the spring and a sample. In most cases the spring is in the form of a cantilever which has a diving board geometry. Attached to the cantilever is an atomically sharp tip which can have a radius of curvature < 10 nm. As the tip approaches the surface of a sample forces between the tip and the surface cause the cantilever to bend. Attractive force between the tip and surface causes the cantilever to bend towards the surface, then as it gets closer repulsive forces cause it to bend away from surface. The deflection of the cantilever is typically measured by shining laser light onto the top surface of the cantilever which is reflected into a position sensitive photodiode (Fig. 57). To monitor the topography of a sample a Z axis piezo is moved to maintain a constant deflection of the cantilever, or a constant distance between the tip and the sample. The tip is raster scanned across the surface with X and Y axis piezos. The movement of the Z piezo to maintain a constant distance gives the topography information about the sample. A schematic of the AFM used in these experiments, an Asylum MFP-3D, is shown in Fig. 58. The precise movement of the sample in the X-Y direction and the cantilever assembly in the Z direction are monitored by three linear variable differential transformers (LVDT) which are position sensing devices. They are necessary because distances cannot be directly calculated using the voltage applied to the piezos due to hysteresis and non-linearity [181].

The operation of the AFM described above is referred to as "contact mode", the tip is kept in contact with the sample. There is another mode of operation called ac mode. Here the cantilever is oscillated close to it's resonant frequency, as it approaches a sample the van der
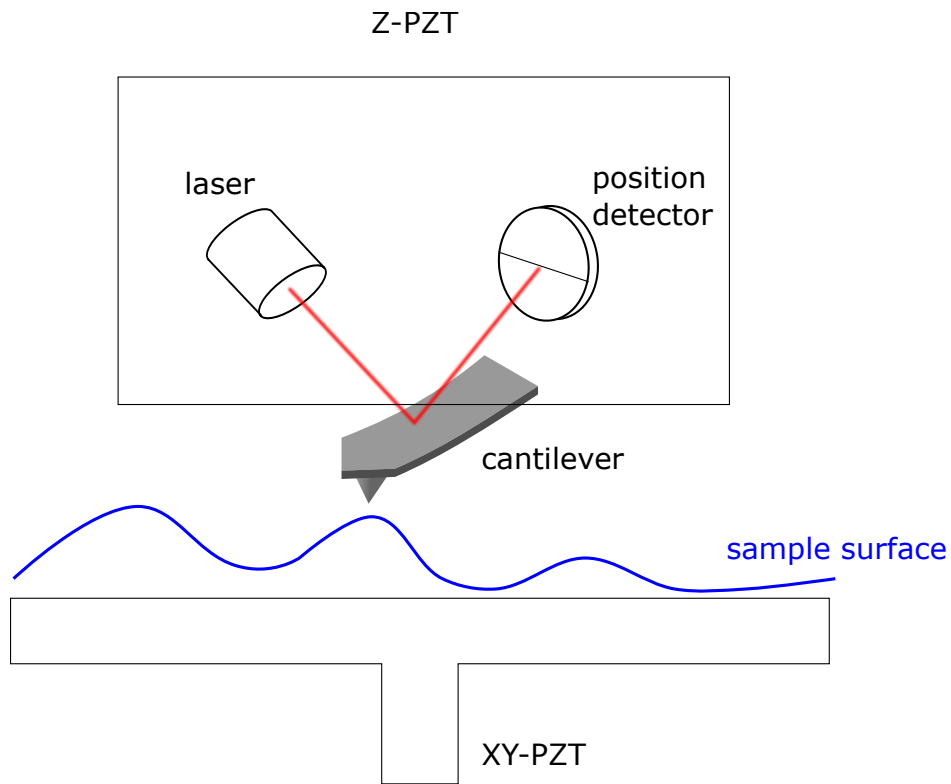
Figure 57: Schematic of atomic force microscope (AFM) operation. The cantilever acts as a spring to measure the atomic forces between the sample and the tip on the end of the cantilever. As the cantilever approaches the sample it will deflect due to these forces. A light source is bounced off a cantilever into a position sensitive photodiode to monitor the deflection of the cantilever. The Z-PZT is a piezo that moves the cantilever in the Z direction. By moving the cantilever to keep the deflection constant and scanning over the sample using the XY piezo stage, the topography of the sample can be imaged.

MFP-3D AFM
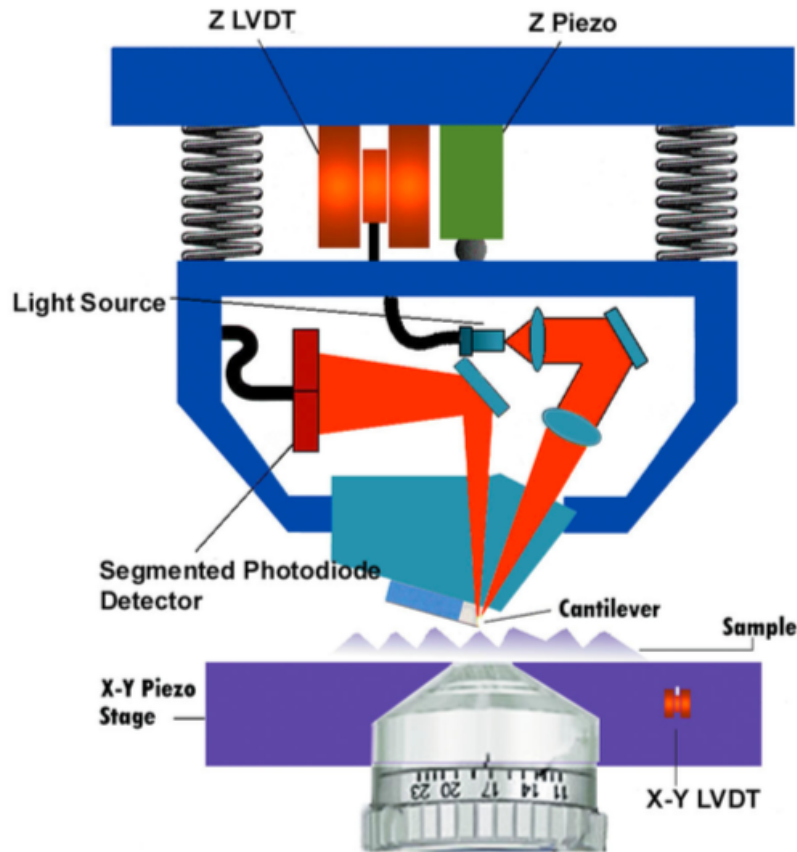
Figure 58: Schematic of the Asylum MFP-3D AFM used in these experiments. A light source is bounced off a cantilever into a position sensitive photodiode which measures the deflection of the cantilever due to the atomic forces between the tip and the sample. The Z piezo moves the cantilever assembly to maintain a constant deflection, or distance, between the tip and the sample. This distance is measured using the Z LVDT (linear variable differential transformer). The X-Y piezo stage moves the sample to scan the tip over the sample and measures the topography, or other properties of the sample. Adapted from Ref. [181].
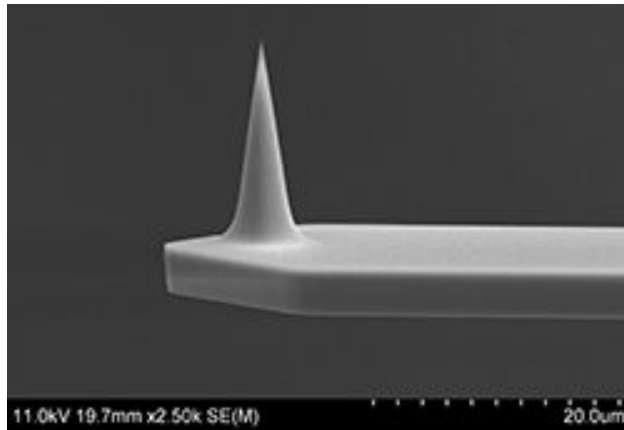
Figure 59: Typical AFM tip used in these experiments. Aspire CFM AFM tip made from highly doped, n-type, single crystal silicon. Tips have a typical radius of curvature of 8 nm, and a force constant of 3 N/m [182].

Waals forces will change the oscillation of the cantilever. By monitoring the oscillations and keeping them at a constant value the tip is kept at a constant distance from the sample and the topography can be determined. AC mode is ideal for soft samples when the tip may damage the sample.

Typical AFM tips used in these experiments are shown in Fig. 59. The tips are made of doped Si and have a radius of curvature of 8 nm and force constant of $\sim$ 3 N/m. Some devices were written with PtSi tips which have a larger radius of curvature ($\sim$ 25 nm), but are more wear resistant, so that the same tip could be used to write several samples. No significant differences were noted between devices written with different tips.

A.2 LOW TEMPERATURE MEASUREMENTS

A.2.1 Dilution refrigerators

Dilution refrigerators use a mixture of ^{3}He and ^{4}He isotopes to cool to temperatures on the order of several mK [183]. Cooling is achieved by using the enthalphy of mixing of the two helium isotopes. At low enough temperatures the ^{3}He-^{4}He mixture will separate into ^{3}He-rich (concentrated) and a ^{4}He-rich (dilute) phases. The phase diagram of liquid ^{3}He-^{4}He mixtures as a function of ^{3}He concentration and temperature is shown in Fig. 60. The shaded region shows where the mixture will separate into ^{3}He-rich and ^{4}He-rich phases. The less-dense ^{3}He-rich phase will float on top of the ^{4}He-rich phase. The enthalpy of ^{3}He in the dilute phase is larger than the enthalpy of ^{3}He in the concentrated phase so the migration of ^{3}He atoms from the concentrated to the dilute phase results in cooling.

As the temperature approaches zero, the ^{3}He-rich phase becomes pure ^{3}He, but the ^{4}He-rich phase reaches a constant concentration of 6.6% ^{3}He at $T = 0$ K. The reason for this finite concentration has to do with the binding energy of the ^{3}He atom in each of the phases.

The binding energy of a single ^{3}He atom in liquid ^{4}He is larger than that of one in liquid ^{3}He. Both isotopes have the same van der Waals forces, but the ^{3}He atom has a larger zero-point motion than the ^{4}He atom (due to its smaller mass). So in a ^{4}He liquid the atoms are closer together, than in a ^{3}He liquid phase, and a ^{3}He atom will have a larger binding energy in liquid ^{4}He because of the smaller distance between the atoms. This means that a ^{3}He atom at the phase boundary will migrate into the ^{4}He-rich phase.

When more ^{3}He atoms are added, increasing the concentration in the dilute phase, there are two competing forces that effect the binding energy. First, there is an attraction between the ^{3}He atoms due to their larger zero-point motion. Because there is more space around them the liquid is more dilute which will attract another ^{3}He atom which prefers more space around it than the ^{4}He atoms have due to their smaller zero-point motion. So as the concentration increases so does the binding energy. This is countered by the face that ^{3}He is a Fermi liquid and must obey the Pauli exclusion principle, additional ^{3}He atoms must go into increasingly higher energy states and this decreases the binding energy with increasing con-
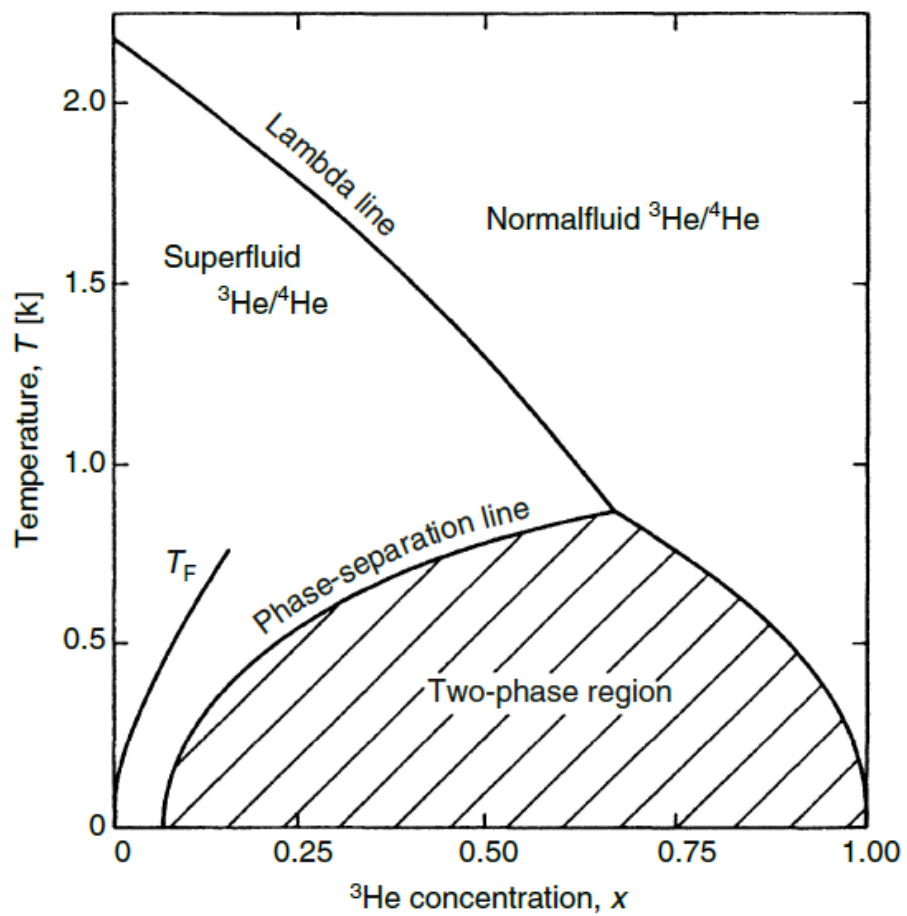
Figure 60: Phase diagram of liquid ^{3}He-^{4}He mixtures. Inside the two-phase region the mixture will separate into ^{3}He rich and ^{3}He poor phases. Adapted from Ref. [183].

centration. These two effects reach an equilibrium in the dilute phase at a concentration of 6.6% ^{3}He.

The dilution refrigerator cools by continuously removing ^{3}He from the dilute phase which will cause ^{3}He from the concentrated phase to migrate across the phase boundary to maintain the concentration at 6.6%. The migration across the phase boundary results in cooling.

A schematic of the dilution unit is shown in Fig. 61. The ^{3}He-^{4}He mixture is continuously circulated in a closed loop. It enters the dilution unit after having been cooled to $\sim$ 1.5 K. It goes through an impedance, which will reduce the pressure of the mixture and ensure that it condenses at 1.5 K and remains in a liquid state. The mixture then passes through a heat exchanger which is in contact with the still at $\sim$ 0.7 K. It passes through a secondary flow impedance to again reduce the pressure and ensure the mixture remains in a liquid state. Next are a series of heat exchangers that are thermally connected to ^{3}He leaving the mixing chamber. It will then enter the concentrated phase of the mixing chamber. ^{3}He migrates across the phase boundary into the dilute phase providing cooling to the mixing chamber, then leaves through a larger tube at the bottom due to the osmotic pressure created by pumping on the still and removing ^{3}He. It flows through the heat exchangers providing cooling to the incoming mixture, and enters the still. The still is kept at a temperature of $\sim$ 0.7 K, where the vapor pressure of ^{3}He is much larger than ^{4}He, so that pumping on the still will remove mostly ^{3}He. The removed ^{3}He is then circulated back into the dilution unit, ideally only ^{3}He is circulated.

If a portion of the circulating gas is ^{4}He it will reduce the cooling power of the cryostat. Circulating ^{4}He means that there is a reduced flow of the ^{3}He, due to the finite flow rate of the pumps in the system, which reduces cooling. It also increases the heat load on the heat exchangers since the specific heat of a ^{3}He-^{4}He mixture is higher than that of pure ^{3}He.

The dilution refrigerator is composed of stages with decreasing temperature. Each stage is used to progressively cool the incoming ^{3}He-^{4}He mixture and the wiring and electronics that are used to do experiments. The 4 K stage is cooled by contact with a liquid ^{4}He bath in the case of a wet fridge, or by a pulse tube compressor in a 'dry' fridge. A pulsed tube compressor uses a closed-loop helium expansion cycle where adiabatic expansion of compressed helium is used to cool to cryogenic temperatures. The next stage in a wet system is the 1 K pot. The 1 K pot uses helium from the bath which is sipped into the 1 K pot through an impedance,
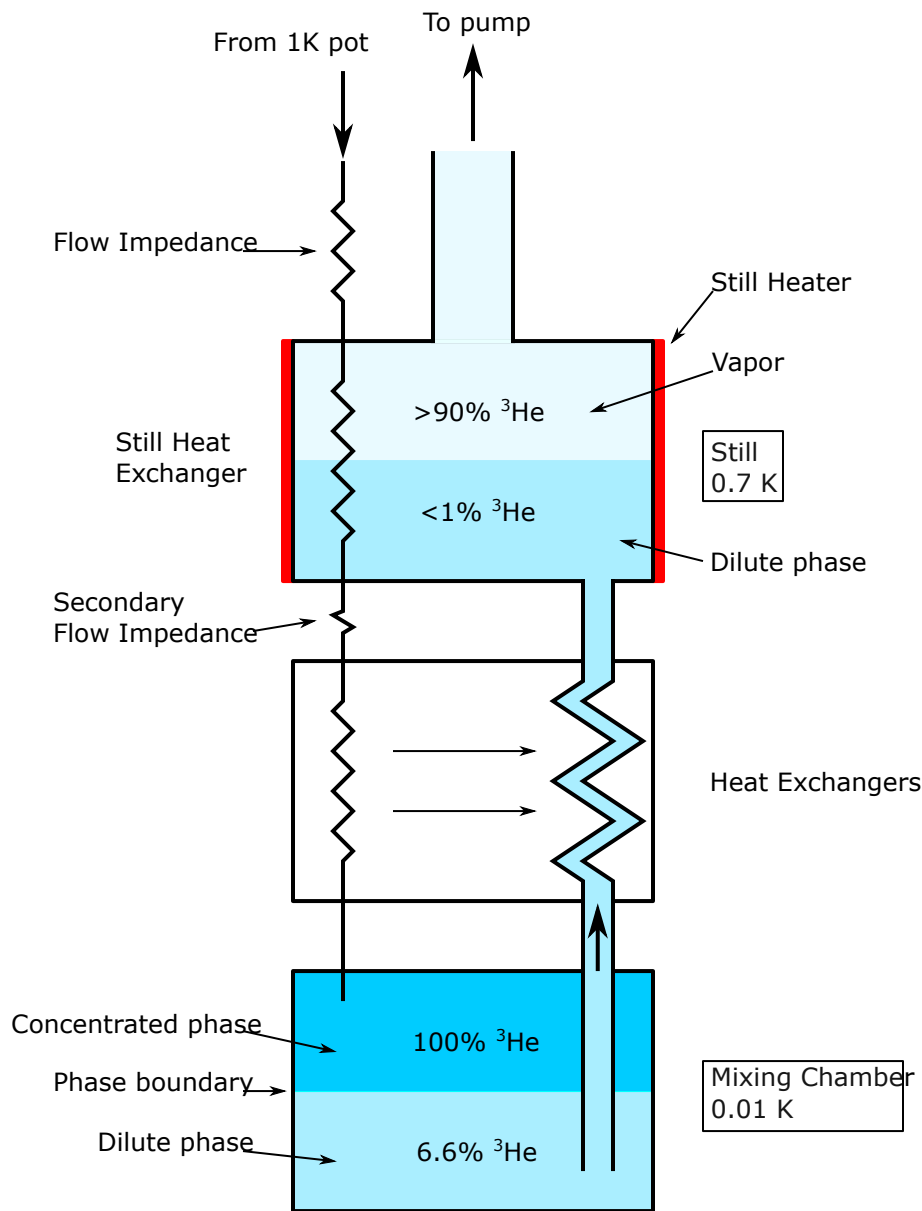
Figure 61: Schematic of the dilution unit. Percentages indicate the percent of ^{3}He composing the ^{3}He-^{4}He mixture. Adapted from Ref. [183].

which helps to reduce its pressure and lower the temperature of the liquid to ~ 1.5 K. The 1 K pot is continuously pumped to keep the pressure low reduce the temperature of the liquid helium from 4 K to ~ 1 K. The next stage is the Still which is at a temperature of 700 mK. The next stage is the 50 mK stage which is thermally connected to the Still through continuous heat exchangers. Additional heat exchangers connect the 50 mK stage to the mixing chamber plate and the mixing chamber where the cooling occurs.

A.2.1.1 Leiden MNK   The dilution refrigerator used in most of the experiments discussed here is a Leiden MNK 700. It is what's known as a 'wet' dilution refrigerator as it uses liquid ^{4}He to precool the mixture to 4.2 K, and 1.5 K. The Leiden MNK system used for these experiments can reach a base temperature of < 10 mK. While sweeping a magnetic field and if the rotator was installed the typical base temperature of the samples during experiments was $T \sim 25$ mK. The ^{4}He cryostat for the Leiden MNK system is shown in Fig. 62 and the dilution insert it shown in Fig. 63. A detailed schematic of the system showing the cryostat, insert, and supporting infrastructure is shown in Fig. 64.

The rooms housing the dilution refrigerators were designed to isolate the system and reduce interference from vibrations and external fields. A schematic for the room configuration is shown in Fig. 65. The cryostat sits on a large floating platform to decouple it from the vibrations in the building. The room is sound and RF field isolated. All of the vacuum lines that go to the cryostat pass through the concrete floor and are connected to the floating platform with flexible vacuum hoses. The vacuum lines pass through the floor and into an adjacent room where they connect to the gas handling system (GHS) which holds all of the values and pumps for circulating mixture and operating the cryostat. This has the advantage of separating all of the noisy components of the system from the experiments. A more detailed diagram of the mixture and auxiliary pumping circuits for the Leiden MNK system can be found in Fig. 66.

A.2.2   Superconducting magnet and 2-axis rotator

The Leiden MNK system includes a 18/20 T superconducting magnet and a 2-axis rotator. The sample can be rotated in any direction using a 2-axis rotator (Fig. 67), in order to apply

Figure 62: ^{4}He cryostat with 18/20 T superconducting magnet for the Leiden MNK dilution refrigerator insert.
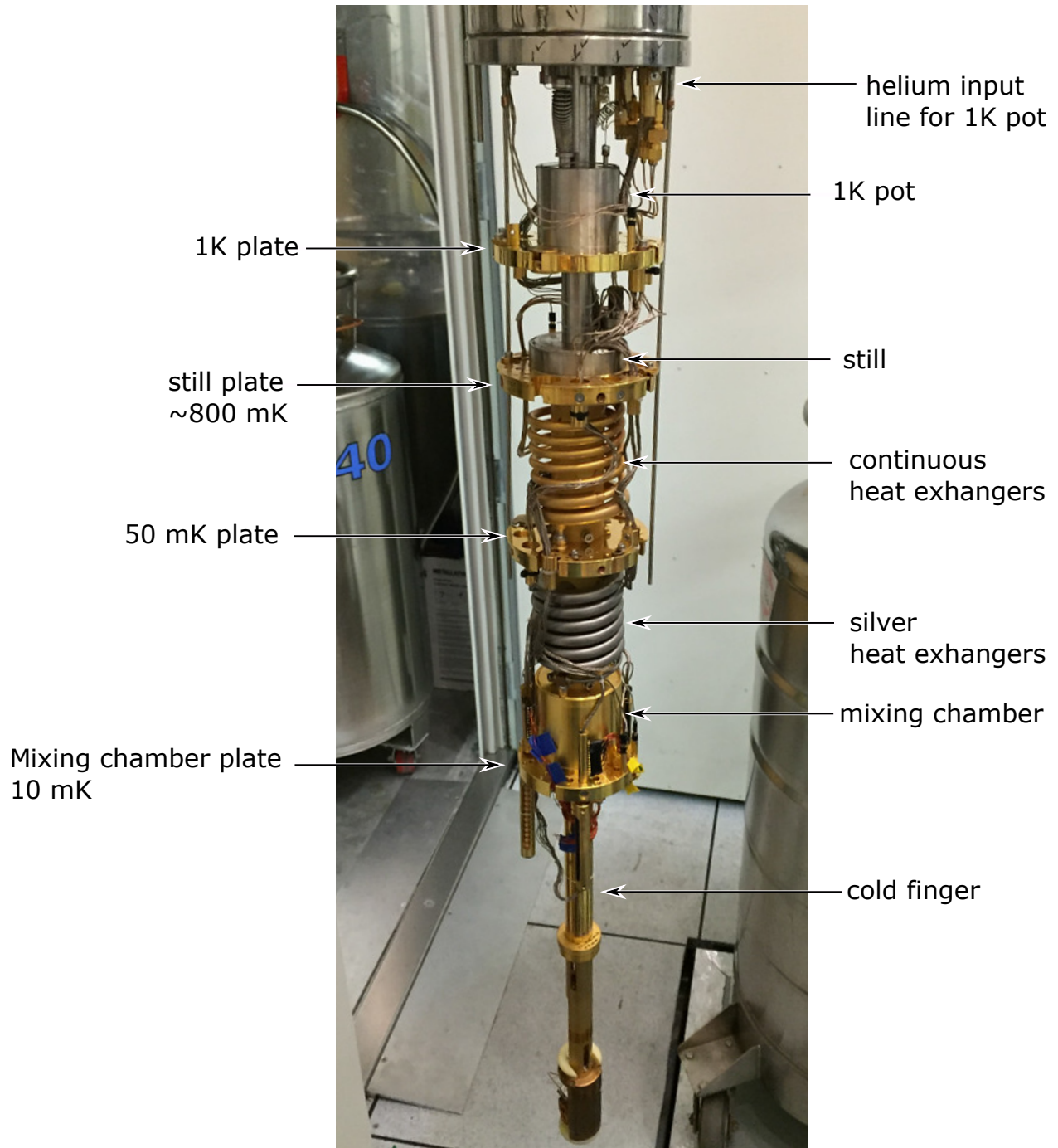
Figure 63: Leiden MNK dilution refrigerator insert. The sample is mounted to the bottom of the cold finger attached to the mixing chamber plate. The insert is lowered into the ^{4}He cryostat which cools it to 4 K. Circulation of the helium mixture cools the system to 10 mK.

Figure 64: Schematic of Leiden MNK cryostat system. Lines travel from the SPM room to an adjacent pump room shown in 65.
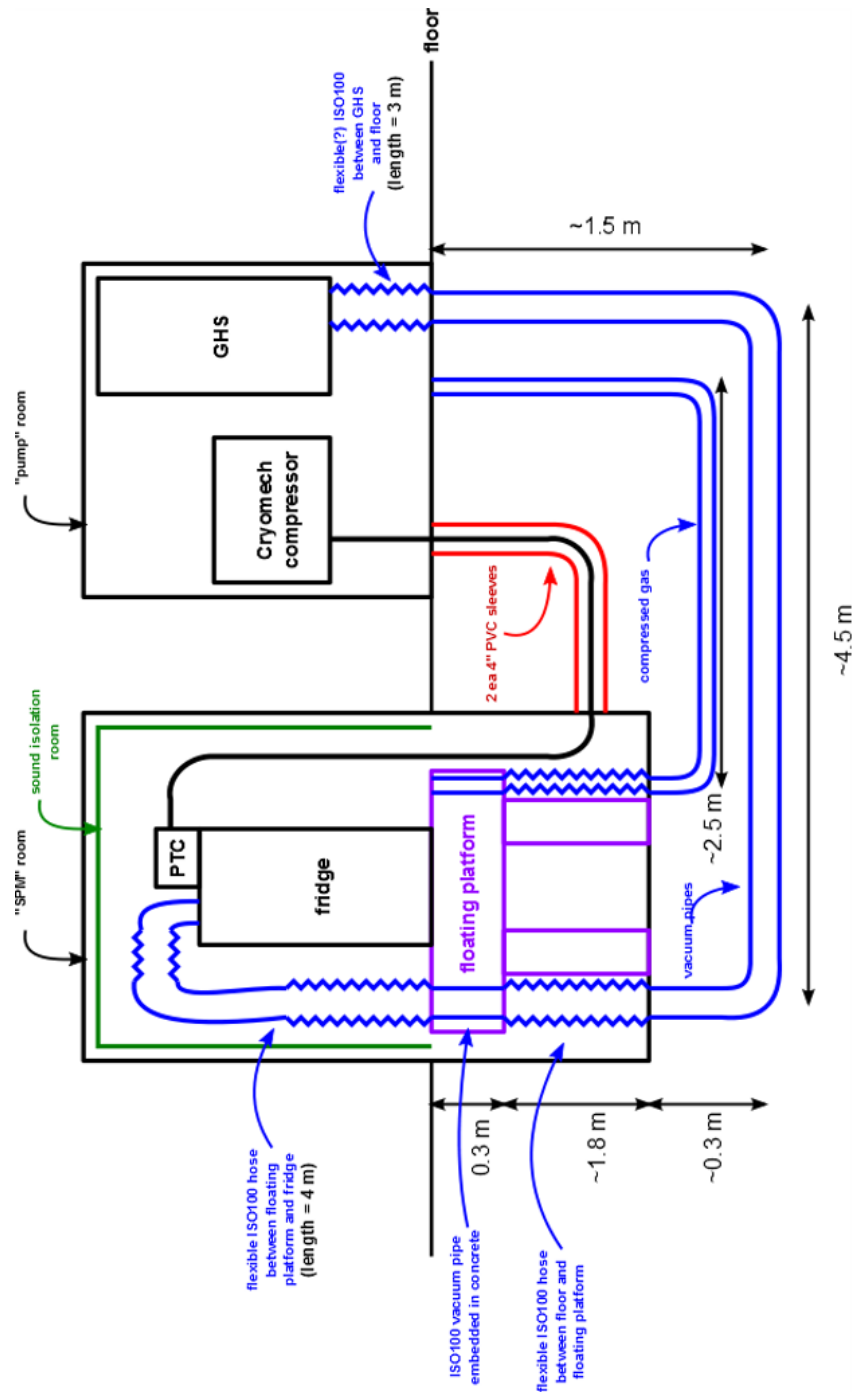
Figure 65: Schematic of the rooms housing the cryostats and supporting equipment. This layout helps to isolate the measurement equipment from the noise and vibration of mechanical pumps.

Figure 66: Diagram of Leiden MNK setup. The cryostat is located in the SPM room and the gas handling system is located in an adjacent pump room.

magnetic fields up to 20 T in any direction relative to the sample. The 2-axis rotator uses slip-stick motion to rotate both axes and a resistive encoder to determine the position of the rotator. Monitoring the position of the resistive encoder requires applying 1 V to the encoders which heats up the sample to above 50 mK. When not rotating the voltage can be reduced so as not to cause heating of the sample. Rotating also produces significant heating of the sample. Care must be taken not to rotate to much otherwise the mixing chamber will heat up enough to blow out the mixture and cause an automatic collection of the mixture to take place. Rotating should be limited to 10°. Allow for about 30 minutes of cooling after rotating before taking measurements. The wiring for the rotator includes a cable from the controller to a room temperature vacuum breakout box. Wires from the breakout box down to the 4K stage of the fridge are made of copper. Wires from the 4K stage down to the mixing chamber stage are made of a superconducting material and are thermalized at each temperature stage. From the mixing chamber down to the rotator are copper wires.

Figure 67: 2-axis rotator on Leiden MNK dilution insert. The 2-axis rotation allows the magnetic field of up to 20 T to be applied in any orientation relative to the sample.

Appendix B Sample information

This chapter provides information about the growth and processing parameters of the LaAlO$_3$/SrTiO$_3$ samples used in these experiments (Table 4). It also details the c-AFM writing parameters used for the devices discussed in Chapters 3-7 (Table 5).

Table 4: All samples were grown at a temperature of T = 550 °C, and an Oxygen pressure of PO_2 = 10E-3 mbar. Table containing the growth and processing parameters for the samples used in the experiments described here.

Sample	substrate	date received	mill param. nm (min)	deposition param.
SA02671	SrTiO₃	4/4/2013	20 (25)	4nm(15s)Ti+20nm(25s)Au 1st step; 5nm(20s)Ti +50nm(60s) Au 2nd step
SA02703	double etched SrTiO₃	8/26/2013	20 (25)	5nm(20s)Ti+25nm(30s)Au 1st step; 5nm(20s) Ti +50nm(60s) Au 2nd step
SA02704	double etched SrTiO₃	8/26/2013	20 (25)	5nm(20s)Ti+25nm(30s)Au 1st step; 5nm(20s)+50nm(60s) Au 2nd step
SA02835	SrTiO₃	2/10/2015	20 (25)	4nm(17s)Ti+25nm(30s)Au 1st step; 5nm(17s)+50nm(60s) Au 2nd step
SA02836	SrTiO₃	2/10/2015	20 (25)	4nm(17s)Ti+25nm(30s)Au 1st step; 5nm(17s)+50nm(60s) Au 2nd step
SA03018	SrTiO₃	3/20/2017	20 (25.1)	4nm (17s) Ti + 25nm (30s) Au 1st step; 4nm (17s) Ti + 50nm (60s) Au 2nd step

Table 5: List of the devices used in the experiments discussed in this thesis and their c-AFM writing parameters including device type and relevant device geometry.

Sample	Device	Device type	device geometry
SA02836H.20160119	Device W1	electron waveguide	$L_B = 20$ nm, $L_S = 50$ nm, $L_C = 500$ nm
SA02836H.20160123	Device W2	electron waveguide	$L_B = 20$ nm, $L_S = 1000$ nm, $L_C = 1800$ nm
SA02703M.20141031	Device W3	electron waveguide	$L_B = 5$ nm, $L_S = 10$ nm, $L_C = 350$ nm
SA02836K.20151223	Device W4	electron waveguide	$L_B = 20$ nm, $L_C = 1500$ nm, $L_S = 700$ nm
SA02836H.20160121	Device W5	electron waveguide	$L_B = 20$ nm, $L_C = 500$ nm, $L_S = 250$ nm
SA02836H.20160620	Device P1	electron waveguide	$L_B = 20$ nm, $L_S = 50$ nm, $L_C = 500$ nm
SA02836H.20160503	Device P2	electron waveguide	$L_B = 20$ nm, $L_S = 50$ nm, $L_C = 500$ nm
SA02836H.20160926	Device P3	electron waveguide	$L_B = 30$ nm, $L_S = 1000$ nm, $L_C = 1800$ nm
SA02836H.20160531	Device P4	electron waveguide	$L_B = 20$ nm, $L_S = 50$ nm, $L_C = 500$ nm
SA02836H.20160518	Device P5	electron waveguide	$L_B = 20$ nm, $L_S = 50$ nm, $L_C = 500$ nm
SA02836H.20160823	Device P6	electron waveguide	$L_B = 20$ nm, $L_S = 50$ nm, $L_C = 500$ nm
SA02836H.20170110	Device P7	electron waveguide	$L_B = 30$ nm, $L_S = 1000$ nm, $L_C = 1800$ nm

Continued on next page

Sample	Device	Device type	device geometry
SA02703M20141208	Device V1	vertical superlattice	SL: $V_{\text{tip}} = \pm 5$ V, 5 nm wavelength, 18 periods WG: $L_B = 5$ nm, $L_s = 10$ nm
SA02703M.20150130	Device V2	vertical superlattice	SL: $V_{\text{tip}} = \pm 5$ V, 5 nm wavelength, 18 periods WG: $L_B = 5$ nm, $L_s = 10$ nm
SA03018H.20170509	Device L1	lateral superlattice	SL: 5 nm amplitude, 10 nm wavelength, 40 periods
SA03018H.20170516	Device L2	lateral superlattice	SL: 5 nm amplitude, 11.5 nm wavelength, 34 periods
SA03018F.20171127	Device H1	helical superlattice	lateral: 10nm amp, 10 nm wavelength, 34 periods vertical: $V_{\text{tip}} = +5$ V/ $+15$ V
SA03018D.20181008	Device H2	helical superlattice	lateral: 10nm amp, 10 nm wavelength, 34 periods vertical: $V_{\text{tip}} = \pm 2.5$ V

Bibliography

[1]   R. P. Feynman. *Simulating physics with computers.* International Journal of Theoretical Physics **21**(6-7), 467 (1982). `http://dx.doi.org/10.1007/bf02650179`.

[2]   S. Lloyd. *Universal Quantum Simulators.* Science **273**(5278), 1073 (1996). `http://dx.doi.org/10.1126/science.273.5278.1073`.

[3]   E. Manousakis. *A Quantum-Dot Array as Model for Copper-Oxide Superconductors: A Dedicated Quantum Simulator for the Many-Fermion Problem.* Journal of Low Temperature Physics **126**(5/6), 1501 (2002). `http://dx.doi.org/10.1023/a:1014295416763`.

[4]   C. Cen, S. Thiel, G. Hammerl, C. W. Schneider, K. E. Andersen, C. S. Hellberg, J. Mannhart, and J. Levy. *Nanoscale control of an interfacial metal–insulator transition at room temperature.* Nature Materials **7**(4), 298 (2008). `http://dx.doi.org/10.1038/nmat2136`.

[5]   C. Cen, S. Thiel, J. Mannhart, and J. Levy. *Oxide Nanoelectronics on Demand.* Science **323**(5917), 1026 (2009). `http://dx.doi.org/10.1126/science.1168294`.

[6]   J. J. Sakurai. *Modern Quantum Mechanics (Revised Edition).* Addison Wesley (1993). ISBN 978-0201539295. `https://www.amazon.com/Modern-Quantum-Mechanics-Revised-Sakurai/dp/0201539292?SubscriptionId=AKIAIOBINVZYXZQZ2U3A&tag=chimbori05-20&linkCode=xm2&camp=2025&creative=165953&creativeASIN=0201539292`.

[7]   A. Montanaro. *Quantum algorithms: an overview.* npj Quantum Information **2**(1) (2016). `http://dx.doi.org/10.1038/npjqi.2015.23`.

[8]   D. Wecker, M. B. Hastings, N. Wiebe, B. K. Clark, C. Nayak, and M. Troyer. *Solving strongly correlated electron models on a quantum computer.* Physical Review A **92**(6) (2015). `http://dx.doi.org/10.1103/physreva.92.062318`.

[9]   P. W. Shor. *Polynomial-Time Algorithms for Prime Factorization and Discrete Logarithms on a Quantum Computer.* SIAM Journal on Computing **26**(5), 1484 (1997). `http://dx.doi.org/10.1137/s0097539795293172`.

[10]   C. L. Degen, F. Reinhard, and P. Cappellaro. *Quantum sensing.* Reviews of Modern Physics **89**(3) (2017). `http://dx.doi.org/10.1103/revmodphys.89.035002`.

[11]   J. Preskill. *Quantum Computing in the NISQ era and beyond.* Quantum **2**, 79 (2018). `http://dx.doi.org/10.22331/q-2018-08-06-79`.

[12] J. I. Cirac and P. Zoller. *Goals and opportunities in quantum simulation.* Nature Physics **8**(4), 264 (2012). http://dx.doi.org/10.1038/nphys2275.

[13] I. Georgescu, S. Ashhab, and F. Nori. *Quantum simulation.* Reviews of Modern Physics **86**(1), 153 (2014). http://dx.doi.org/10.1103/revmodphys.86.153.

[14] M. Greiner, O. Mandel, T. Esslinger, T. W. Hänsch, and I. Bloch. *Quantum phase transition from a superfluid to a Mott insulator in a gas of ultracold atoms.* Nature **415**(6867), 39 (2002). http://dx.doi.org/10.1038/415039a.

[15] D. Jaksch and P. Zoller. *The cold atom Hubbard toolbox.* Annals of Physics **315**(1), 52 (2005). http://dx.doi.org/10.1016/j.aop.2004.09.010.

[16] D. Greif, T. Uehlinger, G. Jotzu, L. Tarruell, and T. Esslinger. *Short-Range Quantum Magnetism of Ultracold Fermions in an Optical Lattice.* Science **340**(6138), 1307 (2013). http://dx.doi.org/10.1126/science.1236362.

[17] D. Porras and J. I. Cirac. *Effective Quantum Spin Systems with Trapped Ions.* Physical Review Letters **92**(20) (2004). http://dx.doi.org/10.1103/physrevlett.92.207901.

[18] J. G. Bohnet, B. C. Sawyer, J. W. Britton, M. L. Wall, A. M. Rey, M. Foss-Feig, and J. J. Bollinger. *Quantum spin dynamics and entanglement generation with hundreds of trapped ions.* Science **352**(6291), 1297 (2016). http://dx.doi.org/10.1126/science.aad9958.

[19] J. Zhang, P. W. Hess, A. Kyprianidis, P. Becker, A. Lee, J. Smith, G. Pagano, I.-D. Potirniche, A. C. Potter, A. Vishwanath, N. Y. Yao, and C. Monroe. *Observation of a discrete time crystal.* Nature **543**(7644), 217 (2017). http://dx.doi.org/10.1038/nature21413.

[20] A. A. Houck, H. E. Türeci, and J. Koch. *On-chip quantum simulation with superconducting circuits.* Nature Physics **8**(4), 292 (2012). http://dx.doi.org/10.1038/nphys2251.

[21] A. Chiesa, P. Santini, D. Gerace, J. Raftery, A. A. Houck, and S. Carretta. *Digital quantum simulators in a scalable architecture of hybrid spin-photon qubits.* Scientific Reports **5**(1) (2015). http://dx.doi.org/10.1038/srep16036.

[22] M. Fitzpatrick, N. M. Sundaresan, A. C. Li, J. Koch, and A. A. Houck. *Observation of a Dissipative Phase Transition in a One-Dimensional Circuit QED Lattice.* Physical Review X **7**(1) (2017). http://dx.doi.org/10.1103/physrevx.7.011016.

[23] A. Politi, J. C. F. Matthews, and J. L. O'Brien. *Shor's Quantum Factoring Algorithm on a Photonic Chip.* Science **325**(5945), 1221 (2009). http://dx.doi.org/10.1126/science.1173731.

[24] A. Peruzzo, M. Lobino, J. C. F. Matthews, N. Matsuda, A. Politi, K. Poulios, X.-Q. Zhou, Y. Lahini, N. Ismail, K. Worhoff, Y. Bromberg, Y. Silberberg, M. G. Thompson, and J. L.

OBrien. *Quantum Walks of Correlated Photons.* Science **329**(5998), 1500 (2010). `http://dx.doi.org/10.1126/science.1193515`.

[25] J. C. F. Matthews, K. Poulios, J. D. A. Meinecke, A. Politi, A. Peruzzo, N. Ismail, K. Wörhoff, M. G. Thompson, and J. L. O'Brien. *Observing fermionic statistics with photons in arbitrary processes.* Scientific Reports **3**(1) (2013). `http://dx.doi.org/10.1038/srep01539`.

[26] T. Byrnes, N. Y. Kim, K. Kusudo, and Y. Yamamoto. *Quantum simulation of Fermi-Hubbard models in semiconductor quantum-dot arrays.* Physical Review B **78**(7) (2008). `http://dx.doi.org/10.1103/physrevb.78.075320`.

[27] A. Singha, M. Gibertini, B. Karmakar, S. Yuan, M. Polini, G. Vignale, M. I. Katsnelson, A. Pinczuk, L. N. Pfeiffer, K. W. West, and V. Pellegrini. *Two-Dimensional Mott-Hubbard Electrons in an Artificial Honeycomb Lattice.* Science **332**(6034), 1176 (2011). `http://dx.doi.org/10.1126/science.1204333`.

[28] M. R. Slot, T. S. Gardenier, P. H. Jacobse, G. C. P. van Miert, S. N. Kempkes, S. J. M. Zevenhuizen, C. M. Smith, D. Vanmaekelbergh, and I. Swart. *Experimental realization and characterization of an electronic Lieb lattice.* Nature Physics **13**(7), 672 (2017). `http://dx.doi.org/10.1038/nphys4105`.

[29] R. Drost, T. Ojanen, A. Harju, and P. Liljeroth. *Topological states in engineered atomic lattices.* Nature Physics **13**(7), 668 (2017). `http://dx.doi.org/10.1038/nphys4080`.

[30] H. Bernien, S. Schwartz, A. Keesling, H. Levine, A. Omran, H. Pichler, S. Choi, A. S. Zibrov, M. Endres, M. Greiner, V. Vuletić, and M. D. Lukin. *Probing many-body dynamics on a 51-atom quantum simulator.* Nature **551**(7682), 579 (2017). `http://dx.doi.org/10.1038/nature24622`.

[31] J. Zhang, G. Pagano, P. W. Hess, A. Kyprianidis, P. Becker, H. Kaplan, A. V. Gorshkov, Z.-X. Gong, and C. Monroe. *Observation of a many-body dynamical phase transition with a 53-qubit quantum simulator.* Nature **551**(7682), 601 (2017). `http://dx.doi.org/10.1038/nature24654`.

[32] C. Gross and I. Bloch. *Quantum simulations with ultracold atoms in optical lattices.* Science **357**(6355), 995 (2017). `http://dx.doi.org/10.1126/science.aal3837`.

[33] Y.-Y. Pai, A. Tylan-Tyler, P. Irvin, and J. Levy. *Physics of $SrTiO_3$-based heterostructures and nanostructures: a review.* Reports on Progress in Physics **81**(3), 036503 (2018). `http://dx.doi.org/10.1088/1361-6633/aa892d`.

[34] A. Ohtomo and H. Y. Hwang. *A high-mobility electron gas at the $LaAlO_3/SrTiO_3$ heterointerface.* Nature **427**(6973), 423 (2004). `http://dx.doi.org/10.1038/nature02308`.

[35]   M. Kawasaki, K. Takahashi, T. Maeda, R. Tsuchiya, M. Shinohara, O. Ishiyama, T. Yonezawa, M. Yoshimoto, and H. Koinuma. *Atomic Control of the SrTiO₃ Crystal Surface.* Science **266**(5190), 1540 (1994). http://dx.doi.org/10.1126/science.266.5190.1540.

[36]   M. Basletic, J.-L. Maurice, C. Carrétéro, G. Herranz, O. Copie, M. Bibes, É. Jacquet, K. Bouzehouane, S. Fusil, and A. Barthélémy. *Mapping the spatial distribution of charge carriers in LaAlO₃/SrTiO₃ heterostructures.* Nature Materials **7**(8), 621 (2008). http://dx.doi.org/10.1038/nmat2223.

[37]   O. Copie, V. Garcia, C. Bödefeld, C. Carrétéro, M. Bibes, G. Herranz, E. Jacquet, J.-L. Maurice, B. Vinter, S. Fusil, K. Bouzehouane, H. Jaffrès, and A. Barthélémy. *Towards Two-Dimensional Metallic Behavior at LaAlO₃/SrTiO₃ Interfaces.* Physical Review Letters **102**(21) (2009). http://dx.doi.org/10.1103/physrevlett.102.216804.

[38]   N. Nakagawa, H. Y. Hwang, and D. A. Muller. *Why some interfaces cannot be sharp.* Nature Materials **5**(3), 204 (2006). http://dx.doi.org/10.1038/nmat1569.

[39]   Z. Zhong, P. X. Xu, and P. J. Kelly. *Polarity-induced oxygen vacancies at LaAlO₃/SrTiO₃ interfaces.* Physical Review B **82**(16) (2010). http://dx.doi.org/10.1103/physrevb.82.165127.

[40]   N. C. Bristowe, P. B. Littlewood, and E. Artacho. *Surface defects and conduction in polar oxide heterostructures.* Physical Review B **83**(20) (2011). http://dx.doi.org/10.1103/physrevb.83.205405.

[41]   Y. Li, S. N. Phattalung, S. Limpijumnong, J. Kim, and J. Yu. *Formation of oxygen vacancies and charge carriers induced in then-type interface of a LaAlO₃ overlayer on SrTiO₃ (001).* Physical Review B **84**(24) (2011). http://dx.doi.org/10.1103/physrevb.84.245307.

[42]   L. Qiao, T. C. Droubay, V. Shutthanandan, Z. Zhu, P. V. Sushko, and S. A. Chambers. *Thermodynamic instability at the stoichiometric LaAlO₃/SrTiO₃ (001) interface.* Journal of Physics: Condensed Matter **22**(31), 312201 (2010). http://dx.doi.org/10.1088/0953-8984/22/31/312201.

[43]   F. Schoofs, M. A. Carpenter, M. E. Vickers, M. Egilmez, T. Fix, J. E. Kleibeuker, J. L. MacManus-Driscoll, and M. G. Blamire. *Carrier density modulation by structural distortions at modified LaAlO3/SrTiO3interfaces.* Journal of Physics: Condensed Matter **25**(17), 175005 (2013). http://dx.doi.org/10.1088/0953-8984/25/17/175005.

[44]   L. Yu and A. Zunger. *A polarity-induced defect mechanism for conductivity and magnetism at polar–nonpolar oxide interfaces.* Nature Communications **5**(1) (2014). http://dx.doi.org/10.1038/ncomms6118.

[45] Z. S. Popović, S. Satpathy, and R. M. Martin. *Origin of the Two-Dimensional Electron Gas Carrier Density at the LaAlO₃ on SrTiO₃ Interface.* Physical Review Letters **101**(25) (2008). `http://dx.doi.org/10.1103/physrevlett.101.256801`.

[46] R. Pentcheva and W. E. Pickett. *Avoiding the Polarization Catastrophe in LaAlO₃ Overlayers on SrTiO₃ (001) through Polar Distortion.* Physical Review Letters **102**(10) (2009). `http://dx.doi.org/10.1103/physrevlett.102.107602`.

[47] M. B. Shalom, M. Sachs, D. Rakhmilevitch, A. Palevski, and Y. Dagan. *Tuning Spin-Orbit Coupling and Superconductivity at the SrTiO₃/LaAlO₃ Interface: A Magnetotransport Study.* Physical Review Letters **104**(12) (2010). `http://dx.doi.org/10.1103/physrevlett.104.126802`.

[48] A. D. Caviglia, M. Gabay, S. Gariglio, N. Reyren, C. Cancellieri, and J.-M. Triscone. *Tunable Rashba Spin-Orbit Interaction at Oxide Interfaces.* Physical Review Letters **104**(12) (2010). `http://dx.doi.org/10.1103/physrevlett.104.126803`.

[49] Y.-L. Han, S.-C. Shen, J. You, H.-O. Li, Z.-Z. Luo, C.-J. Li, G.-L. Qu, C.-M. Xiong, R.-F. Dou, L. He, D. Naugle, G.-P. Guo, and J.-C. Nie. *Two-dimensional superconductivity at (110) LaAlO₃/SrTiO₃ interfaces.* Applied Physics Letters **105**(19), 192603 (2014). `http://dx.doi.org/10.1063/1.4901940`.

[50] Y. Chen, N. Pryds, J. E. Kleibeuker, G. Koster, J. Sun, E. Stamate, B. Shen, G. Rijnders, and S. Linderoth. *Metallic and Insulating Interfaces of Amorphous SrTiO₃-Based Oxide Heterostructures.* Nano Letters **11**(9), 3774 (2011). `http://dx.doi.org/10.1021/nl201821j`.

[51] M. Salluzzo, J. C. Cezar, N. B. Brookes, V. Bisogni, G. M. D. Luca, C. Richter, S. Thiel, J. Mannhart, M. Huijben, A. Brinkman, G. Rijnders, and G. Ghiringhelli. *Orbital Reconstruction and the Two-Dimensional Electron Gas at the LaAlO₃/SrTiO₃ Interface.* Physical Review Letters **102**(16) (2009). `http://dx.doi.org/10.1103/physrevlett.102.166804`.

[52] C. Cancellieri, M. L. Reinle-Schmitt, M. Kobayashi, V. N. Strocov, P. R. Willmott, D. Fontaine, P. Ghosez, A. Filippetti, P. Delugas, and V. Fiorentini. *Doping-dependent band structure of LaAlO₃/SrTiO₃ interfaces by soft x-ray polarization-controlled resonant angle-resolved photoemission.* Physical Review B **89**(12) (2014). `http://dx.doi.org/10.1103/physrevb.89.121412`.

[53] S. M. Walker, S. Riccò, F. Y. Bruno, A. de la Torre, A. Tamai, E. Golias, A. Varykhalov, D. Marchenko, M. Hoesch, M. S. Bahramy, P. D. C. King, J. Sánchez-Barriga, and F. Baumberger. *Absence of giant spin splitting in the two-dimensional electron liquid at the surface of SrTiO₃ (001).* Physical Review B **93**(24) (2016). `http://dx.doi.org/10.1103/physrevb.93.245143`.

[54] S. Thiel, G. Hammerl, A. Schmehl, C. W. Schneider, and J. Mannhart. *Tunable Quasi-Two-Dimensional Electron Gases in Oxide Heterostructures.* Science **313**(5795), 1942 (2006). `http://dx.doi.org/10.1126/science.1131091`.

[55] N. Reyren, S. Thiel, A. D. Caviglia, L. F. Kourkoutis, G. Hammerl, C. Richter, C. W. Schneider, T. Kopp, A.-S. Ruetschi, D. Jaccard, M. Gabay, D. A. Muller, J.-M. Triscone, and J. Mannhart. *Superconducting Interfaces Between Insulating Oxides.* Science **317**(5842), 1196 (2007). `http://dx.doi.org/10.1126/science.1146006`.

[56] F. Bi, M. Huang, S. Ryu, H. Lee, C.-W. Bark, C.-B. Eom, P. Irvin, and J. Levy. *Room-temperature electronically-controlled ferromagnetism at the LaAlO$_3$/SrTiO$_3$ interface.* Nature Communications **5**(1) (2014). `http://dx.doi.org/10.1038/ncomms6019`.

[57] F. Bi, M. Huang, H. Lee, C.-B. Eom, P. Irvin, and J. Levy. *LaAlO$_3$ thickness window for electronically controlled magnetism at LaAlO$_3$/SrTiO$_3$ heterointerfaces.* Applied Physics Letters **107**(8), 082402 (2015). `http://dx.doi.org/10.1063/1.4929430`.

[58] J. F. Schooley, W. R. Hosler, and M. L. Cohen. *Superconductivity in Semiconducting SrTiO$_3$.* Physical Review Letters **12**(17), 474 (1964). `http://dx.doi.org/10.1103/physrevlett.12.474`.

[59] X. Lin, Z. Zhu, B. Fauqué, and K. Behnia. *Fermi Surface of the Most Dilute Superconductor.* Physical Review X **3**(2) (2013). `http://dx.doi.org/10.1103/physrevx.3.021002`.

[60] C. S. Koonce, M. L. Cohen, J. F. Schooley, W. R. Hosler, and E. R. Pfeiffer. *Superconducting Transition Temperatures of Semiconducting SrTiO$_3$.* Physical Review **163**(2), 380 (1967). `http://dx.doi.org/10.1103/physrev.163.380`.

[61] B. Kalisky, E. M. Spanton, H. Noad, J. R. Kirtley, K. C. Nowack, C. Bell, H. K. Sato, M. Hosoda, Y. Xie, Y. Hikita, C. Woltmann, G. Pfanzelt, R. Jany, C. Richter, H. Y. Hwang, J. Mannhart, and K. A. Moler. *Locally enhanced conductivity due to the tetragonal domain structure in LaAlO$_3$/SrTiO$_3$ heterointerfaces.* Nature Materials **12**(12), 1091 (2013). `http://dx.doi.org/10.1038/nmat3753`.

[62] M. Honig, J. A. Sulpizio, J. Drori, A. Joshua, E. Zeldov, and S. Ilani. *Local electrostatic imaging of striped domain order in LaAlO$_3$/SrTiO$_3$.* Nature Materials **12**(12), 1112 (2013). `http://dx.doi.org/10.1038/nmat3810`.

[63] R. A. Cowley. *Lattice Dynamics and Phase Transitions of Strontium Titanate.* Physical Review **134**(4A), A981 (1964). `http://dx.doi.org/10.1103/physrev.134.a981`.

[64] Y.-Y. Pai, H. Lee, J.-W. Lee, A. Annadi, G. Cheng, S. Lu, M. Tomczyk, M. Huang, C.-B. Eom, P. Irvin, and J. Levy. *One-Dimensional Nature of Superconductivity at the LaAlO$_3$/SrTiO$_3$ Interface.* Physical Review Letters **120**(14) (2018). `http://dx.doi.org/10.1103/physrevlett.120.147001`.

[65] C. W. Schneider, S. Thiel, G. Hammerl, C. Richter, and J. Mannhart. *Microlithography of electron gases formed at interfaces in oxide heterostructures.* Applied Physics Letters **89**(12), 122101 (2006). `http://dx.doi.org/10.1063/1.2354422`.

[66] D. Stornaiuolo, S. Gariglio, N. J. G. Couto, A. Fête, A. D. Caviglia, G. Seyfarth, D. Jaccard, A. F. Morpurgo, and J.-M. Triscone. *In-plane electronic confinement in superconducting LaAlO$_3$/SrTiO$_3$ nanostructures.* Applied Physics Letters **101**(22), 222601 (2012). `http://dx.doi.org/10.1063/1.4768936`.

[67] P. P. Aurino, A. Kalabukhov, N. Tuzla, E. Olsson, T. Claeson, and D. Winkler. *Nanopatterning of the electron gas at the LaAlO$_3$/SrTiO$_3$ interface using low-energy ion beam irradiation.* Applied Physics Letters **102**(20), 201610 (2013). `http://dx.doi.org/10.1063/1.4807785`.

[68] H. Thierschmann, E. Mulazimoglu, N. Manca, S. Goswami, T. M. Klapwijk, and A. D. Caviglia. *Transport regimes of a split gate superconducting quantum point contact in the two-dimensional LaAlO$_3$/SrTiO$_3$ superfluid.* Nature Communications **9**(1) (2018). `http://dx.doi.org/10.1038/s41467-018-04657-z`.

[69] A. Jouan, G. Singh, E. Lesne, D. C. Vaz, M. Bibes, A. Barthélémy, C. Ulysse, D. Stornaiuolo, M. Salluzzo, S. Hurand, J. Lesueur, C. Feuillet-Palma, and N. Bergeal. *Quantized conductance in a one-dimensional ballistic oxide nanodevice* (2019). `http://arxiv.org/abs/1903.12134v1`.

[70] Y. Xie, C. Bell, T. Yajima, Y. Hikita, and H. Y. Hwang. *Charge Writing at the LaAlO$_3$/SrTiO$_3$ Surface.* Nano Letters **10**(7), 2588 (2010). `http://dx.doi.org/10.1021/nl1012695`.

[71] M. Boselli, D. Li, W. Liu, A. Fête, S. Gariglio, and J.-M. Triscone. *Characterization of atomic force microscopy written conducting nanowires at LaAlO3/SrTiO3 interfaces.* Applied Physics Letters **108**(6), 061604 (2016). `http://dx.doi.org/10.1063/1.4941817`.

[72] C. L. Kane, R. Mukhopadhyay, and T. C. Lubensky. *Fractional Quantum Hall Effect in an Array of Quantum Wires.* Physical Review Letters **88**(3) (2002). `http://dx.doi.org/10.1103/physrevlett.88.036401`.

[73] C. L. Kane, A. Stern, and B. I. Halperin. *Pairing in Luttinger Liquids and Quantum Hall States.* Physical Review X **7**(3) (2017). `http://dx.doi.org/10.1103/physrevx.7.031009`.

[74] T. Ihn. *Semiconductor Nanostructures.* Oxford University Press (2010). ISBN 0199534438. `https://www.ebook.de/de/product/9314389/thomas_ihn_semiconductor_nanostructures.html`.

[75] S. Datta. *Quantum Transport*. Cambridge University Press (2005). ISBN 0521631459. `https://www.ebook.de/de/product/3268640/supriyo_datta_quantum_transport.html`.

[76] D. L. Maslov and M. Stone. *Landauer conductance of Luttinger liquids with leads*. Physical Review B **52**(8), R5539 (1995). `http://dx.doi.org/10.1103/physrevb.52.r5539`.

[77] K. Nikolić and A. MacKinnon. *Conductance and conductance fluctuations of narrow disordered quantum wires*. Physical Review B **50**(15), 11008 (1994). `http://dx.doi.org/10.1103/physrevb.50.11008`.

[78] B. J. van Wees, H. van Houten, C. W. J. Beenakker, J. G. Williamson, L. P. Kouwenhoven, D. van der Marel, and C. T. Foxon. *Quantized conductance of point contacts in a two-dimensional electron gas*. Physical Review Letters **60**(9), 848 (1988). `http://dx.doi.org/10.1103/physrevlett.60.848`.

[79] D. A. Wharam, T. J. Thornton, R. Newbury, M. Pepper, H. Ahmed, J. E. F. Frost, D. G. Hasko, D. C. Peacock, D. A. Ritchie, and G. A. C. Jones. *One-dimensional transport and the quantisation of the ballistic resistance*. Journal of Physics C: Solid State Physics **21**(8), L209 (1988). `http://dx.doi.org/10.1088/0022-3719/21/8/002`.

[80] H. Hou, Y. Kozuka, J.-W. Liao, L. W. Smith, D. Kos, J. P. Griffiths, J. Falson, A. Tsukazaki, M. Kawasaki, and C. J. B. Ford. *Quantized conductance of one-dimensional strongly correlated electrons in an oxide heterostructure*. Physical Review B **99**(12) (2019). `http://dx.doi.org/10.1103/physrevb.99.121302`.

[81] P. Gallagher, M. Lee, J. R. Williams, and D. Goldhaber-Gordon. *Gate-tunable superconducting weak link and quantum point contact spectroscopy on a strontium titanate surface*. Nature Physics **10**(10), 748 (2014). `http://dx.doi.org/10.1038/nphys3049`.

[82] A. Ron and Y. Dagan. *One-Dimensional Quantum Wire Formed at the Boundary between Two Insulating LaAlO$_3$/SrTiO$_3$ Interfaces*. Physical Review Letters **112**(13) (2014). `http://dx.doi.org/10.1103/physrevlett.112.136801`.

[83] A. Annadi, G. Cheng, H. Lee, J.-W. Lee, S. Lu, A. Tylan-Tyler, M. Briggeman, M. Tomczyk, M. Huang, D. Pekker, C.-B. Eom, P. Irvin, and J. Levy. *Quantized Ballistic Transport of Electrons and Electron Pairs in LaAlO$_3$/SrTiO$_3$ Nanowires*. Nano Letters **18**(7), 4473 (2018). `http://dx.doi.org/10.1021/acs.nanolett.8b01614`.

[84] P. R. Willmott and J. R. Huber. *Pulsed laser vaporization and deposition*. Reviews of Modern Physics **72**(1), 315 (2000). `http://dx.doi.org/10.1103/revmodphys.72.315`.

[85] G. J. H. M. Rijnders, G. Koster, D. H. A. Blank, and H. Rogalla. *In situmonitoring during pulsed laser deposition of complex oxides using reflection high energy electron*

diffraction under high oxygen pressure. Applied Physics Letters **70**(14), 1888 (1997). `http://dx.doi.org/10.1063/1.118687`.

[86] A. Levy, F. Bi, M. Huang, S. Lu, M. Tomczyk, G. Cheng, P. Irvin, and J. Levy. *Writing and Low-Temperature Characterization of Oxide Nanostructures.* Journal of Visualized Experiments (89) (2014). `http://dx.doi.org/10.3791/51886`.

[87] F. Bi, D. F. Bogorin, C. Cen, C. W. Bark, J.-W. Park, C.-B. Eom, and J. Levy. *"Water-cycle" mechanism for writing and erasing nanostructures at the LaAlO$_3$/SrTiO$_3$ interface.* Applied Physics Letters **97**(17), 173110 (2010). `http://dx.doi.org/10.1063/1.3506509`.

[88] K. A. Brown, S. He, D. J. Eichelsdoerfer, M. Huang, I. Levy, H. Lee, S. Ryu, P. Irvin, J. Mendez-Arroyo, C.-B. Eom, C. A. Mirkin, and J. Levy. *Giant conductivity switching of LaAlO$_3$/SrTiO$_3$ heterointerfaces governed by surface protonation.* Nature Communications **7**, 10681 (2016). `http://dx.doi.org/10.1038/ncomms10681`.

[89] M. Huang, F. Bi, S. Ryu, C.-B. Eom, P. Irvin, and J. Levy. *Direct imaging of LaAlO$_3$/SrTiO$_3$ nanostructures using piezoresponse force microscopy.* APL Materials **1**(5), 052110 (2013). `http://dx.doi.org/10.1063/1.4831855`.

[90] Z. Jiang, X. Wu, H. Lee, J.-W. Lee, J. Li, G. Cheng, C.-B. Eom, J. Levy, and K. Lai. *Direct imaging of sketched conductive nanostructures at the LaAlO$_3$/SrTiO$_3$ interface.* Applied Physics Letters **111**(23), 233104 (2017). `http://dx.doi.org/10.1063/1.5005917`.

[91] LevyLab. *Multichannel Lockin* (2019). `https://github.com/levylabpitt/Multichannel-Lockin`.

[92] K. v. Klitzing, G. Dorda, and M. Pepper. *New Method for High-Accuracy Determination of the Fine-Structure Constant Based on Quantized Hall Resistance.* Physical Review Letters **45**(6), 494 (1980). `http://dx.doi.org/10.1103/physrevlett.45.494`.

[93] H. L. Stormer, D. C. Tsui, and A. C. Gossard. *The fractional quantum Hall effect.* Reviews of Modern Physics **71**(2), S298 (1999). `http://dx.doi.org/10.1103/revmodphys.71.s298`.

[94] J. M. Luttinger. *An Exactly Soluble Model of a Many-Fermion System.* Journal of Mathematical Physics **4**(9), 1154 (1963). `http://dx.doi.org/10.1063/1.1704046`.

[95] T. Giamarchi. *Quantum Physics in One Dimension.* Oxford University Press (2003). `http://dx.doi.org/10.1093/acprof:oso/9780198525004.001.0001`.

[96] O. M. Auslaender, H. Steinberg, A. Yacoby, Y. Tserkovnyak, B. I. Halperin, K. W. Baldwin, L. N. Pfeiffer, and K. W. West. *Spin-Charge Separation and Localization in One Dimension.* Science **308**(5718), 88 (2005). `http://dx.doi.org/10.1126/science.1107821`.

[97] H. Steinberg, G. Barak, A. Yacoby, L. N. Pfeiffer, K. W. West, B. I. Halperin, and K. L. Hur. *Charge fractionalization in quantum wires.* Nature Physics **4**(2), 116 (2007). `http://dx.doi.org/10.1038/nphys810`.

[98] R. Landauer. *Spatial Variation of Currents and Fields Due to Localized Scatterers in Metallic Conduction.* IBM Journal of Research and Development **1**(3), 223 (1957). `http://dx.doi.org/10.1147/rd.13.0223`.

[99] A. Yacoby, H. L. Stormer, N. S. Wingreen, L. N. Pfeiffer, K. W. Baldwin, and K. W. West. *Nonuniversal Conductance Quantization in Quantum Wires.* Physical Review Letters **77**(22), 4612 (1996). `http://dx.doi.org/10.1103/physrevlett.77.4612`.

[100] S. Frank, P. Poncharal, Z. L. Wang, and W. A. de Heer. *Carbon Nanotube Quantum Resistors.* Science **280**(5370), 1744 (1998). `http://dx.doi.org/10.1126/science.280.5370.1744`.

[101] Y.-M. Lin, V. Perebeinos, Z. Chen, and P. Avouris. *Electrical observation of subband formation in graphene nanoribbons.* Physical Review B **78**(16) (2008). `http://dx.doi.org/10.1103/physrevb.78.161409`.

[102] I. van Weperen, S. R. Plissard, E. P. A. M. Bakkers, S. M. Frolov, and L. P. Kouwenhoven. *Quantized Conductance in an InSb Nanowire.* Nano Letters **13**(2), 387 (2012). `http://dx.doi.org/10.1021/nl3035256`.

[103] G. Timp, A. M. Chang, P. Mankiewich, R. Behringer, J. E. Cunningham, T. Y. Chang, and R. E. Howard. *Quantum transport in an electron-wave guide.* Physical Review Letters **59**(6), 732 (1987). `http://dx.doi.org/10.1103/physrevlett.59.732`.

[104] F. D. M. Haldane. *'Luttinger liquid theory' of one-dimensional quantum fluids: I. Properties of the Luttinger model and their extension to the general 1D interacting spinless Fermi gas.* Journal of Physics C: Solid State Physics **14**(19), 2585 (1981). `http://dx.doi.org/10.1088/0022-3719/14/19/010`.

[105] C. L. Kane and M. P. A. Fisher. *Transmission through barriers and resonant tunneling in an interacting one-dimensional electron gas.* Physical Review B **46**(23), 15233 (1992). `http://dx.doi.org/10.1103/physrevb.46.15233`.

[106] T. Giamarchi and H. J. Schulz. *Anderson localization and interactions in one-dimensional metals.* Physical Review B **37**(1), 325 (1988). `http://dx.doi.org/10.1103/physrevb.37.325`.

[107] A. Tsukazaki, S. Akasaka, K. Nakahara, Y. Ohno, H. Ohno, D. Maryenko, A. Ohtomo, and M. Kawasaki. *Observation of the fractional quantum Hall effect in an oxide.* Nature Materials **9**(11), 889 (2010). `http://dx.doi.org/10.1038/nmat2874`.

[108] J. Falson, D. Maryenko, B. Friess, D. Zhang, Y. Kozuka, A. Tsukazaki, J. H. Smet, and M. Kawasaki. *Even-denominator fractional quantum Hall physics in ZnO*. Nature Physics **11**(4), 347 (2015). http://dx.doi.org/10.1038/nphys3259.

[109] A. Brinkman, M. Huijben, M. van Zalk, J. Huijben, U. Zeitler, J. C. Maan, W. G. van der Wiel, G. Rijnders, D. H. A. Blank, and H. Hilgenkamp. *Magnetic effects at the interface between non-magnetic oxides*. Nature Materials **6**(7), 493 (2007). http://dx.doi.org/10.1038/nmat1931.

[110] P. Irvin, J. P. Veazey, G. Cheng, S. Lu, C.-W. Bark, S. Ryu, C.-B. Eom, and J. Levy. *Anomalous High Mobility in LaAlO$_3$/SrTiO$_3$ Nanowires*. Nano Letters **13**(2), 364 (2013). http://dx.doi.org/10.1021/nl3033729.

[111] G. Cheng, J. P. Veazey, P. Irvin, C. Cen, D. F. Bogorin, F. Bi, M. Huang, S. Lu, C.-W. Bark, S. Ryu, K.-H. Cho, C.-B. Eom, and J. Levy. *Anomalous Transport in Sketched Nanostructures at the LaAlO$_3$/SrTiO$_3$ Interface*. Physical Review X **3**(1) (2013). http://dx.doi.org/10.1103/physrevx.3.011021.

[112] M. Tomczyk, G. Cheng, H. Lee, S. Lu, A. Annadi, J. P. Veazey, M. Huang, P. Irvin, S. Ryu, C.-B. Eom, and J. Levy. *Micrometer-Scale Ballistic Transport of Electron Pairs in LaAlO$_3$/SrTiO$_3$ Nanowires*. Physical Review Letters **117**(9) (2016). http://dx.doi.org/10.1103/physrevlett.117.096801.

[113] G. Cheng, P. F. Siles, F. Bi, C. Cen, D. F. Bogorin, C. W. Bark, C. M. Folkman, J.-W. Park, C.-B. Eom, G. Medeiros-Ribeiro, and J. Levy. *Sketched oxide single-electron transistor*. Nature Nanotechnology **6**(6), 343 (2011). http://dx.doi.org/10.1038/nnano.2011.56.

[114] R. Dingle, H. L. Störmer, A. C. Gossard, and W. Wiegmann. *Electron mobilities in modulation-doped semiconductor heterojunction superlattices*. Applied Physics Letters **33**(7), 665 (1978). http://dx.doi.org/10.1063/1.90457.

[115] A. P. Micolich. *What lurks below the last plateau: experimental studies of the $0.7 \times 2e^2/h$ conductance anomaly in one-dimensional systems*. Journal of Physics: Condensed Matter **23**(44), 443201 (2011). http://dx.doi.org/10.1088/0953-8984/23/44/443201.

[116] G. Cheng, A. Annadi, S. Lu, H. Lee, J.-W. Lee, M. Huang, C.-B. Eom, P. Irvin, and J. Levy. *Shubnikov–de Haas–like Quantum Oscillations in Artificial One-Dimensional LaAlO$_3$/SrTiO$_3$ Electron Channels*. Physical Review Letters **120**(7) (2018). http://dx.doi.org/10.1103/physrevlett.120.076801.

[117] F. Bi, M. Huang, C.-W. Bark, S. Ryu, S. Lee, C.-B. Eom, P. Irvin, and J. Levy. *Electromechanical response of top-gated LaAlO$_3$/SrTiO$_3$*. Journal of Applied Physics **119**(2), 025309 (2016). http://dx.doi.org/10.1063/1.4940045.

[118] M. A. Topinka, B. J. LeRoy, S. E. J. Shaw, E. J. Heller, R. M. Westervelt, K. D. Maranowski, and A. C. Gossard. *Imaging Coherent Electron Flow from a Quantum Point Contact*. Science **289**(5488), 2323 (2000). `http://dx.doi.org/10.1126/science.289.5488.2323`.

[119] G. Cheng, M. Tomczyk, S. Lu, J. P. Veazey, M. Huang, P. Irvin, S. Ryu, H. Lee, C.-B. Eom, C. S. Hellberg, and J. Levy. *Electron pairing without superconductivity*. Nature **521**(7551), 196 (2015). `http://dx.doi.org/10.1038/nature14398`.

[120] X.-W. Guan, M. T. Batchelor, and C. Lee. *Fermi gases in one dimension: From Bethe ansatz to experiments*. Reviews of Modern Physics **85**(4), 1633 (2013). `http://dx.doi.org/10.1103/revmodphys.85.1633`.

[121] B. Wang, H.-D. Chen, and S. D. Sarma. *Quantum phase diagram of fermion mixtures with population imbalance in one-dimensional optical lattices*. Physical Review A **79**(5) (2009). `http://dx.doi.org/10.1103/physreva.79.051604`.

[122] G. Orso, E. Burovski, and T. Jolicoeur. *Luttinger Liquid of Trimers in Fermi Gases with Unequal Masses*. Physical Review Letters **104**(6) (2010). `http://dx.doi.org/10.1103/physrevlett.104.065301`.

[123] D. L. Maslov. *Transport through dirty Luttinger liquids connected to reservoirs*. Physical Review B **52**(20), R14368 (1995). `http://dx.doi.org/10.1103/physrevb.52.r14368`.

[124] A. Sawada, Z. F. Ezawa, H. Ohno, Y. Horikoshi, Y. Ohno, S. Kishimoto, F. Matsukura, M. Yasumoto, and A. Urayama. *Phase Transition in the $\nu = 2$ Bilayer Quantum Hall State*. Physical Review Letters **80**(20), 4534 (1998). `http://dx.doi.org/10.1103/physrevlett.80.4534`.

[125] C. W. J. Beenakker and H. van Houten. *Josephson current through a superconducting quantum point contact shorter than the coherence length*. Physical Review Letters **66**(23), 3056 (1991). `http://dx.doi.org/10.1103/physrevlett.66.3056`.

[126] M. Kanász-Nagy, L. Glazman, T. Esslinger, and E. Demler. *Anomalous Conductances in an Ultracold Quantum Wire*. Physical Review Letters **117**(25) (2016). `http://dx.doi.org/10.1103/physrevlett.117.255302`.

[127] L. I. Glazman and A. V. Khaetskii. *Nonlinear Quantum Conductance of a Lateral Microconstraint in a Heterostructure*. Europhysics Letters (EPL) **9**(3), 263 (1989). `http://dx.doi.org/10.1209/0295-5075/9/3/013`.

[128] N. K. Patel, L. Martin-Moreno, M. Pepper, R. Newbury, J. E. F. Frost, D. A. Ritchie, G. A. C. Jones, J. T. M. B. Janssen, J. Singleton, and J. A. A. J. Perenboom. *Ballistic transport in one dimension: additional quantisation produced by an electric field*. Journal of Physics: Condensed Matter **2**(34), 7247 (1990). `http://dx.doi.org/10.1088/0953-8984/2/34/018`.

[129] M. Briggeman, M. Tomczyk, B. Tian, H. Lee, J.-W. Lee, Y. He, A. Tylan-Tyler, M. Huang, C.-B. Eom, D. Pekker, R. S. K. Mong, P. Irvin, and J. Levy. *Pascal conductance series in ballistic one-dimensional LaAlO$_3$/SrTiO$_3$ channels* (2019). `http://arxiv.org/abs/1909.05698v1`.

[130] S.-I. Tomonaga. *Remarks on Bloch's Method of Sound Waves applied to Many-Fermion Problems.* Progress of Theoretical Physics **5**(4), 544 (1950). `http://dx.doi.org/10.1143/ptp/5.4.544`.

[131] D. C. Mattis and E. H. Lieb. *Exact Solution of a Many-Fermion System and Its Associated Boson Field.* Journal of Mathematical Physics **6**(2), 304 (1965). `http://dx.doi.org/10.1063/1.1704281`.

[132] S. R. White. *Density matrix formulation for quantum renormalization groups.* Physical Review Letters **69**(19), 2863 (1992). `http://dx.doi.org/10.1103/physrevlett.69.2863`.

[133] Y. an Liao, A. S. C. Rittner, T. Paprotta, W. Li, G. B. Partridge, R. G. Hulet, S. K. Baur, and E. J. Mueller. *Spin-imbalance in a one-dimensional Fermi gas.* Nature **467**(7315), 567 (2010). `http://dx.doi.org/10.1038/nature09393`.

[134] A. Hamo, A. Benyamini, I. Shapir, I. Khivrich, J. Waissman, K. Kaasbjerg, Y. Oreg, F. von Oppen, and S. Ilani. *Electron attraction mediated by Coulomb repulsion.* Nature **535**(7612), 395 (2016). `http://dx.doi.org/10.1038/nature18639`.

[135] Á. Rapp, G. Zaránd, C. Honerkamp, and W. Hofstetter. *Color Superfluidity and "Baryon" Formation in Ultracold Fermions.* Physical Review Letters **98**(16) (2007). `http://dx.doi.org/10.1103/physrevlett.98.160405`.

[136] T. Kraemer, M. Mark, P. Waldburger, J. G. Danzl, C. Chin, B. Engeser, A. D. Lange, K. Pilch, A. Jaakkola, H.-C. Nägerl, and R. Grimm. *Evidence for Efimov quantum states in an ultracold gas of caesium atoms.* Nature **440**(7082), 315 (2006). `http://dx.doi.org/10.1038/nature04626`.

[137] G. Cheng, M. Tomczyk, A. B. Tacla, H. Lee, S. Lu, J. P. Veazey, M. Huang, P. Irvin, S. Ryu, C.-B. Eom, A. Daley, D. Pekker, and J. Levy. *Tunable Electron-Electron Interactions in LaAlO$_3$/SrTiO$_3$ Nanostructures.* Physical Review X **6**(4) (2016). `http://dx.doi.org/10.1103/physrevx.6.041042`.

[138] U. Schollwöck. *The density-matrix renormalization group.* Reviews of Modern Physics **77**(1), 259 (2005). `http://dx.doi.org/10.1103/revmodphys.77.259`.

[139] U. Schollwöck. *The density-matrix renormalization group in the age of matrix product states.* Annals of Physics **326**(1), 96 (2011). `http://dx.doi.org/10.1016/j.aop.2010.09.012`.

[140] I. P. McCulloch. *From density-matrix renormalization group to matrix product states.* Journal of Statistical Mechanics: Theory and Experiment **2007**(10), P10014 (2007). `http://dx.doi.org/10.1088/1742-5468/2007/10/p10014`.

[141] I. P. McCulloch. *Infinite size density matrix renormalization group, revisited* (2008). `http://arxiv.org/abs/0804.2509v1`.

[142] G. M. Crosswhite, A. C. Doherty, and G. Vidal. *Applying matrix product operators to model systems with long-range interactions.* Physical Review B **78**(3) (2008). `http://dx.doi.org/10.1103/physrevb.78.035116`.

[143] J. A. Kjäll, M. P. Zaletel, R. S. K. Mong, J. H. Bardarson, and F. Pollmann. *Phase diagram of the anisotropic spin-2 XXZ model: Infinite-system density matrix renormalization group study.* Physical Review B **87**(23) (2013). `http://dx.doi.org/10.1103/physrevb.87.235106`.

[144] P. W. Anderson. *Model for the Electronic Structure of Amorphous Semiconductors.* Physical Review Letters **34**(15), 953 (1975). `http://dx.doi.org/10.1103/physrevlett.34.953`.

[145] R. de Picciotto, M. Reznikov, M. Heiblum, V. Umansky, G. Bunin, and D. Mahalu. *Direct observation of a fractional charge.* Nature **389**(6647), 162 (1997). `http://dx.doi.org/10.1038/38241`.

[146] L. P. Kouwenhoven, D. G. Austing, and S. Tarucha. *Few-electron quantum dots.* Reports on Progress in Physics **64**(6), 701 (2001). `http://dx.doi.org/10.1088/0034-4885/64/6/201`.

[147] C. S. OHern, T. C. Lubensky, and J. Toner. *Sliding Phases in XY models, Crystals, and Cationic Lipid-DNA Complexes.* Physical Review Letters **83**(14), 2745 (1999). `http://dx.doi.org/10.1103/physrevlett.83.2745`.

[148] D. Pekker, G. Refael, and E. Demler. *Finding the Elusive Sliding Phase in the Superfluid-Normal Phase Transition Smeared byc-Axis Disorder.* Physical Review Letters **105**(8) (2010). `http://dx.doi.org/10.1103/physrevlett.105.085302`.

[149] P. Mohan, P. M. Goldbart, R. Narayanan, J. Toner, and T. Vojta. *Anomalously Elastic Intermediate Phase in Randomly Layered Superfluids, Superconductors, and Planar Magnets.* Physical Review Letters **105**(8) (2010). `http://dx.doi.org/10.1103/physrevlett.105.085301`.

[150] F. Bloch. *Über die Quantenmechanik der Elektronen in Kristallgittern.* Zeitschrift für Physik **52**(7-8), 555 (1929). `http://dx.doi.org/10.1007/bf01339455`.

[151] S. N. Kempkes, M. R. Slot, J. J. van den Broeke, P. Capiod, W. A. Benalcazar, D. Vanmaekelbergh, D. Bercioux, I. Swart, and C. M. Smith. *Robust zero-energy modes in an*

electronic higher-order topological insulator. Nature Materials (2019). `http://dx.doi.org/10.1038/s41563-019-0483-4`.

[152] R. D. L. Kronig and W. G. Penney. *Quantum Mechanics of Electrons in Crystal Lattices.* Proceedings of the Royal Society A: Mathematical, Physical and Engineering Sciences **130**(814), 499 (1931). `http://dx.doi.org/10.1098/rspa.1931.0019`.

[153] D. C. Tsui, H. L. Stormer, and A. C. Gossard. *Two-Dimensional Magnetotransport in the Extreme Quantum Limit.* Physical Review Letters **48**(22), 1559 (1982). `http://dx.doi.org/10.1103/physrevlett.48.1559`.

[154] K. J. Thomas, J. T. Nicholls, M. Y. Simmons, M. Pepper, D. R. Mace, and D. A. Ritchie. *Possible Spin Polarization in a One-Dimensional Electron Gas.* Physical Review Letters **77**(1), 135 (1996). `http://dx.doi.org/10.1103/physrevlett.77.135`.

[155] F. Bauer, J. Heyder, E. Schubert, D. Borowsky, D. Taubert, B. Bruognolo, D. Schuh, W. Wegscheider, J. von Delft, and S. Ludwig. *Microscopic origin of the '0.7-anomaly' in quantum point contacts.* Nature **501**(7465), 73 (2013). `http://dx.doi.org/10.1038/nature12421`.

[156] Y. Oreg, E. Sela, and A. Stern. *Fractional helical liquids in quantum wires.* Physical Review B **89**(11) (2014). `http://dx.doi.org/10.1103/physrevb.89.115402`.

[157] G. Shavit and Y. Oreg. *Fractional Conductance in Strongly Interacting 1D Systems.* Physical Review Letters **123**(3) (2019). `http://dx.doi.org/10.1103/physrevlett.123.036803`.

[158] Y. Gul, S. N. Holmes, M. Myronov, S. Kumar, and M. Pepper. *Self-organised fractional quantisation in a hole quantum wire.* Journal of Physics: Condensed Matter **30**(9), 09LT01 (2018). `http://dx.doi.org/10.1088/1361-648x/aaabab`.

[159] S. Kumar, M. Pepper, S. Holmes, H. Montagu, Y. Gul, D. Ritchie, and I. Farrer. *Zero-Magnetic Field Fractional Quantum States.* Physical Review Letters **122**(8) (2019). `http://dx.doi.org/10.1103/physrevlett.122.086803`.

[160] M. Briggeman, J. Li, M. Huang, H. Lee, J. Lee, C.-B. Eom, P. Irvin, and J. Levy. *Engineered spin-orbit interactions in LaAlO$_3$/SrTiO$_3$-based 1D serpentine electron waveguides.* In preperation (2020).

[161] J. Salfi, J. A. Mol, R. Rahman, G. Klimeck, M. Y. Simmons, L. C. L. Hollenberg, and S. Rogge. *Quantum simulation of the Hubbard model with dopant atoms in silicon.* Nature Communications **7**(1) (2016). `http://dx.doi.org/10.1038/ncomms11342`.

[162] K. K. Gomes, W. Mar, W. Ko, F. Guinea, and H. C. Manoharan. *Designer Dirac fermions and topological phases in molecular graphene.* Nature **483**(7389), 306 (2012). `http://dx.doi.org/10.1038/nature10941`.

[163] J. R. Abo-Shaeer, C. Raman, J. M. Vogels, and W. Ketterle. *Observation of Vortex Lattices in Bose-Einstein Condensates.* Science **292**(5516), 476 (2001). `http://dx.doi.org/10.1126/science.1060182`.

[164] P. Engels, I. Coddington, P. C. Haljan, V. Schweikhard, and E. A. Cornell. *Observation of Long-Lived Vortex Aggregates in Rapidly Rotating Bose-Einstein Condensates.* Physical Review Letters **90**(17) (2003). `http://dx.doi.org/10.1103/physrevlett.90.170405`.

[165] Y.-J. Lin, R. L. Compton, K. Jiménez-García, J. V. Porto, and I. B. Spielman. *Synthetic magnetic fields for ultracold neutral atoms.* Nature **462**(7273), 628 (2009). `http://dx.doi.org/10.1038/nature08609`.

[166] Y.-J. Lin, K. Jiménez-García, and I. B. Spielman. *Spin–orbit-coupled Bose–Einstein condensates.* Nature **471**(7336), 83 (2011). `http://dx.doi.org/10.1038/nature09887`.

[167] R. M. Lutchyn, J. D. Sau, and S. D. Sarma. *Majorana Fermions and a Topological Phase Transition in Semiconductor-Superconductor Heterostructures.* Physical Review Letters **105**(7) (2010). `http://dx.doi.org/10.1103/physrevlett.105.077001`.

[168] Y. Oreg, G. Refael, and F. von Oppen. *Helical Liquids and Majorana Bound States in Quantum Wires.* Physical Review Letters **105**(17) (2010). `http://dx.doi.org/10.1103/physrevlett.105.177002`.

[169] A. C. Y. Li and J. Koch. *Mapping repulsive to attractive interaction in driven–dissipative quantum systems.* New Journal of Physics **19**(11), 115010 (2017). `http://dx.doi.org/10.1088/1367-2630/aa8d5b`.

[170] J. Klinovaja, P. Stano, and D. Loss. *Topological Floquet Phases in Driven Coupled Rashba Nanowires.* Physical Review Letters **116**(17) (2016). `http://dx.doi.org/10.1103/physrevlett.116.176401`.

[171] V. Mourik, K. Zuo, S. M. Frolov, S. R. Plissard, E. P. A. M. Bakkers, and L. P. Kouwenhoven. *Signatures of Majorana Fermions in Hybrid Superconductor-Semiconductor Nanowire Devices.* Science **336**(6084), 1003 (2012). `http://dx.doi.org/10.1126/science.1222360`.

[172] K. Ray, S. P. Ananthavel, D. H. Waldeck, and R. Naaman. *Asymmetric Scattering of Polarized Electrons by Organized Organic Films of Chiral Molecules.* Science **283**(5403), 814 (1999). `http://dx.doi.org/10.1126/science.283.5403.814`.

[173] R. Gutierrez, E. Díaz, R. Naaman, and G. Cuniberti. *Spin-selective transport through helical molecular systems.* Physical Review B **85**(8) (2012). `http://dx.doi.org/10.1103/physrevb.85.081404`.

[174] K. M. O'Hara, S. L. Hemmer, M. E. Gehm, S. R. Granade, and J. E. Thomas. *Observation of a Strongly Interacting Degenerate Fermi Gas of Atoms.* Science **298**(5601), 2179 (2002). `http://dx.doi.org/10.1126/science.1079107`.

[175] T. Bourdel, L. Khaykovich, J. Cubizolles, J. Zhang, F. Chevy, M. Teichmann, L. Tarruell, S. J. J. M. F. Kokkelmans, and C. Salomon. *Experimental Study of the BEC-BCS Crossover Region in Lithium 6.* Physical Review Letters **93**(5) (2004). `http://dx.doi.org/10.1103/physrevlett.93.050401`.

[176] S. Krinner, D. Stadler, D. Husmann, J.-P. Brantut, and T. Esslinger. *Observation of quantized conductance in neutral matter.* Nature **517**(7532), 64 (2014). `http://dx.doi.org/10.1038/nature14049`.

[177] L. P. Kouwenhoven, F. W. J. Hekking, B. J. van Wees, C. J. P. M. Harmans, C. E. Timmering, and C. T. Foxon. *Transport through a finite one-dimensional crystal.* Physical Review Letters **65**(3), 361 (1990). `http://dx.doi.org/10.1103/physrevlett.65.361`.

[178] Y. Takagaki, Y. Tokura, and S. Tarucha. *Transmission of interacting electrons through a one-dimensional periodic potential.* Physical Review B **53**(23), 15462 (1996). `http://dx.doi.org/10.1103/physrevb.53.15462`.

[179] A. Nethwewala, H. Lee, M. Briggeman, Y. Tang, J. Li, J.-W. Lee, C.-B. Eom, P. Irvin, and J. Levy. *Inhomogeneous energy landscape in LaAlO$_3$/SrTiO$_3$ nanostructures.* Nanoscale Horizons (2019). `http://dx.doi.org/10.1039/c9nh00188c`.

[180] G. Binnig, C. F. Quate, and C. Gerber. *Atomic Force Microscope.* Physical Review Letters **56**(9), 930 (1986). `http://dx.doi.org/10.1103/physrevlett.56.930`.

[181] Asylum Research. *MFP-3D Atomic Force Microscope Installation and Operation Manual* (2003-2004).

[182] Aspire CFM `https://store.nanoscience.com/aspire-cfm.html`.

[183] F. Pobell. *Matter and Methods at Low Temperatures.* Springer Berlin Heidelberg (2007). `https://www.ebook.de/de/product/20512312/frank_pobell_matter_and_methods_at_low_temperatures.html`.